University of California
Merced

Solar Irradiance Forecasting at Multiple Time Horizons and Novel Methods To Evaluate Uncertainty

A dissertation submitted in partial satisfaction
of the requirements for the degree Doctor of Philosophy in
Mechanical Engineering and Applied Mechanics

by

Ricardo Marquez

2012

The dissertation of Ricardo Marquez is approved.

Carlos F. M. Coimbra, Advisor

Yihsu Chen

Gerardo Diaz, Committee Chair

University of California, Merced
2012

Solar Irradiance Forecasting at Multiple Time Horizons and Novel Methods To Evaluate Uncertainty.

RICARDO MARQUEZ.
(Under the direction of Carlos F. M. Coimbra.)

ABSTRACT

As an energy resource, solar energy provides a cleaner alternative to the conventional power generation systems and therefore solar energy has the potential to help achieve lower emissions standards as well to help provide domestic energy security. A major challenge, however, is the non-dispatchability and variability of the solar resource which makes it necessary to develop forecasting methodologies in order to safely integrate with the electric grid. As dictated by current electricity markets, power generation is dispatched according to day-ahead unit commitment as well as 1-hour ahead and 15-minutes for load-following services. In order to integrate large penetration levels of solar energy into the current systems, forecasting at these time intervals are necessary. In this work, we develop and evaluate several solar irradiance forecast models for multiple-time horizons. The 1-day ahead forecasting models are based on forecasted elements from the National Weather System's (NWS) forecasting database (NDFD). The 1-hour ahead forecasting models are based on sky cover indices derived from ground measurements including solar and infrared radiometers as well as a sky imager and we also develop satellite-based models that utilize neural networks for time-series predictions. For very short-term forecasts of $<$ 15-minutes ahead, we present a solar forecasting application using detailed image processing of a sky imager. Where possible, these models are compared to existing models in the literature. Because various authors use different benchmarks and forecast model quality measures, we also outline procedure that allows the comparisons of

different forecasting models and discuss why the procedure is a robust indicator of forecasting skill. In determining forecasting skill, it is necessary to quantify variability. Quantifying variability is also important for analyzing the economic impacts which are introduced by the addition of variability from a solar power system, which is discussed here in some detail. A case study of the economic impacts due to solar high-frequency variability is presented for the University of California Merced and a 1-MW photovoltaic plant.

Contents

List of Tables

List of Figures

Chapter 1

Introduction

In the context of the near-future scenario where a significant amount of variable energy resources is used to produce electricity, power producers, utility companies and independent system operators will rely heavily on streaming data and information to balance and manage the variability of energy supply and demand. Recent studies on higher penetration impact of renewables have emphasized the need for accurate forecasts if large variable capacities are to be achieved [4, 5, 6]. Historically, most of the power grid variability has been on the load (demand) side because fossil and nuclear generation are designed to operate in stable, dispatchable and controllable fashion. In order to increase renewable power capacity penetration, Independent System Operators (ISOs) must also be able to cope with generation variability and uncertainty.

The variablility of the solar energy resource at the ground level greatly complicates the management and integration of power output from solar farms. Today it is widely acknowledged by power producers, utility companies and independent system operators (ISOs) that there is a need for enhanced forecasting of weather systems and their effect on solar power output. For large scale solar applications, the amount of irradiance reaching the ground surface is most strongly affected by clouds, aerosols and water vapor column, with cloud effects being particularly dominant for most locations where solar is produced currently. Thus, there is particular need of developing fine-tuned cloud monitoring systems that would help manage inverter banks and dispatchers.

Current efforts in developing forecast models include the development of artificial neural networks (ANN) for time series predictions, semi-empirical models based on satellite images and predictions based on national or regional weather predictions (see, e.g., [7, 8]). Many of the existing forecast models have been shown to predict the 1-hour integrated solar irradiance 1 or 2 hours ahead to good accuracy [9, 10, 11] and forecast models for same-day [7, 8], 1–5 days ahead have also been developed with good accuracy and reliability. Effective forecasting methodologies and relevant inputs considered are highly dependant on the time horizons considered. This work builds on previous efforts by

- developing in Chapter 3 image processing techniques for sky imagers in order to produce solar irradiance forecasts for 3–15-minute ahead,
- developing in Chapter 4 a hybrid physics and stochastic modeling approach based on cloud indexing and velocimetry on satellite images and incorporating selected features into a ANN forecasting model for 30–120 minute forecast horizons,
- developing in Chapter 5 a 1-hr ahead forecasting methods using derived sky cover indices from ground-based measurements,
- and by developing in Chapter 6 an ANN forecasting model for same-day and 1-day ahead forecast horizons using the National Weather Service's (NWS) forecasting database.

Before developing the forecast models, we first present an forecast evaluation procedure in Chapter 2 which will help us to compare forecast skill with other forecast models in the literature.

1.1 A Metric for Forecast Quality

Comparing the relative advantages of different forecasting methodologies is not straightforward because different studies use different evaluation criteria, and also because the solar radiation data sets are dependent on geographic location and climate. The second issue is particularly significant

as it is relatively easier to forecast the solar irradiance during clear day periods, and therefore an oversimplistic forecast model can yield very good conventional statistical metrics for those conditions when solar irradiation is highly predictable. The same oversimplistic forecast model would certainly fail under different geoclimatic conditions. The purpose of the work presented in Chapter 2 is to introduce an alternative approach to evaluate the quality of forecast models by defining and comparing in a quantitative way the solar resource variability (V) and the forecast uncertainty (U). The observation that leads to the relationship between V and U is that forecast model errors are typically higher during wet (cloudy) days than during dry (clear) days, as clearly demonstrated in a few recent studies [7, 8]. In Chapter 2, we analyze forecast models to quantify the relationship between 'variability' and 'forecastability' in order to derive a consistent metric that is independent of the time horizon under consideration.

1.2 Sub-hourly forecasting using sky imaging

Total Sky Imagers (TSIs), originally developed for meteorological and aviation purposes, are potentially helpful for developing solar irradiance prediction and forecasting models, although the time horizon covered by such instruments is limited by the field of view and rapid turnover of cloud motion. Here we propose and test new methods for predicting future values of Direct Normal Irradiance (DNI) using processed images taken by a ground level TSI.

Different solar irradiance forecast methodologies have been proposed for various time horizons. For medium-term solar forecasting of 6-hours to a few days ahead, NWP models have been tested [3, 12, 7, 13, 14]. For time horizons of 1-6 hours, satellite-based forecasts are competitive with NWP models as shown in [3]. Satellite models have also been applied to 30-minute ahead forecasting [15]. Besides these physical image-based models, time-series based solar forecasting methods have also been extensively applied, (e.g. [16, 17, 18, 11, 9, 19, 20, 2]) and validated over wide ranges of time horizons. In some of these time-series applications, direct cloud information is not used [19, 11, 17, 18, 2] while some incorporate cloud information as exogenous inputs [9, 20]. The

time-series forecasting methodologies have been applied successfully for 5-15 minutes [21], 1-hour [9, 19, 11], and 24-hours ahead [18].

To date, the use of sky imagers for solar irradiance forecasting has been rather limited. One study [22], employed a TSI to extract cloud features using a Radial Basis Function Neural Network (RBFNN) pixel classifier to include in an Artificial Neural Network (ANN) forecast model for 1-minute to 60-minute ahead horizons. Results from this study were mixed, showing only marginal improvements with reference to a model which uses only irradiance lagged values as input variables. This initial study concluded that errors introduced by the cloud index estimates were limiting the accuracy of the TSI-based solar irradiance forecasts. The work of [20] uses cloud indices obtained from a TSI built-in cloud classification algorithms, and cloud indices derived from Infrared Radiometric (IR) measurements to report improved results for 1-hour forecasting of Global Horizontal Irradiance (GHI) using ANNs for time-series predictions. More recently, Chi and coworkers [23] used TSI images to produce nowcasting of GHI single-point solar irradiance sensors located at the University of California San Diego meteorological network. Their study also analyzed the cloud field propagation by computing matching errors of the future image given current images translated in the direction of the computed velocity field. Their results suggest that TSI maybe useful for forecasting horizons of up to 15 minutes, depending on cloud velocities and field of view. The work presented Chapter 3 discusses new developments using sky imagers to forecast the direct normal irradiance (DNI).

1.3 Satellite and ANN-based solar forecasting

The most important factor affecting the amount of solar irradiation at any given time of a day is cloud cover. Predicting accurately the extent, motion, formation, dissipation, and transmissivity of clouds is a very complex task for solar forecast applications, even for moderate temporal (few minutes ahead) and spatial scales (few kilometers). As a result, short-term forecasting of solar irradiance can be very difficult when using satellite-based modeling if the models are not robust to

the uncertainty in the many potential parameters involved. For this reason, we consider the use of ANNs in combination with detailed satellite image processing for determining future values of the global horizontal solar irradiance (GHI).

Although several short-term solar irradiance forecasting studies have been presented [20, 11, 9, 24, 18, 21] there are much fewer attempts which directly use satellite-imagery [15, 25, 1]. Many of the methodologies that are not satellite-based rely heavily on ANNs as the forecast models [20, 11, 9, 24, 18, 21], as well as auto-regressive models [24, 11, 21]. The satellite-based models, on the other hand, are based on cloud translation then use the clear-sky index to forecast solar irradiance [15, 25, 1], with the exception that in [25], ANNs were used but without incorporating into the model the results of the image-processing used for the cloud translations. The aim of this study is to combine the ANNs with the information gathered in the detail image processing stages.

The work presented in Chapter 4 involves the development of two forecasting models. The first GHI forecast model (GHI_{f1}) only includes satellite-derived information such as cloud fractions computed at prescribed grid elements of the satellite images. This model contrasts the recent study in [26] where only endogenous inputs are considered to examine the effectiveness of the statistical forecast approaches. The (GHI_{f1}), in contrast, uses only exogenous inputs (inputs not derived from GHI time-series). We slightly increase the complexity in the second GHI forecast model (GHI_{f2}) by including lagged values of GHI in addition to the satellite-derived inputs to examine the effectiveness of using satellite-derived information.

It has been expressed in [2, 27] the increased urgency, as the energy industry moves towards the integration of increased capacity levels of renewable energy systems, to develop approaches and best practices to properly evaluate and compare existing forecast models in order to make progress in development and utilization of solar forecasts. A second purpose of the work in Chapter 4 is to extensively compare with other satellite-based solar forecasting methods such as in [1, 8] by evaluating the RMSE forecasting skill and the forecasting skill metric recently proposed in [2].

1.4 Ground-based sky cover indices

Sky Cover (SC) is the most critical variable in forecasting solar energy power generation. Satellite images are common source of cloud cover information but they lack the detailed temporal and spatial resolution required to accurately monitor the operational effects on solar energy for a given site. A shortcoming of using satellite images for cloud information is the lack of detailed temporal and spatial resolution required to accurately monitor the operational effects on solar energy for a given site. An alternative approach is to use ground based sky images from Total Sky Imager (TSI) where data can be gathered at high frequency, but even then such information is only available during daytime. Thus, night cloud cover information that is relevant for forecasting solar power generation in the early morning hours is not registered. An additional problem of completely relying on TSI data is the high costs associated with imaging instruments, which limits their utilization for covering large regions [28, 29].

One of the objectives of this work is to resolve these shortfalls by developing a technique for obtaining cloud cover information using infrared radiometers (IR) as a complement to the development of cloud cover methods based on the visible part of the electromagnetic radiation spectra. Some previous works have examined how to extrapolate cloud information from solar radiation and other recent works have also included infrared radiation to predict cloud cover [29, 30]. Measurements that use IR are cheaper relative to sky imaging measurements, are characterized by high measurement and collection frequency, and are already located at many standard weather monitoring stations [28], and therefore wider coverage is possible. Another possible advantage of using IR radiometers is that they are sensitive to cloud cover during the night time [30], which is critical to forecast morning shoulder ramping rates.

The intended application of our results is to incorporate the IR measurements as inputs to solar radiation forecast models. To this extent, solar forecasting methodologies rely on cloud cover information with varying rates of success [8, 7, 9]. In [8, 7], for example, sky cover is obtained from forecasts provided by the National Weather Service (NWS) where the data sets can be used to

produce same-day and several days ahead hourly solar forecasts. Cao and Lin [9] used cloud cover data retrieved from a weather station forecasts given in specific category format: overcast, sunny, cloudy, and cloudy and sunny where the categories were later processed using defuzzification techniques. These previous approaches, however, have generally neglected the use of infrared radiation and thus ignored opportunities for improvements in forecasting performance. A forecasting model based on using an infrared radiometer and a Total Sky Imager (TSI) is developed in Chapter 5.

1.5 Same-day and 1-day ahead forecasting based on the NDFD

The NDFD produces same-day up and to 7-days ahead forecasts of meteorological variables, not including solar irradiance. We refer to these forecasting time horizons as medium-term to be consistent with [8], whom have recently developed and validated a forecasting model for GHI based on the sky cover data supplied from the NDFD. When applied to the Sacramento and New York areas, their forecasting model obtained accuracies consistent with preliminary analysis using Multiple Output Statistics and meso-scales models elsewhere (e.g. [31]). More recently, their model has been evaluated in a number of locations with widely different climates [8] and thus further validating the generalization of the simple model. The present study extends theirs by considering the use of additional meteorological variables in order to enhance the forecasting capabilities of the models. Because this study considers the use of a larger number of variables, we present and employ an objective strategy which helps to select relevant inputs. This work is presented in Chapter 6.

1.6 Cost of solar variabililty

While much variability reduction can be achieved through geographic diversity and smoothing [32, 33, 34, 35, 36], i.e., distributed PV systems, there are still concerns that at large penetration

levels of renewable energies, the variability may significantly impact electricity markets [35, 37] as well as cause other technical issues [6]. Currently, the grid operates with most of the uncertainty coming from the demand side. To handle the uncertainty due to the stochastic solar variability, transmission operators (ISOs) must make sure to allocate additional reserve capacity [37, 38]. With the exception of hydro, reserves with fast-ramping capabilities are typically comprised of the more expensive generating units and thus uncertainty has the effect of creating higher electricity prices [38].

In [32, 36], compelling evidence is presented on the possibility to significantly reduce fluctuations from distributed PV systems as opposed to a single reference location. While this is one way to manage the fluctuations produced from PV plants, it is questionable whether the advantages of geographic diversity of PV systems outweigh the benefits of economies of scales of large centralized plants. Furthermore, [39] argues that managing variability in renewable energy resources is technically feasible; but social, political – and hence, economical – obstacles hinder the integration of renewable energy sources. Therefore, it is important to quantify the cost of the fluctuations produced by renewable electricity generation, in addition to developing methods to manage the variability of the electricity produced by solar power systems. Chapter 7 deals with estimating the costs of variability in terms of suitable variability metrics.

Chapter 2

A Proposed Metric for Evaluation of Solar Forecasting Models

This work presents an alternative metric for evaluating the quality of solar forecasting models. Some conventional approaches use quantities such as the root-mean-square-error and/or correlation coefficients to evaluate model quality. The direct use of statistical quantities to assign forecasting quality can be misleading because these metrics do not convey a measure of the variability of the time-series for the solar irradiance data. In contrast, the quality metric proposed here, which is defined as the ratio of solar uncertainty to solar variability, compares forecasting error with solar variability directly. By making the forecasting error to variability comparisons for different time windows, we show that this ratio is essentially a statistical invariant for each forecasting model employed, i. e., the ratio is preserved for widely different time horizons, and therefore could potentially provide a robust way to compare solar forecast performance. We employ the proposed metric to evaluate two new forecasting models proposed here, and compare their performances with a persistent model.

2.1 Introduction

One of the leading impediments for achieving higher market penetration and power grid connectivity of solar and wind technologies is the variable nature of such resources. Recent studies on higher penetration impact of renewables have emphasized the need for accurate forecasts if large variable capacities are to be achieved [4, 5, 6]. Historically, most of the power grid variability has been on the load (demand) side because fossil and nuclear generation are designed to operate in stable, dispatchable and controllable fashion. In order to increase renewable power capacity penetration, Independent System Operators (ISOs) must now cope with generation variability. Therefore load forecasting errors have economic consequences on electricity markets, as well as other operational impacts [5].

Current efforts in developing forecast models include the development of artificial neural networks (ANN) for time series predictions, semi-empirical models based on satellite images and predictions based on national or regional weather predictions (see, e.g., [7, 8]). Many of the existing forecast models have been shown to predict the 1-hour integrated solar irradiance 1- or 2-hours ahead to good accuracy [9, 10, 11] and forecast models for same-day [7, 8], 1–5 days ahead have also been developed with good accuracy and reliability. Effective forecasting methodologies and relevant inputs considered can vary widely depending on the time horizons considered.

However, consideration of the relative advantages of different forecasting methodologies is not straightforward because different authors use different evaluation criteria, and also because the solar radiation data sets are dependent on geographic location, time of year, and climate. The second issue is particularly significant as it is relatively easier to forecast the solar irradiance during clear day periods, and therefore an oversimplistic forecast model can yield very good conventional statistical metrics for those conditions when solar irradiation is highly predictable. The same oversimplistic forecast model would certainly fail under different geoclimatic conditions. The purpose of this work is to present an alternative approach to evaluate the quality of forecast models by defining and quantitatively comparing the solar resource variability (V) and the forecast uncertainty (U).

The observation that leads to the relationship between V and U is that forecast model errors are typically higher during wet (cloudy) days than during dry (clear) days, as clearly demonstrated in a few recent studies [7, 8]. In this paper, we analyze forecast models and quantify the relationship between 'variability' and 'uncertainty' in order to produce a consistent metric that is independent of the time horizon under consideration.

Since the forecast quality measures that is introduced depends on using clear sky solar irradiation model as a normalization factor to compute V and U and to define a persistence model, we consider 2 clear sky models. We also test a definition of V and U and a persistence model based on the extraterrestrial solar irradiance so that, unlike the clear sky models, location dependent parameters can be avoided. The clear sky and persistence models are described in Sections 2.2 and 2.3, respectively. In Section 2.4, the solar irradiance variability is defined and discussed following the work from [35, 32]. After these preliminaries, the goal here is to evaluate the forecasting using a more robust and meaningful metrics which is based on determining the average forecasting skill ($\langle s \rangle$). In Section 2.5, we describe the forecasting model evaluation procedure. In Section 2.6, two forecasting models are developed and, along with the persistence models, are evaluated in terms of the conventional and proposed evaluation metrics. The rest of the paper discusses further forecasting evaluations for various time-horizons and other possible applications of understanding forecast uncertainty and variability.

2.2 Clear-Sky Models

This section describes two clear sky models which are used for persistence forecasts and for normalization in the evaluation metric described later. The parameters of the clear sky models are site specific to the location of the study (Merced, CA.) and for the period of the study (Jan. 1 – Oct. 31, 2010) and therefore may not be accurate for other locations. The interested reader can find other well studied clear sky models from [40]. Here we only choose two clear sky models, one which is a based on a polynomial regression and the other based on the European Solar Radiation

Atlas (ESRA) clear sky model, so that the sensitivity of the methods for forecasting of clear sky days can be examined. The sensitivity should be small since short-term forecasting involves the use of previous irradiance values that can be used to adjust the clear sky predictions. This particular feature of short-term forecasting is shown using a persistence model in Section 2.3.

2.2.1 CS Model 1: Polynomial Fit

The first clear sky model that we are considering is a third degree polynomial function of cosine of the solar zenith angle $\cos(\theta)$,

$$I_{clr,poly} = c_3 \left(\cos\theta\right)^3 + c_2 \left(\cos\theta\right)^2 + c_1 \left(\cos\theta\right) + c_0 \tag{2.1}$$

where the coefficients where determined as: $c_3 = 688$, $c_2 = 1103$, $c_1 = 518$, $c_0 = -3$ and $I_{clr,poly}$ is in W/m^2. This model was generated using selected clear sky days in the data set collected in the year 2010 at the University of California Merced solar observatory station. The accuracy for a few selected days is shown in Table 2.1.

2.2.2 CS Model 2: ESRA

As a second clear sky model, $I_{\text{clr,ESRA}}$ is computed using the ESRA model adopted from [41, 42]. The algorithms used are developed by [41] and were obtained from the accompanying c.d. to [42]. The ESRA model only depends on a site dependent Linke-Turbidity factor (T_L). Here, T_L is set to $T_L = 4$ so that the bias for all of the clear sky days of the entire data set is minimized.

The polynomial and ESRA clear sky models are compared in Fig. 2.1 which shows that models do not exactly match. Although their correlation is high, there is a spread of $RMSE = 14.7W/m^2$. It is intentional to have a difference between the polynomial and the ESRA clear sky models so that we can test the resulting sensitivity to the evaluations of the developed forecasting models.

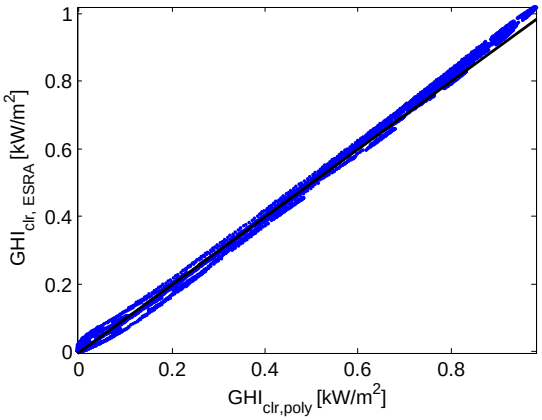

Figure 2.1 – Comparison of ESRA and polynomial-fit clear-sky models. The coefficient of determination between the two models is $(R^2) = 0.998$ and the root-mean-squared error is $RMSE = 14.7W/m^2$.

2.3 Persistence Models

2.3.1 Clear Sky Persistence Models

The clear sky persistence models are defined as having the clear sky conditions (ratio between the measured irradiance to the clear sky irradiance) persist for the next time-step,

$$\hat{k}(t + \Delta t) = k^*(t) = \frac{I(t)}{I(t)_{clr}}. \tag{2.2}$$

From $\hat{k}(t + \Delta t)$, the prediction for the next value of solar irradiance value $I(t + \Delta t)$ is computed as,

$$\hat{I}_p(t + \Delta t) = \hat{k}(t + \Delta t)\ I_{clr}(t + \Delta t). \tag{2.3}$$

This simple persistence model only relies on I_{clr} which is time and location dependent. Since the persistence model only relies on I_{clr}, there can also be several persistence models depending on how I_{clr} is estimated. Here we consider two persistence models based on the clear sky models already presented,

$$\hat{I}_{poly}(t + \Delta t) = k_{poly}(t)\ I_{clr,poly}(t), \tag{2.4}$$

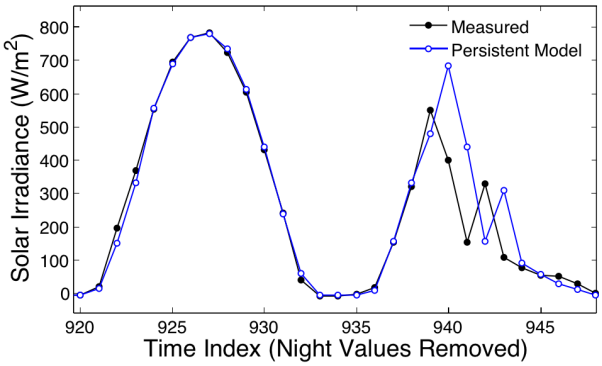

Figure 2.2 – Example of persistent model performance for a clear and a partially cloudy day (Mar. 20 – 21, 2010). The clear day is approximated very well by persistent model, whereas a 'time delay' is observed for the partially cloudy day.

and

$$\hat{I}_{ESRA}(t + \Delta t) = k_{ESRA}(t)\ I_{clr,ESRA}(t + \Delta t). \tag{2.5}$$

An illustration of the persistence model, $\hat{I}_{poly}(t + \Delta t)$, is shown in Fig. 2.2 which shows two prominent characteristics of persistence model in general. The first characteristic, is that large forecasting errors mainly occur during abrupt changes in $I(t)$ which are a result of passing opaque clouds. The second characteristic is the obvious lag of the abrupt change as can be clearly seen in the second day in Fig. 2.2. During cloudless periods, the persistence model is extremely effective as a forecast model as there is very little error resulting from the persistence of the clear sky values.

2.3.2 Clearness Persistence Model

As a slight variation of the persistence models just described, we also apply a *clearness* persistence model which is based on the extraterrestrial solar radiation (I_0) rather than I_{clr}, that is computed in W/m^2 as,

$$I_0 = G_0\ \cos(\theta_z) \tag{2.6}$$

where $G_0 = 1367 W/m^2$ is the solar constant. Moreover, this persistence does not involve any location-dependent fitting parameters as the clear sky models, however, when compared to irradi-

ance the I_0 has a large positive bias I_0. The resulting clearness-based persistence model is similarly defined as,

$$\hat{I}_0(t + \Delta t) = k_0(t)\ I_0(t + \Delta t). \tag{2.7}$$

Applying this persistence model gives us an extreme case where the normalization factor has a large positive bias compared to measured clear sky irradiance values and will be useful to evaluate the sensitivity of how accurate clear sky models need to be for short-term forecasting.

2.3.3 Clear Sky Modeling and Forecasting Accuracy

This section is intended to clarify the difference between the accuracy of clear sky models (I_{clr}) and persistence forecast models ($\hat{I}_p$) during clear days. The main difference is that the persistence models utilize the clear sky (or clearness) index at time t as an indication of the irradiance value at $t + \Delta t$, whereas the clear sky model does not use this information. Clear sky models are generally used with satellite-based modeling to predict irradiance for location where no other measurements exist, however, in forecasting applications, on-site solar irradiance measurements are generally available. As a result, the persistence models are more accurate than the clear sky models.

To demonstrate, consider the arbitrarily selected clear days shown in Fig. 2.3 which shows the measured hourly average values of the solar irradiance $I(t)$, the polynomial based clear sky model $I_{clr,poly}$, and the polynomial based persistence forecast model $\hat{I}_{poly}$. As this graph shows, the clear sky model fails to overlap well the irradiance values for a few of the days while on other days there is close overlap. The persistence, on the other hand, is fairly accurate for each of the days shown. The same analysis can be done with other clear sky (or extraterrestrial) and persistence models. Applying the root-mean-squared error (RMSE) (defined in Section 2.5) and mean-bias-error (MBE) as levels of accuracy for the days shown in Fig. 2.3, we get the results shown in Table 2.1. According to the obtained values, the persistence-based forecasts are much more accurate than the accuracy of a clear sky model indicate. Similar results can be obtained for other forecasting horizons besides 1-hour. Based on our experience, clear sky modeling accuracy is not critical for short-term forecasting

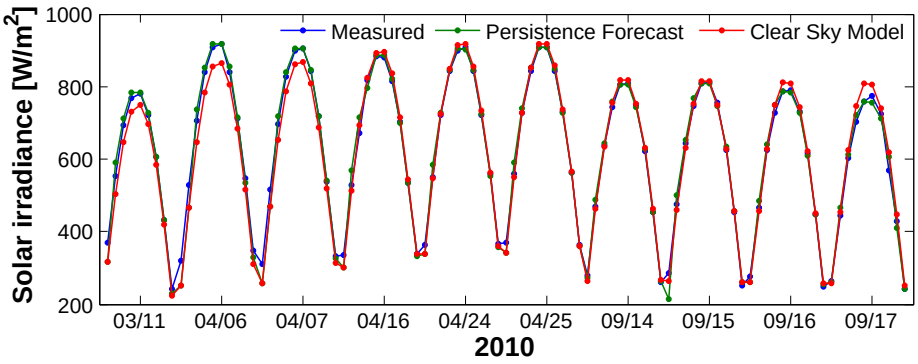

Figure 2.3 – Measured, modeled, and forecasted clear sky days arbitrarily selected for 2010. This figure illustrates the improved accuracy of a clear sky persistence forecast model over original clear sky model. The RMSEs are respectively 20.7 W/m^2 and 26.6 W/m^2 for the clear sky persistence forecast model and the original model.

Table 2.1 – Comparing Clear Sky and Extraterrestrial models with clear sky and clearness persistence models.

	RMSE $[W/m^2]$		MBE $[W/m^2]$	
	I_{clr}	$\hat{I}_p$	I_{clr}	$\hat{I}_p$
Polynomial	28.1	12.9	-12.8	-0.0906
ESRA	26.6	20.7	7.44	-0.186
Extraterrestrial	257	31.5	-252	7.28

applications.

2.4 Solar Resource Variability

The variability of solar irradiance at the ground level is due to several factors such as the presence of participating gases in the atmosphere (CO_2, H_2O, etc.), aerosols, cloud cover and solar position [42]. Most of the solar variability, however, is due to the latter two factors. The variability due to solar position is completely deterministic while the variability due to clouds is considered mostly stochastic because precise models for cloud dynamics have been proven elusive. The portion of solar variability that is of most concern to forecast models is the cloud-induced (or stochastic) component [6, 35, 43], thus we refer to solar variability as the standard deviation of the step-changes of the ratio of the measured solar irradiance to that of a clear sky solar irradiance so that the diurnal

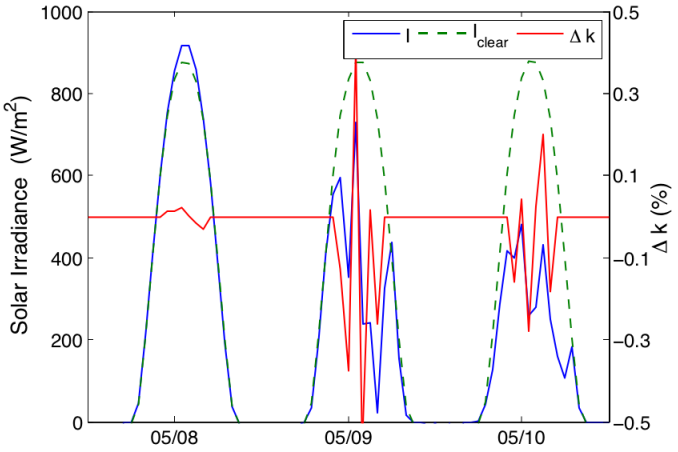

Figure 2.4 – Time series of Global Horizontal Irradiance (I) values, estimated clear-sky I and calculated values of stochastic step changes, Δk (Data for May 8–10, 2010 in Merced, CA).

variability is neglected,

$$V = \sqrt{\frac{1}{N}\sum_{t=1}^{N}\left(\frac{I(t)}{I_{clr}(t)} - \frac{I(t-1)}{I_{clr}(t-1)}\right)^2} = \sqrt{\frac{1}{N}\sum_{t=1}^{N}(\Delta k(t))^2}. \tag{2.8}$$

In the above definition for V, k is either the clear sky or clearness index depending on whether we use the $I_{clr,poly}$, $I_{clr,ESRA}$ or I_0. This formulation of variability is essentially the same as in [32, 44], except for the modification to include the deterministic changes ($\Delta k(t)$) as is done in [35, 43]. For very small time intervals of less than 5 minutes this modification is not too important because the deterministic (solar position dependent) variations are small. Figure 2.4 shows values of $\Delta k(t)$ for a sequence of clear and cloudy days. For clear days, the fluctuations $\Delta k(t)$ are much smaller than for the cloudy days where large ramps are apparent in the $\Delta k(t)$ time-series signal.

2.5 Uncertainty In Solar Resource: Forecasting Errors

2.5.1 Conventional Statistical Metrics to Characterize Model Quality

The coefficient of determination is a comparison of the variance of the errors to the variance of the data which is to be modeled,

$$R^2 = 1 - \frac{\mathrm{Var}(\hat{I} - I)}{\mathrm{Var}(I)}, \tag{2.9}$$

where the denominator in the second term of the right hand side of the equation is the calculated variance $\mathrm{Var}(I)$ of the data set, not to be mistaken for the variability ($\approx \sqrt{\mathrm{Var}(\Delta k)}$).

Another common evaluation metric is the root-mean-squared error (RMSE) which yields a measure of the average spread of the forecasting errors. The RMSE is calculated as,

$$\mathrm{RMSE} = \sqrt{\frac{1}{N}\sum_{t=1}^{N}\left(\hat{I}(t) - I(t)\right)^2}, \tag{2.10}$$

where the summation is carried over the entire data set. Typically night values are removed in the above calculations of R^2 and RMSE and only 1 value is given to summarize the entire data set. Both the RMSE and the R^2 do not help to quantify the amount of variability actually in the irradiance data. Other solar forecasting metrics include normalization of RMSE (relative RMSE), the Mean Bias Error (MBE), the Mean Absolute Error (MAE), the Mean Absolute Percentage Error (MAPE), and the correlation coefficient (ρ). Again, none of these metrics embed a sense of variability of the irradiance time-series data.

2.5.2 Proposed Metric

Here we define the uncertainty as the standard deviation of a model forecast error divided by the estimated clear sky value of the solar irradiance over a subset time window of N_w data points:

$$U = \sqrt{\frac{1}{N_w}\sum_{t=1}^{N_w}\left(\frac{\hat{I}(t) - I(t)}{I_{clr}(t)}\right)^2}. \tag{2.11}$$

This definition is related to the commonly used RMSE [8, 10, 7, 11] where sometimes relative or normalized RMSE is used [7, 8, 11] with respect to the average irradiance. The present definition of solar resource uncertainty is closely related to those except that in our definition, the normalization is made with respect to I_{clr} for which we will use $I_{clr,poly}$, $I_{clr,ESRA}$ or I_0 in our evaluations.

The following metric directly evaluates the variability that is effectively reduced by the forecasting models by taking the difference between U and V and normalizing it with respect to V,

$$s = \frac{V - U}{V}, \tag{2.12}$$

where U and V are calculated over the same data set. The metric for evaluating the quality of forecast models is more simply computed by considering the ratio between uncertainty, U, and variability, V, such that:

$$s = 1 - \frac{U}{V}. \tag{2.13}$$

The forecast quality measure is defined above is such that when $s = 1$ it means that the solar irradiance is perfectly forecasted, and when $s = 0$ the solar irradiance variability dominates the forecast. By definition, the persistence model should have a forecast quality measure of $s = 0$, as can be shown by comparing Eqns. (2.3), (2.8) and (2.11). The ratio U/V would be then defined as a measure of the benefit of a forecast method with respect to the persistency forecast based on the clear sky index. If s is negative for a developed forecast model, then that model performs worse

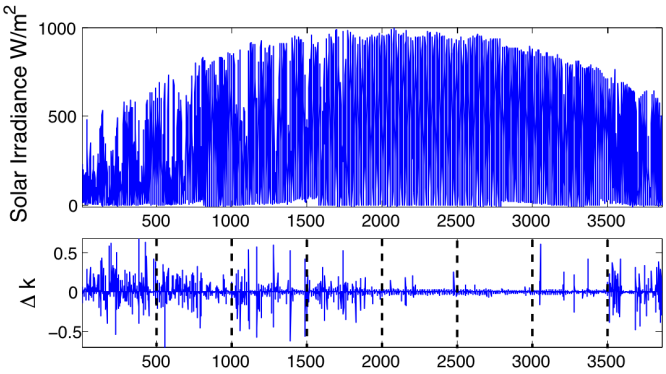

Figure 2.5 – Time series of solar irradiance and Δk. The figure illustrates the partition of the time series into window sizes of $N_w = 500$ (hours). Each dashed vertical line represents the boundaries of the 500-hour time windows.

than a persistence forecast. A typical forecast model should be characterized with values between 0 and 1, with higher values indicating better forecasting.

Since U and V are random variables, it follows that s is also a random variable. To obtain a representative value of s, we take the average value $\langle s \rangle$ as the indication of forecast skill. The average is obtained by calculating U and V for various time-window subsets. If a time window contains a large number of clear days, then both U (forecasting error) and V (the solar irradiance variability) will be small for that time window, thereby, the relative amount of error to variability is preserved. The time windows are selected by fixing N_w (the window size) and computing U_j and V_j over each jth window in the time series. The window partitioning is illustrated in Fig. 2.5, showing solar irradiance and calculated values of Δk_{poly} for the data set spanning Jan. 1 – Oct. 31. Low confidence experimental values due electrical power issues that occurred in May and July were removed from the calculations. In the case shown in Fig. 2.5, the window size is $N_w = 500$ and are separated by the dashed vertical bars. As mentioned above, night values are not included in Fig. 2.5, nor are they used in the calculations below.

2.6 Application Of Proposed Metric To Forecast Model Evaluation

The metric proposed is now applied to solar forecasting models based on Artificial Neural Networks (ANNs). We employ feedforward ANNs to approximate future hourly values of the $I(t)$ using lagged values of the time series. In the first case, we use only the time-series of hourly averaged $I(t)$, and in the second case, we use more information of $I(t)$ by including 30-minute and 6-minute moving averages and standard deviations computed from 30-second interval data. In this work, we do not consider applying an input selection scheme to determine the most relevant inputs (see e.g., [7]), but rather limit the scope to determining whether or not including several more inputs than just the hourly averaged values of $I(t)$ time series alone will improve the forecasting performance of the models. The forecasting performances are evaluated based on the conventional and the proposed metric (s) in order to compare and contrast the quality of the models.

2.6.1 NAR And NARX Forecasting Models

The forecast model including only the hourly averaged $I(t)$ time-series as an input is referred to as the Nonlinear AutoRegressive (NAR) forecasting model, and the model including additional inputs is referred to as the Nonlinear AutoRegressive with eXogenous inputs (NARX) forecasting model. The NAR model for 1-hour ahead predictions can be mathematically expressed as

$$\hat{I}(t+1) = f\left(I(t), I(t-1), \ldots, I(t-n)\right), \tag{2.14}$$

where $n+1$ is the number of time delays of the time series $I(t)$ which are included as inputs to predict $I(t+1)$. The number of time delays is set to 2 (e.g., $I(t)$, $I(t-1)$ are used to predict $I(t+1)$). The function (f) is based on a feed-forward ANN structure where the number of hidden neurons is set to 10. The values of the network weights are determined by the 'early-stopping' method

for ANN training where the data is split into three sets – a training set for computing directional derivatives of the errors in weight space, a testing set for determining when to stop training, and a validation set which is not used at all during the ANN training [45, 42]. Data from Oct. 15 – 31, 2010 is used for validation and the rest of the data from Jan. 1, 2010 – Oct. 14, 2010 is split randomly into 80% for the training set and 20% for the testing sets. The ANNs are implemented using the Matlab Neural Network Toolbox Version 7.0.

The NARX model is similar to the NAR model except that more time-series signals are utilized in the forecast scheme,

$$\begin{aligned} \hat{I}(t+1) &= f\left(I(t), I(t-1), \ldots, I(t-n),\right. \\ &\quad \left. u_1(t), u_1(t-1), ..., u_2(t), ..., u_m(t-n)\right), \end{aligned} \tag{2.15}$$

where m is the number of exogenous inputs. In this case, the u's are 30-minute and 6-minute backwards moving averages (MA) and standard deviations (SD) of clearness index values which are calculated from 30-second interval data, denoted as k' to distinguish from k which is the clear sky index for hourly averages of I. For example, the 30-minute MA and SD is calculated as,

$$u_{\mathrm{MA}_{30\mathrm{min}}}(t) = \frac{1}{N} \sum_{\tau\,=\,t-30\mathrm{min}}^{t} k'(\tau), \tag{2.16}$$

and

$$u_{\mathrm{SD}_{30\mathrm{min}}}(t) = \sqrt{\frac{1}{N} \sum_{\tau\,=\,t-30\mathrm{min}}^{t} (k'(\tau) - \bar{k'}(t))^2}, \tag{2.17}$$

where $\bar{k'}(t) = u_{\mathrm{MA30min}}(t)$. The 6-minute MA and SD is similarly defined. These inputs are an attempt to use the trends at the last moments of the current hour to forecast the next 1-hour time step. Again, f in Eqn. (2.15) is also a feedforward ANN which contains more input neurons than the NAR model and the number of time delays are set to 2 for each signal. The number of hidden neurons are set to 10, and the early-stopping method is used for adjusting the weights.

2.6.2 Comparison Between Persistent and Forecasting Models

The forecast quality evaluations were performed for the data set collected from Jan. 1 – Oct. 31 of 2010. Figure 2.6, shows scatter plots of U_j versus V_j computed for each jth time-window partitioning of the data set for $N_w = 50, 100, 150$, and 200. These plots allow us to visualize the forecasting performance over various time window subsets with different variability values. The difference between each of the evaluations is the normalization factor in the calculations of U and V, where we used on separate occasions $I_{clr,poly}$, $I_{clr,ESRA}$, and I_0. These plots show that the persistence models (also distinctive in terms of the normalization variable) all result in $s = 0$, since $U_j = V_j$ for any window j. Note that, for the extraterrestrial case, U_j and V_j have a smaller numerical range than the cases for using $I_{clr,poly}$ and $I_{clr,ESRA}$. This is because $I_0 > I_{clr,poly}$ and $I_{clr,ESRA}$. In all cases, the general trends and conclusions are the same which can be visualized by the scatter points in Fig. 2.6. The NAR model forecast quality seems to be not much better than persistence, while the NARX model does show some significant forecasting benefit since many of the scatter points fall below the 1:1 line.

The results are quantitatively evaluated by computing an approximation of $\langle s \rangle$. As mentioned earlier, s is a random variable which depends on the ratio U/V. The statistical average of this ratio is approximated by computing the slope of the scatter points as shown in Fig. 2.5, since the scatter plots from each of the models form almost a linear relationship[1]. The slopes calculations are repeated using $N_w = 10, 11, \ldots, 200$ and the results are plotted in Fig. 2.7, where we can see that, values of $\langle s \rangle$ converge to a certain value as N_w increases. For the persistence models $\langle s \rangle = 0$, for the NAR model $2\% < \langle s \rangle < 5\%$, and for the NARX model $10\% < \langle s \rangle < 15\%$. Again, there is very little difference in the resulting approximation of $\langle s \rangle$ amongst which normalization factor is used in the evaluation procedures.

Numerical values of $\langle s \rangle$ obtained using $N_w = 200$ are given in Table 2.2, along with the more

[1]Throughout this paper, we exclusively use a linear relationship between U and V for simplicity. In the future, we will consider advanced methods to account for nonlinear and piecewise relations between U and V.

Table 2.2 – Forecasting quality metrics for the persistent, NAR, and NARX models on validation and training data sets. For comparisons, the metric $s = 1 - U/V$ is based on three normalization factors.

Training Set Model	R^2	RMSE (W/m^2)	s_{poly}	s_{ESRA}	s_0
$I_{p,0}$	0.964	59.4	0	–	–
$I_{p,ESRA}$	0.969	55.5	–	0	–
$I_{p,poly}$	0.973	52.4	–	–	0
NAR	0.972	53.2	1.74 %	2.27 %	3.71%
NARX	0.977	48.8	11.56 %	12.02 %	13.1%
Validation Set Model	R^2	RMSE (W/m^2)	s_{poly}	s_{ESRA}	s_0
$I_{p,0}$	0.918	62.4	0	–	–
$I_{p,ESRA}$	0.926	59.5	–	0	–
$I_{p,poly}$	0.934	56.5	–	–	0
NAR	0.924	60.2	-2.56 %	-2.53 %	2.66 %
NARX	0.949	49.4	16.12 %	16.25 %	20.1 %

common forecast quality metrics, the R^2 and the RMSE. Considering first R^2, which range 0.964–0.977 on the validation data set, this forecasting quality measure gives the impression that the forecasts are very accurate even for the persistence models. This performance measure, however, is misleading because, by definition, the persistence model does not capture any of the solar irradiance variability. Similarly, the RMSEs, which range from 48.8–59.4 W/m^2, give misleading conclusions if compared to other RMSEs in the literature (e. g., [7, 20, 8, 10, 11, 9]) without first knowing about the solar irradiance variability conditions in those studies. By using the R^2 or $RMSE$s, it is not clear either how much those difference actually translate to differences in forecast quality. In terms of the $\langle s \rangle$ metric, it is clear that each persistence model has no forecasting quality since $\langle s \rangle = 0$ which means that $U = V$ (all the uncertainty is due to the variability).

Comparing the $\langle s \rangle$ values for the NAR and NARX models the $\langle s \rangle$ values are slightly different depending on the normalization factor. When the $I_{clr,poly}$ and $I_{clr,ESRA}$ are used, the difference of the computation of $\langle s \rangle$ leads us within $\pm 1\%$, there is some, although small, sensitivity on forecasting quality when using different normalization factors.

The time series of the developed forecasting models, the persistent model and the measured $I(t)$ values are shown in Fig. 2.8. The lines of the measured values and NARX model predictions are in

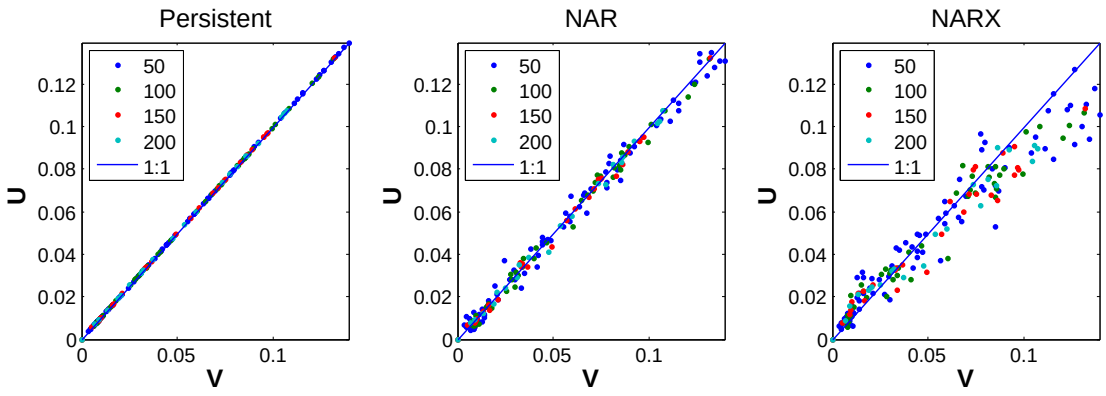

(a) Polynomial

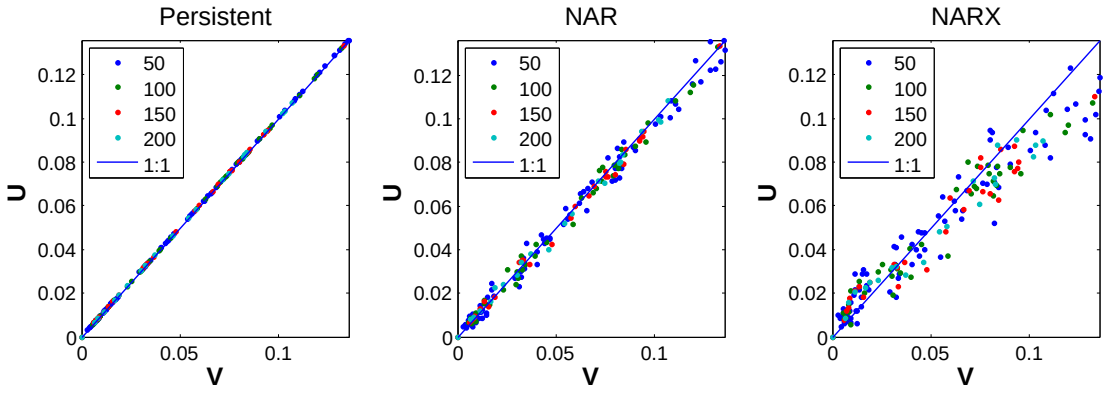

(b) ESRA

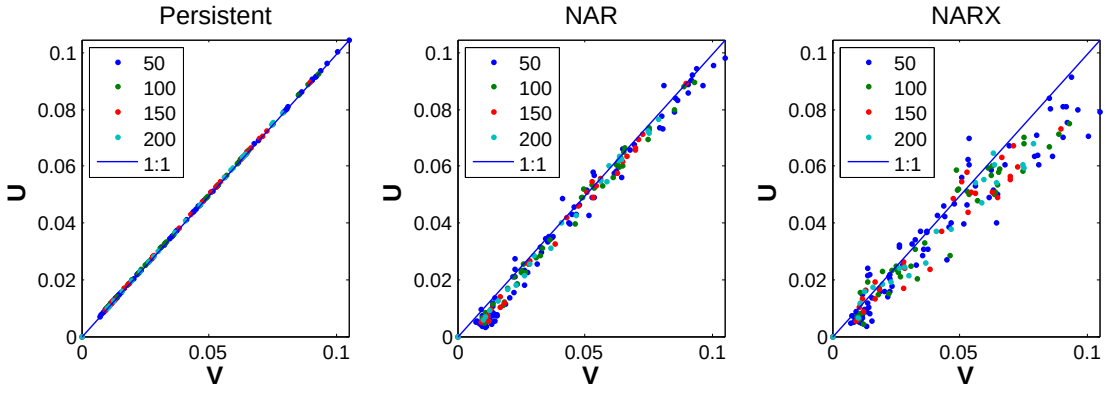

(c) Extraterrestrial

Figure 2.6 – Scatter plot of U and V using various clear sky models including a polynomial-based, the ESRA-based, and the clearness index model which uses Extraterrestrial irradiance for normalization.

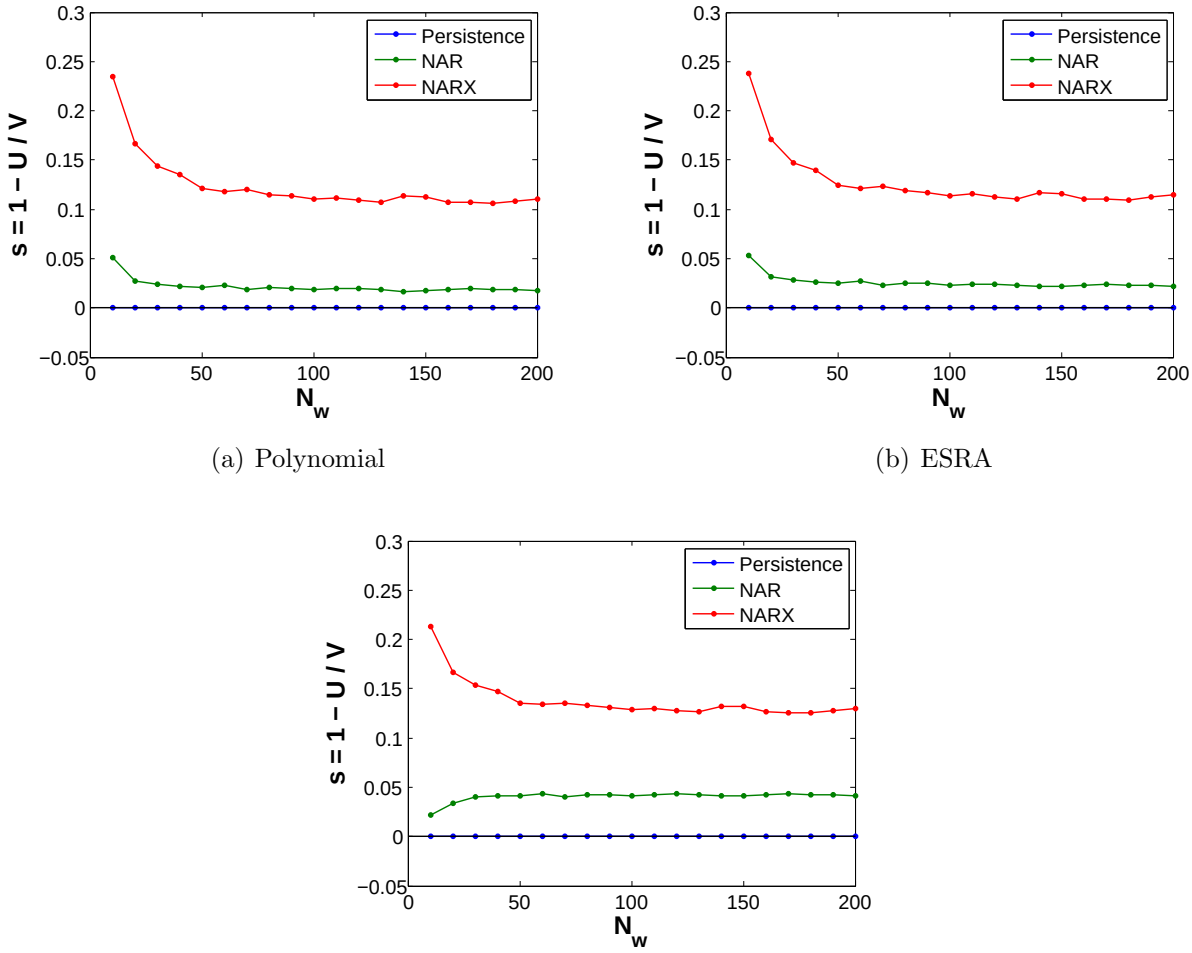

(a) Polynomial

(b) ESRA

(c) Extraterrestrial

Figure 2.7 – Evaluation of $\langle s \rangle = 1 - U/V$ versus N_w (Time-window sizes) after modifying algorithm with different clear sky and persistence models.

bold in order to reduce clutter and also to emphasize the performance of the NARX model which seems to perform the best. This figure illustrates that the models perform similarly well over the clear day. In general, each model performs very well on clear days as opposed to the highly variable days where most of the larger errors occur.

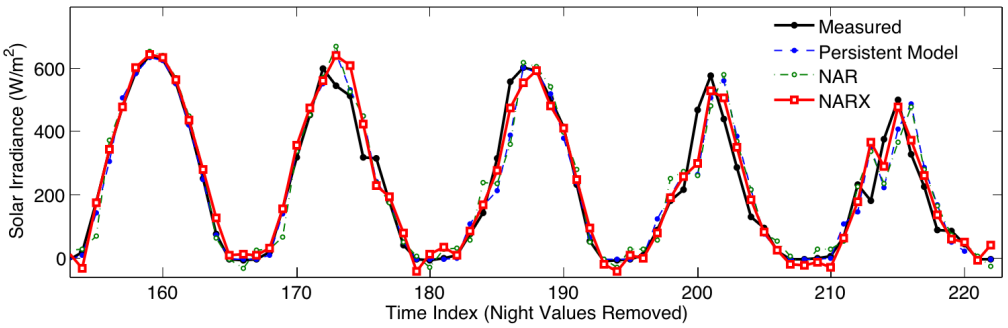

Figure 2.8 – Hourly forecasting comparisons for 5 consecutive days (October 27 – 31, 2010) in the validation data set with night values removed.

2.6.3 Comparison with a Previously Validated Forecast Model

In this section, we show how the NAR and NARX models can be compared to a previously validated forecast model by Perez et al. (2010) [8]. The Perez et al. model is based on Cloud Motion Forecasts (CMF) and was used to validate solar irradiance forecasts of 1–5 hours ahead for several climatically distinct sites for a period spanning from Aug. 23, 2008 – Aug. 31, 2009. In the CMF technique, satellite derived images are used to extract pixel values of clearness index ($k(t)$) at time t. The motions of the clouds are then predicted and are used to determine future images from which values of $k(t+1)$ are inferred. From the $k(t+1)$ predictions, solar irradiance forecasts are obtained. The study in [8] is relevant for comparisons here because the persistent model is defined equivalently to the present work. Specifically, both persistent models make use of the current clearness index value to predict future values of solar irradiance.

The models are compared by observing the improvements over persistency and, furthermore, the improvement over the persistent models are approximate to the proposed metrics, that is, $U/V \approx \text{RMSE}/\text{RMSE}_p$, where RMSE_p is the RMSE of the persistence model. To empirically show this, the RMSEs of the persistent, NAR, and NARX models were calculated using $N_w = 200$ hours then we plot the RMSEs of the NAR and NARX forecasts versus the RMSEs for the persistent model as shown in Fig. 2.9(a). The slopes obtained by the regression fits are equivalent to the slopes describing the average of the ratio U/V. Taking the slope quantities to estimate $\langle s \rangle$ we get values :

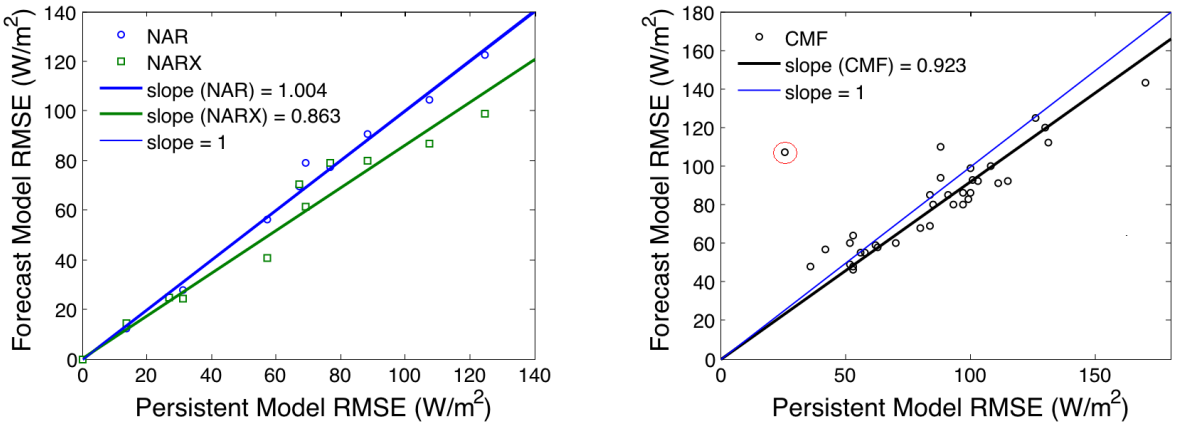

(a) NAR and NARX models

(b) CMF model

Figure 2.9 – Root Mean Square Errors (RMSEs) for different forecast models vs. RMSE of persistent model: (a) NAR and NARX model, and (b) CMF model [8]. The point highlighted with a red circle was ignored for calculating the regression line in (b).

$\langle s \rangle = 1 - 1.004 = -0.4\%$ and $\langle s \rangle = 1 - 0.863 = 13.7\%$, which are approximately equally to those in Table 2.2 for the NAR and NARX models, respectively. The approximate equivlance between U/V and RMSE/RMSEp can also be established from the definitions of U, V, and RMSE and realizing that the normalization factors effectively cancel out when taking the ratios. Estimating U/V with RMSE/RMSEp is much easier than the procedure used to produce the graphs in Fig. 2.9, so this approach is recommended. However, we emphasize here the rational for proposing the metric which is that the metric gives a measure on the effective reduction of random variability (Eqn. (2.13)).

In Table 2 of Ref. [8], RMSEs for 1-hour ahead forecasts of the CMF model and the persistent model are given. These values are used to produce Fig. 2.9(b), where we calculate a regression line after setting the intercept value at zero. The point inside the red circle was considered an outlier and neglected from the fit (for this datum, the persistent model performed much better than the CMF model in terms of the RMSE). Just as the value of $\langle s \rangle$ for the NAR and NARX models from Fig. 2.9(a), the $\langle s \rangle$ value of the CMF model is estimated to be $1 - 0.923 \approx 8\%$. This value is close to the value obtained by NARX model value reported here, therefore, a NARX-type approach seems to produce comparable forecasting performance to the CMF model approach.

2.7 Lorenz et. al. NWP Forecast Study

Here we consider an interesting case to test our proposition that forecasting errors are mainly due to solar variability and to affirm using performance measures that directly compare solar irradiance forecast errors with solar irradiance variability. In [12], solar irradiance forecasts were developed a spatially distributed array of sensors over Germany using a the European Centre for Medium-Range Weather Forecast (ECMWF) Numerical Weather Prediction (NWP) model. An important result highlighted in this study, is the reduction of overall forecasting errors, as evaluated using the RMSE, when averaged over all the sensors. Here we explain their observations of the error reductions using the framework recently proposed by [43] for studying variability for an ensemble of PV systems. According to [43, 35], the variability for a fleet of PV systems can be determined from knowledge of the individual standard deviations $\sigma^i_{\Delta t}$ of the fluctuations and the correlation coefficients $\rho^{i,j}_{\Delta t}$ of the fluctuations for each pair of stations from,

$$\sigma^{Fleet}_{\Delta t} = \frac{1}{N}\sqrt{\sum_{i=1}^{N}\sum_{j=1}^{N}\sigma^i_{\Delta t}\sigma^j_{\Delta t}\rho^{i,j}_{\Delta t}} \tag{2.18}$$

Based on the results obtained in the previous sections of this paper, we anticipate that $U \propto V$, thus we make the assumption that for the forecasts in [12], $\Delta k \propto \varepsilon$, where ε is a forecast error. Using this assumption, we proceed by adapting Hoff and Perez's variability model to the ensemble average solar irradiance forecasting error and also assume that, for all i, $\sigma^i_{\Delta t} = \sigma^1_{\Delta t}$ where now we let $\sigma^i_{\Delta t}$ and $\rho^{i,N}_{\Delta t}$ represent the forecast RMSE and the cross correlation of the forecast errors, respectively. After expanding the first summation we get,

$$\frac{\sigma^{Fleet}_{\Delta t}}{\sigma^1_{\Delta t}} = \frac{1}{N}\sqrt{\left(\sum_{i=1}^{N}\rho^{i,1}_{\Delta t} + \sum_{i=1}^{N}\rho^{i,2}_{\Delta t} + \cdots + \sum_{i=1}^{N}\rho^{i,N}_{\Delta t}\right)}. \tag{2.19}$$

Each summation term can be represented as an average N times the average ($N\ \langle \dots \rangle = \sum \dots$) and, after assuming $\langle \rho_{\Delta t}^{i,1} \rangle = \langle \rho_{\Delta t}^{i,2} \rangle = \cdots = \langle \rho_{\Delta t}^{i,N} \rangle = \langle \rho \rangle$, we reexpress Eqn. (2.19) as,

$$f_R = \frac{\sigma_{\Delta t}^{Fleet}}{\sigma_{\Delta t}^{1}} = \sqrt{\langle \rho \rangle}. \tag{2.20}$$

This equation, which only depends on the cross correlations ($\langle \rho \rangle$), gives us a very simple expression for estimating the reduced combined uncertainty for a network of spatially distributed solar irradiance measurements sites. As it turns out, $\langle \rho \rangle$ (the cross correlations of Δk or ε) can very accurately be modeled as a function of distance x between stations. In fact, when plotting $\langle \rho \rangle$ of Δk (as in [43]) or ε (as in [12]) versus x the plots appear to follow a similar decreasing trend. In [12], $\rho(x)$ was modeled with an exponential parametric function, $\rho = \exp((a_1 x)^{a_2})$, however, the parameters were not given. The fitting function was re-estimated here by selecting points on the model fit of their graph, but this time using the parametric exponential function $\exp(a_3 x^3 + a_2 x^2 + a_1 x + a_0)$. The results are shown in Fig. 2.10 where the selected points are indicated by the square markers and the dashed line is the fit. Using the fit, we approximate the reduced error factor f_R given by Eqn. (2.20) as,

$$f_R(x) = \sqrt{1/x \int_0^x \rho(x')dx'}. \tag{2.21}$$

Applying this equation gives the solid line in Fig. 2.10 which matches closely the observed values obtained from [12].

It is also interesting to point a possible lower bound for f_R which occurs when all the forecast errors are uncorrelated. In this situation, $f_R = 1/\sqrt{N}$ as can be verified from Eqn. 2.20. This is the same result for reduced solar irradiance variability predicted in [32, 35] and observed approximately from experiments in [46, 47] [2].

[2]Ref. [47] finds a $1/\sqrt{S}$ law, where S is the PV plant extension. However, the relation between S and N are closely connected by a dispersion factor, $D = L/V\Delta t$ (see [32]). Alternatively, $1/\sqrt{S}$ can be explained by the correlation coefficients as a function of x as in [43], then realizing that as x (or S) becomes large the correlations tend to vanish, resulting in reduced output variability $1/\sqrt{N}$.

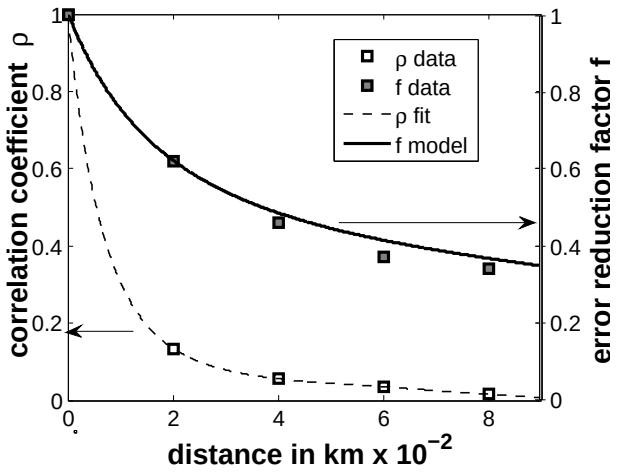

Figure 2.10 – Empirical data compared with modeling predictions of uncertainty (forecast errors) reduction.

2.8 Potential Applications Of Forecast Metric

As compared to a single site, the solar variability can be significantly reduced by distributing solar power generation sites over geographically diverse locations [32, 44]. Building distributed solar power sites can take some time however due to a number of reasons (building permits, capital costs, etc.). One immediate way to avert negative impacts of variability of the solar resource is through reliable forecasting. We demonstrated that a well trained forecasting model has the effect of reducing stochastic variability which is the real concern for solar power. In one sense, the purpose of forecasting is to reduce the amount of stochastic variability because this type of variability is difficult to manage. By applying the proposed metric, we can provide an estimate on the amount of reduced stochastic solar variability and therefore provide some reassurance that some of the solar variability could be handled. If the solar variability is reduced by geographically distributed generation, then the gains are compounded by improved forecasting, as shown in the previous section. In [12], the 'relative' RMSE (rRMSE) for one location are found to be on the order 36%, where as for an ensemble of sites the rRMSE is dramatically reduced to 13% for one-day ahead forecasts.

As recent renewable energy integration studies have reported [5, 4, 6], the variability and intermittency of renewables will likely have significant impacts on reserve and storage requirements. Assuming that the amount of reserve and storage capacity needed to back-up solar energy is proportional to the solar variability, then we can potentially reduce these requirements with reliable forecasting. The forecast metric allows one to estimate by how much a forecasting model will save in storage and reserve requirements. Because the variability of solar irradiance is an important quantity to characterize (e.g., probability of large ramp rates, frequency of fluctuations, etc.) for the purposes of estimating future impacts of including solar energy, it is beneficial to examine historical solar irradiance data sets in order to characterize solar irradiance variability on a temporal and spatial basis. Based on the observations provided here, it can be reasonably expected that a forecasting model, if it is trained well enough over data sets that thoroughly represent the climatology for a given location, should retain their performance in terms of the forecast metric when applied to locations with similar climates. This kind of analysis would be valuable information for simulating impacts due to the uncertainty and variability of solar availability over certain geographical regions of interest.

2.9 Conclusions

A new forecasting metric is proposed and compared to conventional forecasting performance metrics such as root-mean-squared-error (RMSE) and the coefficient of determination (R^2). We showed that the proposed metric is a good indicator of the extent to which a forecast model effectively predicts the stochastic variability of solar radiance. The purpose of forecasting models is essentially to prescribe the non-trivial component of the solar irradiance, and hence improve our understanding of the solar resource variability. The concept is illustrated by comparing three forecast models. One set of models were used as baseline comparisons, where a persistent clearness index is assumed so that the baseline would only incur an error when the solar resource has stochastic variability. As expected, persistent models highly suffer in forecast quality when the solar irradiance exhibits

cloud-induced fluctuations. Two other models based on artificial neural networks were also applied, one of which included short-range moving averages as inputs which did produce effective forecasts by reducing the stochastic variability by 12–20%. In terms of the conventional statistical metrics, each model seems to perform well with R^2 above 90% and RMSEs below 65 W/m^2 over the entire data sets. The advantage of the the proposed metric over the other metrics is that the forecast quality measures seem robust since the ratio U/V over all time window subsets. The novel metric is promising but its invariance should continue to be tested on other cases.

Chapter 3

Intra-Hour DNI Forecasting Based on Cloud Tracking Image Analysis

In the present work, detailed image processing methods aimed at forecasting DNI are presented. Section 3.1 described briefly the data collection procedure. Sections 3.2–3.4 describe processing methods for the images obtained by our TSI. The processing includes the determination of masks, spatial transformations, the computation of the velocity fields, and classification of cloud and clear pixels. In Section 3.5, the methodology for computing grid cloud fractions is described. This methodology defines the variables used for generating the solar forecasts. Solar forecasting errors are computed and evaluated in Section 3.6 with respect to the Root-Means-Squared Errors (RMSEs), and in relation to a persistent model, which is used as the baseline for comparisons with other solar forecasting methods in the literature. Conclusions follow in Section 4.8.

3.1 Data

3.1.1 Total Sky Imager

Images of the sky are taken at one minute intervals at the University of Calfifornia Merced's solar observatory station using Yankee Environmental Systems' TSI-880 instrument [48]. The TSI is

composed of a heated rotating hemispherical mirror with a down-pointing CCD camera located above it. The mirror contains a sun tracking shadow-band that continuously covers the mirror from the the direct sunlight in order to protect the camera sensor from the sun's reflection. The TSI built-in algorithms do not produce cloud classification and dynamic properties such as cloud type, speed, or height, but does produce processed images with pixels representing clear, thin-cloud, and opaque-clouds. The cloud classification algorithm rely on simple R/B thresholds which were developed for cloud fraction estimations. For the forecasting application under consideration here, we instead use our own algorithms (described in Section 3.4), since the built-in cloud classifier does not produce accurate classifications in areas close to the sun's location in the images.

3.1.2 Solar irradiance data

We collected high quality solar irradiance data at the UC Merced Solar Observatory since September 2009. The solar instrumentation used in this study includes Eppley Precision Spectral Pyranometers (PSPs) and Normal Incidence Pyrheliometers (NIPs), with one shaded PSP and one NIP mounted on an Eppley model SMT tracker. The TSI is located within 5 meters of the rest of the solar instruments. Data is logged with a Campbell Scientific CR1000 datalogger at a sampling rate of 2 seconds from which 30-second averages are recorded. In this work, we included only DNI data as measured by an Eppley NIP, which typically deviates from true Absolute Cavity Radiometer (ACR) values by less than 3% (not including obvious errors due to misalignments are tracker stoppage). When broken clouds are present, instrumentation errors of 3% are very small compared to the frequent fluctuations in DNI that can account for full value drops (100%), and amplifications due to cloud edge effects. Predicting these fluctuations is the main goal of this work.

3.2 Processing sky images

Relevant image processing procedures are presented in this section for short-term solar forecasting applications. First, suitable masks are created for the images so that segments such as the protective shadow band and some nearby object appearing on the horizon (such as poles and fences that are not part of the sky) can be discarded. Next, we transform the images onto a rectangular grid so that clouds and velocity fields are more accurately represented. Lastly, we apply simple procedures for cloud determination, which are then used to determine the intensity of the DNI beam. An example of all the steps is shown in Fig. 3.1.

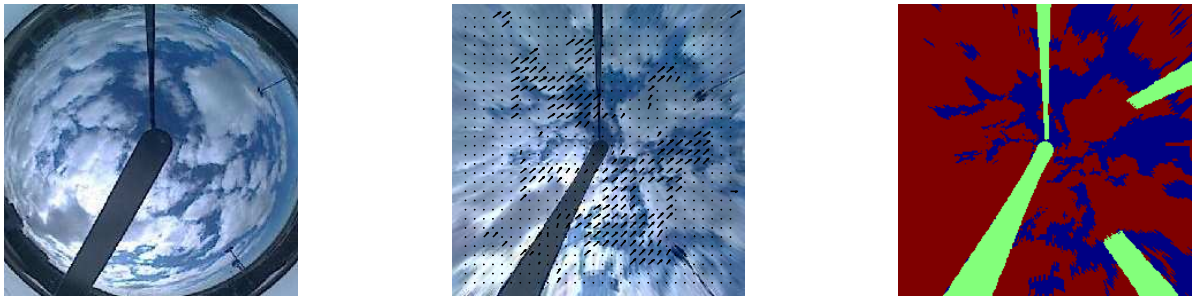

(a) Original image (b) Projected image with velocity field (c) Cloud decision

Figure 3.1 – Main image processing steps. *Left:* Original 8-bit image in RGB color space. *Middle:* Image projected to rectangular grid using derived image to sky mapping, and velocity fields computed using piv algorithm. *Right:* Cloud decision image based on MCE algorithm. Green areas represent false image pixels which are neglected in cloud decision algorithm.

3.2.1 Masks

The shadow band's location is a critical obstruction for DNI predictions, and severely limits the ability of using the TSI for very-short term solar forecasting. Additionally, the glare in the circum-solar region makes it difficult to apply easy rules for replacing the shadow-band pixels with sky pixels, (e. g., which pixels should represent blue-sky or clouds). These difficulties are avoided in

this work by focusing on forecasts with horizons larger than 3 minutes, and by applying masks to effective ignore the effects of areas close to the solar region. The masks are matrices with elements corresponding to locations of the image. The element values are binary (0 or 1) which we use to indicate true or false. Regions where the image is false signals the algorithm to ignore computations in later steps for these locations, and otherwise if the regions are labeled true.

The masks are created by making use of predictable attributes of the images:

1. The images are always enclosed by a circle located of the same size and *position*.

2. The shadow-band and poles are always the same size and shape.

3. The shadow-band moves in a predictable fashion, according to the solar azimuth angle.

We first focus on computing the center of the image and the location of the shadow-band. This task is a suitable application of the function *CircularHough_Grd* available at the Matlab Central File Exchange. The function was developed for detecting various radii in grayscale images via Hough Transforms. The code was written by [49]. Peng's algorithm is used here to detect the outer edges of the sky imager dome, and then to compute a best fit circle by estimating the proper radius and circle center. Because of the random nature of the best fit approximations, there are invariably some differences in the resulting values for a given sequence of images. In some cases the algorithm fails if the lighting is poor such as during rain or highly overcast periods. To maximize its performance, the algorithm is benchmarked on a clear-days. Fig. 3.2 shows an example for March 3, 2011. The histogram of the values for the dome center estimations returned by the algorithm are displayed in Fig. 3.3. The histogram shows that the spread is approximately $\pm$ 3 pixels which is small compared to the total number of pixels (352×288).

After determining the center of the image, we then determine the position of the shadow-band. The dome center was required so that the pivot of the the shadow-band rotation is specified. The orientation of the shadow-band is determined using solar azimuth calculations obtained from [50]. Two other parameters which must specified are the mask are the radius of the inner edge of the

circumference of the dome (the Hough Transform algorithm computed the outer edge because of the higher contrast) and the width of the shadow-band. These parameters are fixed respectively at 130 pixels and 20 pixels. An example of a masks is shown in Fig. 3.4.

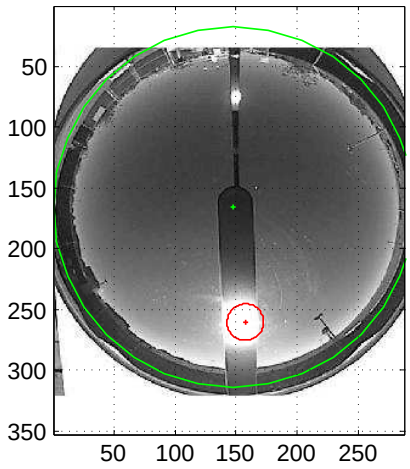

Figure 3.2 – Example of computing the center and radius of the sky imager dome using circHough algorithm. For this case the center is $x_c = [161.6072, 164.3110]^T$ and the radius of the dome is $r_{dome} = 157$. Image was taken on 2011/03/02 13:39 PST.

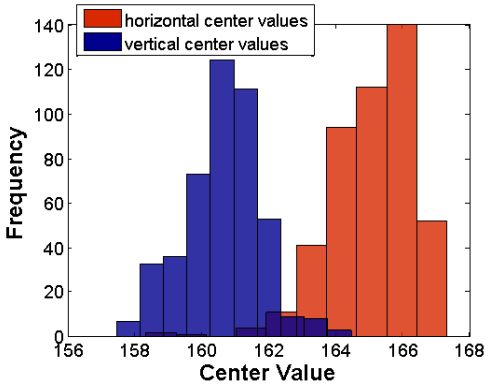

Figure 3.3 – Histogram of horizontal and vertical center values determined using center detection algorithm. The used data was obtained for 2011/03/02 at 5 minute interval samples. The total number of images used for that day were 457. This figure shows that there is some randomness of $\pm$ 3 pixels in the resulting center point determination.

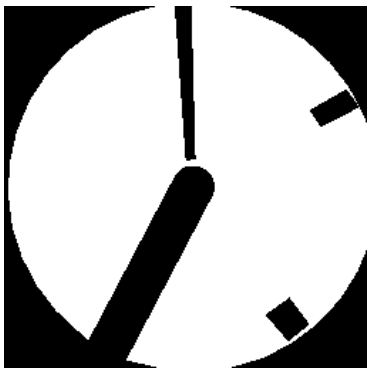

Figure 3.4 – Example of a Mask for the same image shown in Fig. 3.1.

3.2.2 Transformations to Rectangular Grid

This section covers the approach used to transform the images from a spherical to rectangular grid. Because of the shape of the TSI mirror and the unknown location of the focal point of the camera it is difficult to determine on a geometric-optics basis the transformation equation to map points on the image to actual points on the sky. The complicated geometrical optics is avoided by using knowledge of the solar zenith angles and the sun's apparent position in the image to arrive at the desired transformation. The image pixel locations are first represented in polar coordinates,

$$x_i = r_i \cos(\phi), \qquad y_i = r_i \cos(\phi), \tag{3.1}$$

where r_m is the radial distance from the center of the TSI raw image to the coordinate $[x_i, y_i]$, and ϕ is the azimuth angle with respect to the horizontal axis (East to West on the image). The rectangular grid (sky) coordinates are represented as,

$$x_s = r_s \cos(\phi), \qquad y_s = r_s \cos(\phi), \tag{3.2}$$

where r_s is the radial distance for rectangular grid coordinates (sky). Corresponding pixels in either coordinate frame share the same values for the polar angle ϕ, therefore the mapping is accomplished

by determining the relationship between r_i and r_s. This relationship is obtained by considering the solar zenith angle (θ_{sz}) which is known at any given time (see [50] for θ_{sz} angle calculations), and the Sun's position on the image (r_i) determined using, again, the Hough transform algorithm. An example is shown in Fig. 3.2. The sky radial distance (r_s) can be computed given the zenith angle as,

$$r_s = \tan^{-1}(\theta_{sz}). \tag{3.3}$$

The mapping $r_s \rightarrow r_i$ is approximated by curve fitting r_m with θ_{sz}. We selected three days and computed θ_{sz}, and determined r_i using, again, the Matlab routines to find circles which best fit around the Sun in each image and determined that the best fit cubic polynomial is adequate for the mapping, since the y-intercept falls close to zero and the curvature of plots were accurately modeled (see Fig. 3.5). The mapping from the true sky position to the mirror position is,

$$\begin{aligned} r_s &= \sqrt{x_s^2 + y_s^2} && (3.4)\\ \theta_z &= \tan^{-1}(r_s) && (3.5)\\ r_i &= r_i(\theta_z; \text{according to curve fit results}) && (3.6)\\ [x_i,\ y_i] &= r_i\,[\cos(\phi),\ \sin(\phi)]\,. && (3.7) \end{aligned}$$

The above equations define the projections from the apparent positions in the image to a flat sky. An example of the image projections is shown in Fig. 3.1(b).

3.3 Computing Velocity Fields

3.3.1 Particle Image Velocimetry

We use an 'MPIV' toolbox developed by [51] to obtain the cloud velocity fields. The interrogation window is defined by a 32 pixels × 32 pixels area, and the overlap between two consecutive windows is set to 50%, with maximum displacements set to 20 pixels for both vertical and horizontal direc-

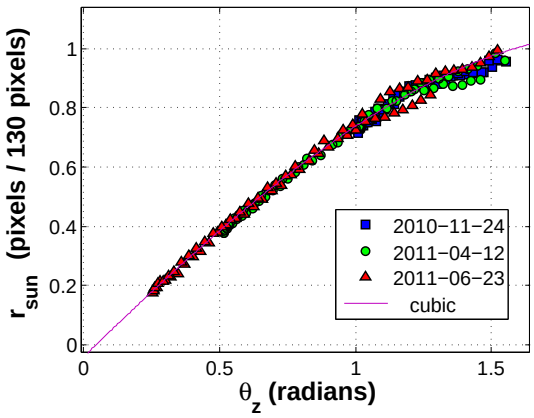

Figure 3.5 – Radial distance of solar position to center and solar zenith angles computed for three days as shown in legend. June 23 is solar summer solstice and is the longest day of the year. This day also has the highest solar zenith angle of all days of the year and is therefore used for the curve-fitting.

tions. The MQD (Minimum Quadratic Difference) method [51] is used with two recursive checks. The velocity field is filtered and smoothed by the functions in the 'MPIV' toolbox. The sequence of images are given at 1-minute apart. An example of a velocity field calculation is shown in Fig. 3.1(b). A detailed description of the Particle Image Velocimetry (PIV) methods used here can be found in [51].

Qualitatively, the PIV algorithm seems to perform well, although it is not always possible to retrieve velocity fields from less well defined clouds. One way to evaluate the velocity vector output is to calculate matching errors, as was done by [23]. However, because clouds are always deforming (there are also artificial deformations due to the mirror curvature and image projections), the matching errors do not accurately represent the quality of the velocity field output. Therefore we do not compute the matching errors or further evaluate the velocity vector output other than using visual inspection. Because our goal is to use a stochastic learning method that will be able to learn from these translations errors over time, we assume that some 'learnable' translation error can be easily overcome by the stochastic learning techniques.

3.3.2 Selecting a representative velocity vector

For each image, several velocity vectors are computed depending on the local motions of clouds at points (x_i, y_i). The following analysis is simplified by selecting a representative vector for each image. The representative velocity vector is chosen by applying $k-$means clustering on the distribution of velocity vectors. In parts of the image where clouds are absent, zero velocity vectors are computed and thus each image will usually have a cluster of velocity vectors near to or at zero. We therefore cluster each velocity field around 2 cluster means, which are determined using a cluster means algorithm. The larger (in magnitude) of the cluster means is chosen as the representative velocity vector. Fig. 3.6 shows an example of using the $k-$means clustering algorithm to select a single representative velocity vector.

Based on Fig. 3.6, the velocity vector: $(u = 6.0, v = -4.6)$ pixels/minute is chosen as the velocity vector for estimating cloud motion. For instance, we can estimate that the time that it takes for a cloud to pass through the range of the sky seen by the TSI by taking the total number of pixels (255), say in the horizontal distance, then dividing by the horizontal velocity (6.0 pixels/minute), and calculating that it takes approximately 42 minutes for a cloud to cross the observable range of the sky for these conditions. For applications, the utility time of using the TSI for solar irradiance forecasting is about 1/3 of the estimated 42 minutes since more than 1 pixel is need for advection (or to be useful for making predictions). The longest time-scales for which the TSI is useful for predictions is approximately 12-18 minutes.

3.4 Cloud pixel identification

Perhaps the most important step in using a TSI for solar forecasting is automating the identification of cloud pixels of the images. A common approach is to use the red and blue channels of the image [52, 53, 54, 55]. The clear sky is characterized by high blue intensities and low red intensities, whereas, pixels with clouds are characterized by higher intensities in both channels. The distinctions

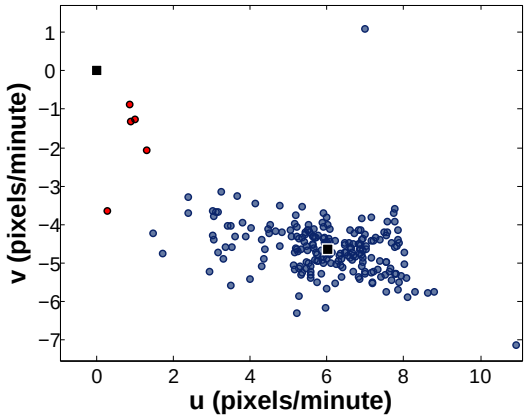

Figure 3.6 – Clustering velocity field using $k-$means algorithm. Velocity cluster mean at zero represents the clusters of velocities computed at blue parts of sky. The non-zero velocity cluster mean at $(u = 6.0, v = -4.6)$ pixels/minute is selected as the representative velocity vector for the image.

are more fuzzy when there are thin clouds and bright areas caused by large amounts of scattering in the solar region of the images, making it more difficult to apply a universal threshold for cloud pixel classification. Here we follow the approach recently described by [55] which employs an adaptive threshold scheme. The algorithm determines the cloud pixels by selecting the threshold as the minimizer of the cross-entropy between the B/R normalized ratio image and the segmented image (B_t).

The normalized B/R ratio defined by [55] is given by

$$\lambda_n = (b - r)/(b + r), \tag{3.8}$$

where b and r refer to the values of blue and the red channel, respectively. To identify clouds, a threshold (t) is specified which segments the clear and cloudy parts of the sky. The new segmented image B_t is related to the image of λ_n intensities by,

$$B_t(x, y) = \begin{cases} \mu(1, t), & \lambda_n(x, y) < t \\ \mu(t + 1, L), & \lambda_n(x, y) \geq t \end{cases}, \tag{3.9}$$

where x and y denote the coordinate of a pixel and $\mu(a,b)$ is defined as

$$\mu(a,b) = \sum_{a}^{b} ih(i) / \sum_{a}^{b} h(i). \tag{3.10}$$

The threshold hold is set to the minimizer of the cross-entropy between I_N and B_t, which results in,

$$\begin{aligned} t^* &= \arg\min\{-m(1,t)\log\left(\mu(1,t)\right) \\ &\quad -m(t+1,L)\log\left[\mu(t+1,L)\right]\}, \end{aligned} \tag{3.11}$$

where $m(a,b) = \sum_{i=a}^{b} ih(i)$. This classification algorithm, referred to as the MCE (Minimum Cross Entropy) algorithm, was developed and tested in [55] as part of the HYTA (HYbrid Threshold Algorithm). The MCE is meant to be applied to images with bimodal B/R histograms. The MCE is applicable in our case, since we are mainly interested only in days with mostly broken clouds.

Two modifications to the MCE algorithm were made. Firstly, we decided that whenever $t^* > 0.3$ or $t^* < 0.2$, the cloud decision images were (by visual inspection) unsatisfactory. Therefore, we decided to limit t^* in the interval $0.2 \leq t^* \leq 0.3$. The second modification includes making the adaptive thresholds localized depending on masks, which are used to partition the image in four regions. The four regions are illustrated in Fig 3.7 after transforming the masks using the same cropping and spatial projections as the original image. For convenience, the perimeters of the regions are overlayed on the original image. The colors represent the true parts for each of the four masks. The first mask (blue) is true at points enclosed by a circle of 60 pixel radius with center at the sun's position. The second mask (cyan) is true for pixel values enclosed by an arc which subtend 90° with sector originating from the center of the image, but not including pixels in the first mask. The third mask (yellow) is true for pixels enclosed by a circle of radius 100 pixels, but not including the first and second masks. The fourth mask, includes any pixels not covered by the first, second, and third masks. Each local t^* values are computed in the union of each masks and the masks and

the mask derived in Section 3.2.1. The resulting cloud indexed images are then combined into a single cloud decision image (e.g., Fig. 3.1(c)).

(a) The 4 Masks used to partition images.

(b) Mask perimeters overlayed on original image.

Figure 3.7 – Masks used for partitioning image into 4 regions for separate cloud classification thresholds. *Right:* Each color represents a different mask; M_1: blue, M_2: cyan, M_3: yellow, M_4: red. *Left:* Perimeters of masks overlayed on original image.

3.5 Grid Cloud Fractions

In order to forecast solar irradiance, we first construct a set of grid elements oriented column-wise in the reverse direction of the cloud flow field. The direction is obtained from the representative velocity vectors, described in Section 3.3. At each instant, the velocity vectors are averaged over the last 10 sequences, so that the velocity time-series is smoother since much of the fluctuations in the velocity computations are due to random computational errors. Figure 3.8 illustrates the orientations. The column of grid elements distance from the sun region and each grid element is denoted as variable $X_1, X_2, \ldots, X_6$ in ascending order as the grid element is away from the sun region. The size of the regions are each 20×20 pixels. For the $i-$th grid element, the calculated cloud fractions at time t is assigned to $X_i(t)$. These grid cloud fraction values are used to make solar forecast predictions for several time-horizons. In some cases, the grid elements overlap regions where masks are set to false. In these situations, the overlap sections are ignored in the cloud

fraction computations. If the grid element completely overlaps a false section, the resulting cloud fraction is ignored in the forecasting evaluations.

This approach relies solely on the direction of the velocity vectors. The speed given by the velocity vectors is not used in this formulation, but we should note that the speed is accounted for by the distance the grid elements to the position of the Sun and the size of the grid elements (20 pixels $\times$ pixels). By making use of the definition of speed (speed = distance/time) some additional points can be made. Assuming constant (in time) velocity fields, grid elements further out correspond to longer forecasting horizons. For example, if the average velocity speed is 20 pixels/minute, then the grid element which contains the best information for a 5 minute forecasting horizon should be a distance of 10 pixels/minute $\times$ 5 minutes = 50 pixels. This distance corresponds to the third grid element whose midpoint is also 50 pixels from the sun position. The size of the grid elements correspond to the time-averaging of the solar irradiance. Since we are computing 1-minute averages, we can argue that the size of the pixels should by 10×10 pixels (assuming again cloud speeds of 10 pixels/minute). This size was found to be to sensitive to misidentification of clouds, thus we increased the size of the pixels to 20 pixels $\times$ 20 pixels. We also decided to keep 1-minute averaged solar irradiance, instead of computing 2-minute averages.

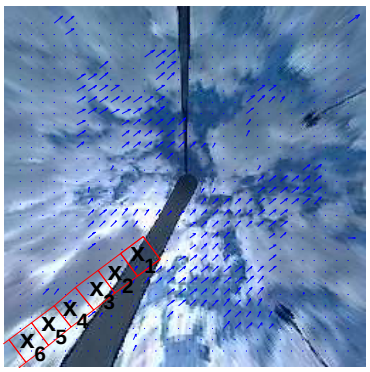

Figure 3.8 – The squares indicate regions of interest assigned for variables $X_1, \ldots, X_6$. Each variable represents the computed cloud fraction in the designated regions.

Table 3.1 – Days used in forecasting evaluations and corresponding velocity and irradiance statistics. The velocity directions are given in units of degrees with respect to the East to West axis.

Day	Ave. Speed (pixels/min)	Std Speed (pixels/min)	Ave Direction (°)	Std Direction (°)	Ave DNI (kW/m^2)	Std DNI (kW/m^2)
June 1, 2011	6.06	0.86	-56.25	17.71	0.44	0.40
June 5, 2011	11.62	1.51	-110.48	11.66	0.57	0.38
October 5, 2011	8.06	2.06	17.10	13.43	0.57	0.34
November 4, 2011	7.84	4.48	27.86	38.35	0.63	0.31

3.6 Forecasting Direct Normal Irradiation

In the following calculations we selected four days to apply the DNI forecasting algorithm. The four days selected are given in Table 3.1. These days for the nature of their cumuliform clouds (which facilitate cloud classification), but also for being highly variable DNI days.

3.6.1 Evaluation of Errors

We test 1-minute averaged direct normal irradiance forecasts for time horizons (Δt) of 3–15 minutes. To compare the cloud fractions with DNI values, each variable $X_i(t)$ is subtracted from 1 and then multiplied by $G_{B,m}$.

$$X_i(t)' = G_{B,m}(1 - X_i(t)) \tag{3.12}$$

We subtract from 1 is because of the inverse relationship between cloud fraction and DNI intensity. $G_{B,m}$ is the maximum beam irradiance (DNI) value for the days analyzed, which is set to a constant value of 0.9 kW/m^2 for this study. The errors are summarized by calculating Root-Mean-Squared Errors (RMSEs), which are computed for each variable and for each forecasting horizon as

$$RMSE(\Delta t, i) = \sqrt{1/N \sum_{t \in T} (DNI(t + \Delta t) - X_i(t)')^2}, \tag{3.13}$$

where the summation is carried out in the set $T = 10:00$ to $14:00$ corresponding to 4 hours of the evaluated day. We also include the persistence forecast for which the RMSE is

$$RMSE_p(\Delta t) = \sqrt{1/N \sum_{t \in T} (DNI(t + \Delta t) - DNI(t))^2}. \tag{3.14}$$

The persistent model represents the simplest forecasting model one can use. It represents the situation where no information is available to forecast with other than the current value. Also, as discussed in [2], the RMSEs of the persistence model also roughly represents the variability of the solar irradiance, as defined in [32]. Essentially, when the variability is low, an appropriately defined persistence model produces very accurate forecasts and therefore any forecast model which shows improvement over the persistence is reducing *random* variability [2].

The forecasting approach is applied to 4 days including June 1, 2011; June 5, 2011; October 5, 2011; and November 4, 2011. Cloud speeds and DNI attributes for these days are summarized in Table 3.1. These days were selected because of the satisfactory cloud decisions that were obtained using the algorithm described in Section 3.4.

Tables 3.2 show the RMSEs as calculated by Eqs (3.13) and (3.14) for each variable X_i and the persistence model. The forecasting horizons are denoted in the 1-st column of the table. Each sub-table corresponds to a different day. According to each of the sub-tables, there is a clear trend in the variable performance and the time horizon. Variables representing grid elements further away from the solar region are more useful for predicting DNI at longer time horizons. The most accurate forecasts appear to be for 5-minutes ahead.

Table 3.2 – Root-Mean-Squared Errors (RMSEs) in kW/m^2 computed for forecasting horizons of 3–15 minutes as indicated in 1-st columns. Bold-faced numbers represent best RMSE with respect to time forecasting horizon. Generally, grid element variables located further away are more useful for longer forecast horizons.

(a) June 1, 2011

Forecast Horizon	*Persistent*	X_1	X_2	X_3	X_4	X_5	X_6
3	0.437	**0.361**	0.444	0.518	0.531	0.565	0.576
4	0.475	**0.286**	0.406	0.494	0.519	0.558	0.564
5	0.495	**0.226**	0.371	0.473	0.504	0.549	0.555
6	0.496	**0.238**	0.334	0.450	0.492	0.533	0.545
7	0.504	**0.292**	0.307	0.427	0.476	0.514	0.533
8	0.518	0.354	**0.300**	0.400	0.455	0.496	0.522
9	0.535	0.400	**0.316**	0.367	0.433	0.480	0.507
10	0.547	0.431	0.343	**0.341**	0.404	0.458	0.496
11	0.545	0.446	0.367	**0.336**	0.376	0.429	0.477
12	0.554	0.457	0.388	0.355	**0.351**	0.403	0.451
13	0.570	0.466	0.399	0.3753	**0.346**	0.372	0.422
14	0.586	0.482	0.411	0.392	**0.358**	0.358	0.398
15	0.596	0.493	0.433	0.405	0.370	**0.360**	0.378

(b) June 5, 2011

Forecast Horizon	*Persistent*	X_1	X_2	X_3	X_4	X_5	X_6
3	0.279	**0.258**	0.28012	0.313	0.333	0.347	0.361
4	0.301	**0.213**	0.24172	0.293	0.321	0.343	0.345
5	0.326	0.236	**0.208**	0.274	0.307	0.334	0.335
6	0.360	0.283	**0.224**	0.250	0.296	0.323	0.331
7	0.379	0.312	0.261	**0.242**	0.278	0.317	0.326
8	0.390	0.328	0.279	**0.269**	0.277	0.308	0.325
9	0.403	0.346	0.316	**0.294**	0.305	0.312	0.330
10	0.415	0.368	0.338	**0.317**	0.325	0.327	0.341
11	0.424	0.392	0.355	**0.337**	0.337	0.332	0.349
12	0.436	0.410	0.377	0.355	**0.350**	0.345	0.353
13	0.455	0.417	0.398	0.374	**0.370**	0.366	0.360
14	0.463	0.421	0.413	0.394	0.387	**0.385**	0.373
15	0.467	0.433	0.420	0.412	0.401	0.402	**0.392**

(c) October 5, 2011

Forecast Horizon	*Persistent*	X_1	X_2	X_3	X_4	X_5	X_6
3	0.352	**0.276**	0.264	0.302	0.331	0.375	0.377
4	0.376	0.317	**0.252**	0.310	0.319	0.360	0.374
5	0.401	0.360	**0.267**	0.306	0.318	0.348	0.366
6	0.412	0.399	**0.293**	0.294	0.318	0.341	0.359
7	0.427	0.421	0.330	**0.289**	0.314	0.348	0.358
8	0.442	0.445	0.361	**0.305**	0.307	0.356	0.367
9	0.451	0.468	0.389	0.322	**0.300**	0.355	0.370
10	0.453	0.479	0.409	0.345	**0.303**	0.344	0.372
11	0.453	0.487	0.422	0.359	**0.317**	0.341	0.367
12	0.451	0.496	0.424	0.361	0.334	**0.332**	0.362
13	0.454	0.497	0.431	0.353	0.347	**0.328**	0.349
14	0.463	0.496	0.433	0.352	0.352	**0.331**	0.340
15	0.475	0.496	0.438	0.356	0.356	0.335	**0.332**

(d) November 4, 2011

Forecast Horizon	*Persistent*	X_1	X_2	X_3	X_4	X_5	X_6
3	0.309	**0.237**	0.329	0.395	0.416	0.408	0.408
4	0.322	**0.217**	0.312	0.392	0.415	0.414	0.414
5	0.338	**0.257**	0.302	0.383	0.412	0.420	0.420
6	0.352	**0.286**	0.304	0.375	0.411	0.428	0.428
7	0.361	**0.292**	0.305	0.366	0.409	0.440	0.440
8	0.368	**0.298**	0.299	0.359	0.396	0.437	0.437
9	0.375	0.305	**0.291**	0.360	0.386	0.433	0.433
10	0.390	0.311	**0.283**	0.356	0.380	0.430	0.430
11	0.412	0.315	**0.275**	0.339	0.373	0.424	0.424
12	0.433	0.320	**0.267**	0.317	0.371	0.42	0.425
13	0.447	0.336	**0.276**	0.297	0.365	0.426	0.426
14	0.461	0.358	**0.291**	0.291	0.359	0.424	0.424
15	0.473	0.380	0.307	**0.299**	0.354	0.424	0.424

Time-series plots of the measured values and the forecasts are shown in Fig. 3.9 for 5-minute ahead forecasting. The persistence model is also shown. The main characteristic of the persistence model is the lagged response to the effects of clouds. We can see from these figures that the forecasts show considerable improvement over the persistence to predict the onset of transitions from clear to cloudy and cloudy to clear conditions. During periods where there is high frequency of fluctuations, the forecasts do not overlap the measured values as well.

3.6.2 Forecast quality comparisons

The DNI forecasting errors are evaluated further by making comparisons with the errors of the persistence model. Taking the RMSE data of the best models and the persistence model from Table 3.2, we produced Figure 3.10. This Figure, again shows that the optimal forecast period is for five minutes ahead. For each day analyzed, there are significant improvements over the forecast period with RMSEs on average approximately 30 W/m^2. To get an indication of the quality of the forecast models, we show in Fig. 3.11 the same RMSEs in Fig. 3.10, but this time plotting the RMSEs of the forecast versus the RMSEs of the persistence model. Although there is some scatter, a general trend is apparent, which indicates that the forecast RMSEs increases with the persistence model RMSEs. In analogy with [2], the ratio of the RMSEs is approximated with the slope of a linear fit to the scatter data. In this case, we approximate the slopes to range between 0.6 and 0.8, which means that the forecast quality of the models as a measure of improvement over a persistence model are between $1 - RMSE/RMSE_p \approx 1 - 0.8 = 20\%$ and $1 - RMSE/RMSE_p \approx 1 - 0.6 = 40\%$, with higher values indicate better forecasting quality. The improvement in forecasting skill is competitive in terms of other forecasting models described in the literature for different time horizons. For 1-hour ahead forecasting, [3] obtained 8–10% improvement over persistence using cloud motion forecasts from satellite images; [2] obtained 12–20% using a ANNs; and [11] obtained 10–15% also using ANNs. Unfortunately, direct comparisons are difficult to evaluate due to regional meteorological conditions and different time horizons. Nonetheless, our preliminary study shows that within the

Table 3.3 – Evaluation of excessive ramps due to forecast errors of the developed models and the persistence. The critical ramp rate is set to 0.60 kW/m^2. Numerical values are estimated from plot in Fig. 3.12.

day	$P(\|E_f\| < 0.6\ kW/m^2)$	$P(\|E_p\| < 0.6\ kW/m^2)$
June 1, 2011	0.76	0.67
June 5, 2011	0.92	0.87
October 5, 2011	0.86	0.78
November 4, 2011	0.90	0.86

15 minute time horizon, forecasting with sky image processing shows promise, especially if coupled with stochastic learning techniques that can offset some of the image classification and translation issues described above.

3.6.3 Forecasting of large variations (ramps)

A major concern with the utilization of solar energy systems for the production of electricity is the potential instabilities that can occur during large ramping events. Solar irradiance forecast can be used for decision making to circumvent those hazards. For these evaluations, we take the absolute values of the errors obtained for 5-minute ahead forecasts ($|E_f|$), as well as the errors of the persistence model ($|E_p||$), and plot the cumulative distribution function in Fig. 3.12. A critical ramp rate (critical error) is assigned at 0.60 kW/m^2 as depicted by the vertical line. From this figure for example, following the intersection of the vertical line and the line for say the persistence model on June 1, 2011 (blue dashed line), we can estimate the probability that a ramp of less 0.60 kW/m^2 occurred 67% of the time. Alternatively, we also estimate that a ramp of larger than 0.60 kW/m^2 occurred $1-0.67 = 33\%$ of the time. The analysis is carried fore each of the days considered in Table 3.3. Essentially, the more area under the curve, the less likely an unexpected large ramp event will occur, and in this way we can see some of the benefit of using the solar irradiance forecast.

3.7 Conclusions

The work presented here makes significant progress in our ability to forecast DNI for time horizons shorter than 15 minutes. Procedures for image processing were applied, including the development of a spatial transformation to map the image obtained by a hemispherical mirror to locations on a flat grid, application of a PIV routine [51] to compute velocity fields and the determination of a representative velocity vector using a $k-means$ algorithm, and an application of the a modification of the technique developed by [55] for pixel cloud classification. We introduced an approach for computing cloud fractions of grid elements oriented in such a way to scan the image according the computed velocity vectors. The computed cloud fractions were used for forecasting DNI. Evaluations of the RMSE errors demonstrate that TSIs are useful for 3–15 minute ahead forecasting horizons. We chose 4 highly variable days to demonstrate the methodology. While 4 days may seem to few, a limited number of days is in fact more relevant to evaluate short-term forecasts than a very large period including many clear days because clear days tend to affect the error averages (there is essentially no forecast errors for either clear days or consistently cloudy days). The comparison is also made in respect to a persistent model, which is reasonably accurate for very short times. Results of the solar forecasting method are very encouraging despite some difficulty in cloud identification. Comparing with a persistent model, it appears that the most accurate forecasts are for 5-minutes ahead, but the TSI approach is still very useful even for 15-minutes ahead. Previous work using sky imagers highlighted intrinsic difficulties with achieving robust image cloud classifications [52, 23, 55, 22, 53], in particular for images with large amounts of glaring. We experienced similar difficulties with this work. We anticipate that improved cloud classification of images plus the incorporation of stochastic learning techniques for translation error reduction will contribute significantly to forecasting accuracy at short term horizons.

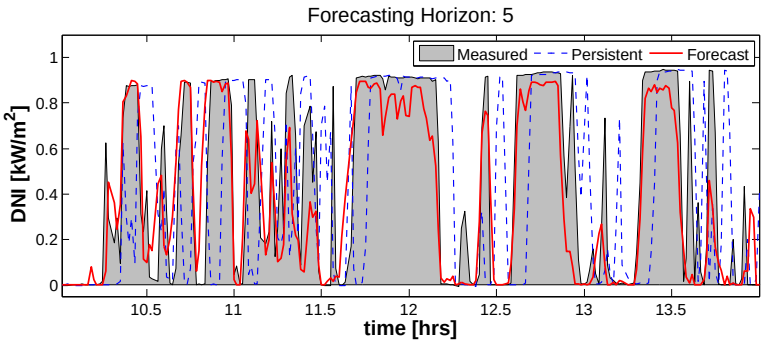

(a) June 1, 2011

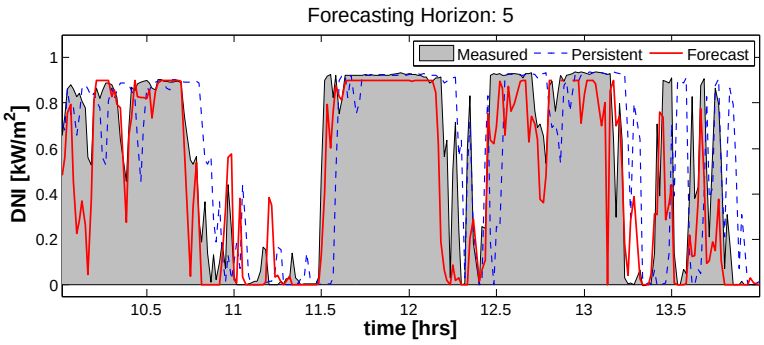

(b) June 5, 2011

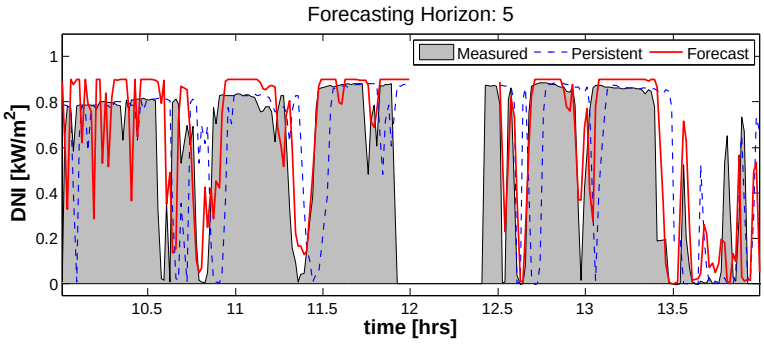

(c) October 5, 2011

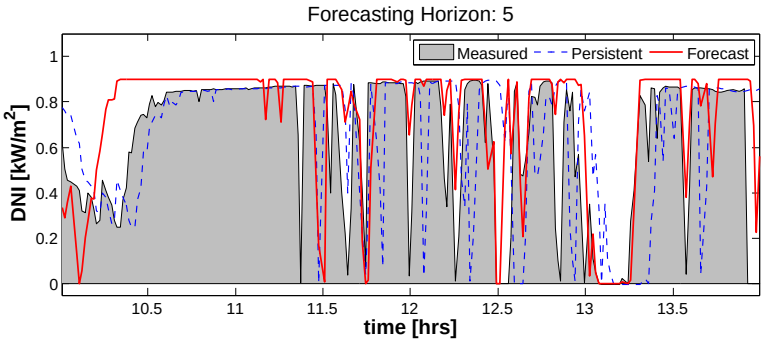

(d) November 4, 2011

Figure 3.9 – 5-minute ahead forecasting of 1-minute averaged DNI values for the 4 evaluated days. The time-series range from 10:00 to 14:00 PDT. Value between 12:00 to 12:30 were removed because of poor cloud classification of cirrus clouds.

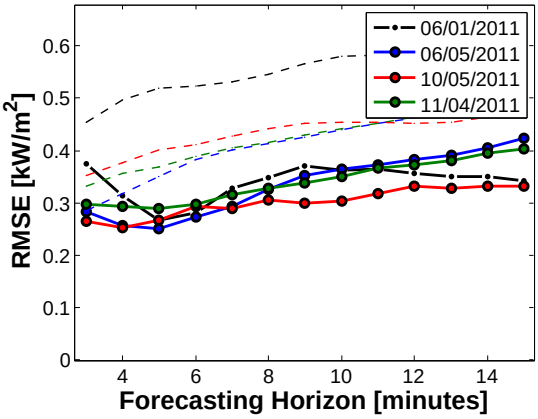

Figure 3.10 – RMSEs and forecast horizons . Bold lines with markers denote the *best* forecast RMSE for the forecast horizon and dashed thin lines denote the persistent RMSEs. The optimal forecast period appears to be for 5-minutes ahead.

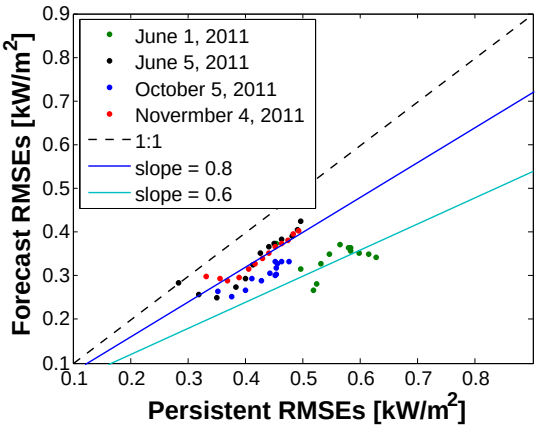

Figure 3.11 – Comparing *best* RMSEs with persistent model RMSEs to evaluate 'forecast quality'. The slope of 0.8 suggests that the forecast quality is between $1 - RMSE/RMSE_{persistent} \approx 1 - 0.8 = 20\%$ and $1 - RMSE/RMSE_{persistent} \approx 1 - 0.6 = 40\%$. See [2] for a detailed discussion on solar forecasting evaluations.

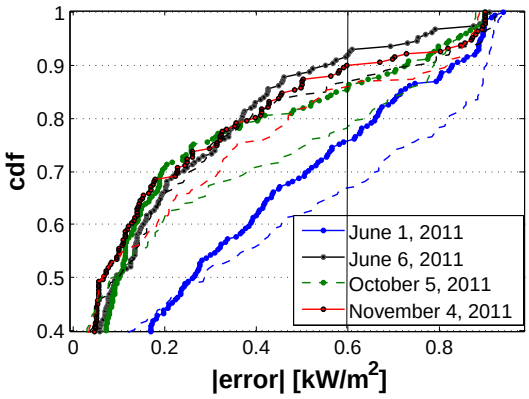

Figure 3.12 – Cumulative distribution function of the absolute value of the errors for 5-minute ahead forecasts. The lines with markers denote errors of the forecast models, and the dashed lines denote errors of the persistence models. The vertical line is used for computing probabilities of errors below the 0.6 kW/m^2 critical value in Table 3.3.

Chapter 4

Forecasting Solar Irradiance With GOES-West Satellite Images And Artifical Neural Networks

This work describes an approach based on satellite images and Artificial Neural Networks (ANNs) for time-series predictions to forecast the global horizontal solar irradiance (GHI) for forecasting horizons of T = 30, 60, 90, and 120 minutes ahead. The forecast model is applied to GHI data gathered from the UC Davis and UC Merced solar observatory nodes which adequately represent the Central Region of California. The forecasting approach involves information gathered from satellite image analysis including velocimetry and cloud indexing to include in an ANN model. To the best of our knowledge, this model is a first step towards hybridizing a physics and statical approach using satellite imagery for solar forecasting applications. The developed forecast models are comprehensively compared, where possible, with other existing forecast model performances in the literature using forecast skill as the applicable metric for forecast performance comparisons.

4.1 Introduction

Accommodating large-scale solar power to the grid requires the use of highly accurate forecasting capabilities in order to maintain the number of reserves that are used to back-up load and power

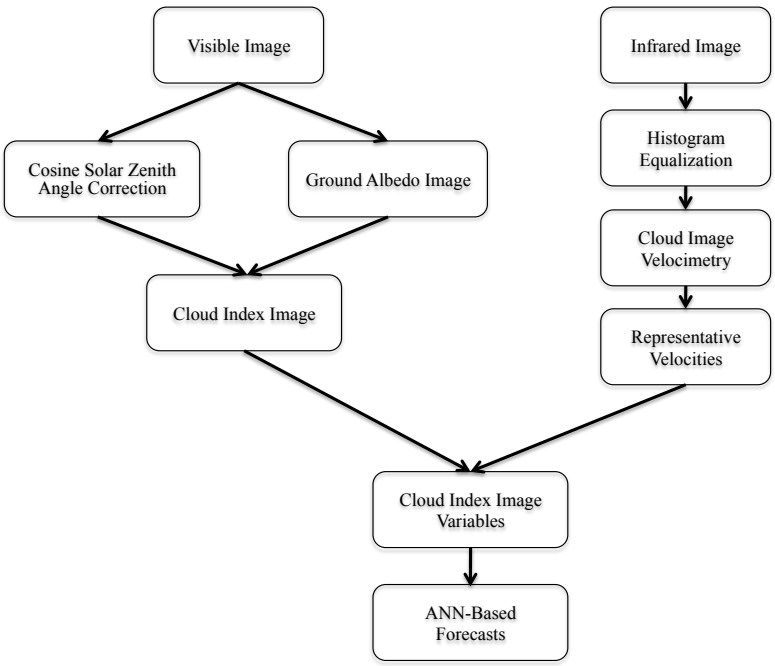

Figure 4.1 – Schematic of solar forecast modeling methodology which includes 3 stages – cloud indexing, image velocimetry, and ANN predictions.

generation variability [4, 5]. The focus of this work is to develop solar irradiance forecasts for lead-times of 30-minutes to 2-hours. The solar forecasts are developed for two locations in the Central Valley of California using information extracted from GOES-West satellite images and incorporated with Artificial Neural Networks (ANNs) for time-series predictions.

The organization of this chapter is as follows. It starts with an overview of the methodology in Section 4.2, which discusses the methodology as composed of three distinct stages. In Sections 4.3 and 4.4, the satellite-image processing including cloud indexing and image velocimetry stages are explained. Section 4.5 describes the methodology of constructing and incorporating input variables for the ANN forecasting models. The configuration and training of the ANN models are described in Section 4.6 and the models are evaluated in Section 4.7. Conclusions are given in Section 4.8.

4.2 Forecast Model Overview

The proposed methodology is based on combining the strengths of ANNs for time-series predictions with information from satellite images. An ANN forecasting model that uses information of lagged values single or multivariate time-series can be written generally as,

$$y(t+T) = f(y(t), y(t-\Delta t), \dots, \mathbf{u}(t), \mathbf{u}(t-\Delta t), \dots), \tag{4.1}$$

where y is the endogenous variable, and $\mathbf{u}$ is a vector of exogenous variables. The lagged values are considered inputs into the forecasting model which has an output $y(t+T)$, where T is the forecasting horizon. In this work we will consider forecasting horizons of $T = 30$, 60, 90, and 120 minutes for a time-series $y(t)$ consisting of 30-minute averaged global horizontal irradiance (GHI).

A critical step in developing the forecasting model is a careful consideration of which data to include in the input vectors. Ideally, the inputs should be those which contain information relevant for the forecasting of future values of the time-series. In the case of solar irradiance, its future values are strongly dependent on the cloud conditions, therefore a good characterization of cloud conditions *and* cloud motions is paramount for the forecasting of solar irradiance. Thus, in this work we propose a methodology capable of producing good forecasting for solar irradiance based on satellite cloud images which comprises three stages. A schematic depicting an overview of the procedures involved in the model development is shown in Fig. 4.1. The first 2 stages involve cloud analysis procedures, including cloud indexing and cloud velocimetry. These two procedures can be done in parallel. In the stage identified by the upper-right boxes in Fig. 4.1, cloud indexed images are produced using images derived from the Visible spectrum. The stage identified by the upper-left boxes shows the velocimetry calculations using images obtained from the Infrared spectral channels. The output of this stage is a single velocity vector that represents the mean direction for the cloud propagation. In the last stage, identified by the lower boxes, the cloud indexed image and the velocity vector are used to define a set of grid elements and to compute cloud fractions. The cloud

fraction variables define the inputs that will be processed by the ANN forecasting model to produce solar irradiance forecasts. Each of the stages in the forecasting process are discussed in detail in the following sections.

4.3 Cloud indices

Cloud indexed images are produced by analyzing each pixel in the satellite images. The observed pixel intensity values of a raw visible image, E, are the result of the remote sensing of reflected visible sun light. Since clouds have a high reflectivity they appear whiter, due to the higher pixel values, than the land masses and oceans in a satellite image. Snow on the ground also has high albedo and can therefore be easily confused with clouds when using a pixel based algorithm for cloud detection. The cloud indexed image is obtained from E images following the approach described by [56] and repeated here because of the importance of this process in our methodology.

The first step in the cloud indexing is to examine the pixel values as a function of the solar zenith angle $\cos(\theta_s)$. As in [56], we apply the following relation between pixel intensity values $E(t)$ and $\cos(\theta_s)$,

$$E = I_0 \rho \cos(\theta_s)^{\alpha}, \tag{4.2}$$

where I_0 is the solar constant, ρ is the pixel albedo and α is a fitting parameter. Fig. 4.2 displays observed pixel intensity values versus $\cos(\theta_s)$ for a random location over several days indicated in the figure caption. The figure shows that the values of pixel intensity of the original image increase with $\cos(\theta_s)$ from values between 20 to 200. The diurnal variation of the solar irradiance is caused by $\cos(\theta_s)$ dependence of the solar irradiance, in order to remove the diurnal effects we use the following form of Eqn. (4.2),

$$\rho = \frac{E}{I_0 \cos(\theta_z)^{\alpha}}, \tag{4.3}$$

with parameter $\alpha = 1.4$. In addition to the E pixel values (blue markers), Fig. 4.2 shows values of $\rho \times I_0$ as a function of $\cos(\theta_s)$ (green markers). The plots shown that the diurnal effects are

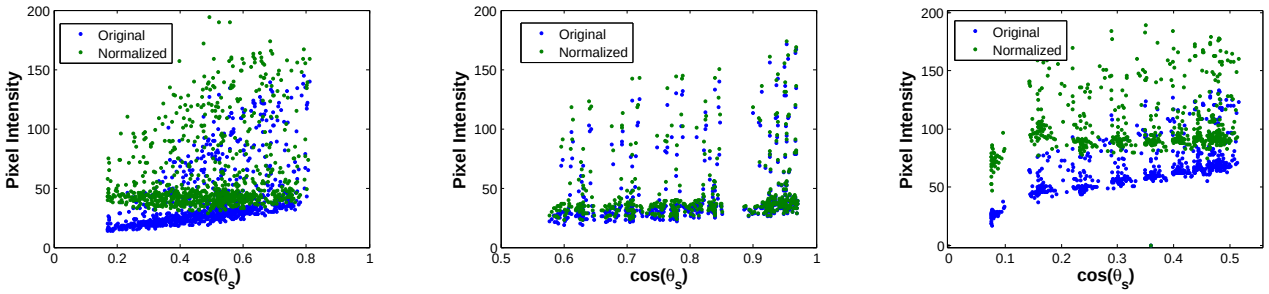

(a) Jan.–Feb., 2011 (b) May–Jun., 2011 (c) Nov.–Dec.. 2011

Figure 4.2 – Pixel intensity versus $\cos(\theta_s)$ before and after normalization. The flatter line resulting from the normalization indicates that the diurnal effects on intensity have been removed.

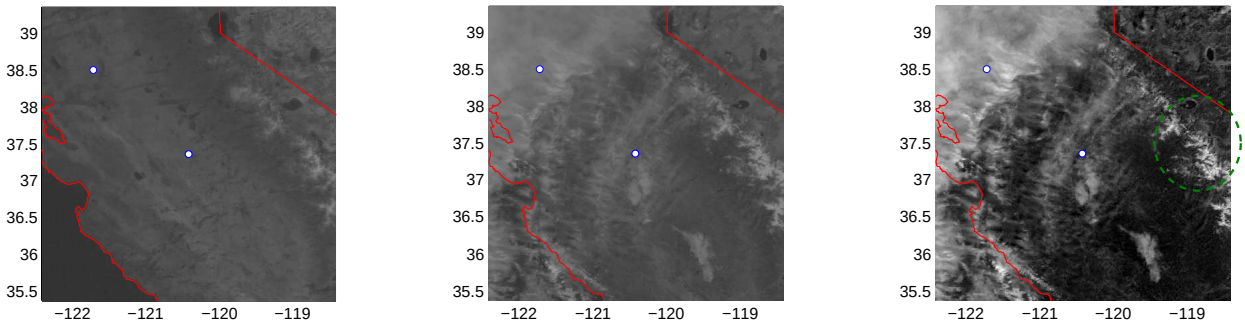

(a) Albedo image (b) Original image (c) Cloud indexed image

Figure 4.3 – Images for demonstrating the cloud indexing procedure. *Left* Albedo image obtained by taking the minimum pixel intensities for each pixel location. *Middle* Original image taken on 12/23/2011. *Right* Cloud indexed image after applying normalization.

successfully removed using $\alpha = 1.4$ for $\cos(\theta_s) > 0.15$, however, for cases where $\cos(\theta_s) < 0.15$ (close to sunrise and sunset) the diurnal effects were not removed in a satisfactory manner. As a result, in later sections, we only consider forecast analysis involving $\cos(\theta_s)$ values above 0.15.

After determining the normalized albedo image ρ, we can define a cloud index n as

$$n = \frac{\rho - \rho_{\max}}{\rho_{\max} - \rho_{\min}}, \tag{4.4}$$

where $\rho_{\max}$ and $\rho_{\min}$ are the maximum and minimum albedos determined over a set of images. In

this work, $\rho_{\min}$ is obtained by taking the minimum ρ for each pixel location over a week's worth of satellite image data. These values are then assembled in a reference ground albedo image as exemplified in Fig. 4.3. The parameter $\rho_{\max}$ is not treated the same way as it depends on cloud reflectivity, depth and type which cannot be characterized properly by a reference image. In this work, the value of $\rho_{\max}$ is set to $\rho_{\max} = 200$. This value was selected based on the data observed in Fig. 4.2, which shows that the pixel values do not exceed 200. In order to illustrate the cloud indexing procedure, Fig. 4.3 shows the reference ground albedo image, an unprocessed original image, and a cloud indexed image (using Eqn. 4.4) for the central valley of California and part of the Sierra Nevada mountain range. The image pixel value limits in Figs. 4.3(a) and 4.3(b) are set to 80 to 200 for enhanced visualization. We can see from this figure how this procedure enhances the contrast between clouds and the ground. In the East part of the images around the Sierra Nevada, snow is observed and is not canceled out properly because of the day-to-day snow accumulation during the time the images were taken, however this situation is not a concern for our purposes because there is no snow accumulation in the locations that where the forecast will be applied.

The cloud indexed image in Fig. 4.3(c) is the output of the cloud processing stage (see upper-right boxes in Fig. 4.1). In a following stage we compute the cloud index fractions on grid elements selected depending on the could motion. These variables will then be used in the ANN forecasting models.

4.4 Velocimetry with IR images

Velocity field calculations are performed using a Particle Image Velocimetry (PIV) algorithm obtained from [51]. This algorithm has been successfully applied to the estimation of cloud motion from sky images obtained with a Total Sky Imager to produce Direct Normal Irradiance (DNI) forecasts [57]. The PIV algorithm computes the velocity vectors by determining the correlation between a set of consecutive images. The images are partitioned in a grid of interrogation windows in which the algorithm operates obtaining a velocity vector for each one.

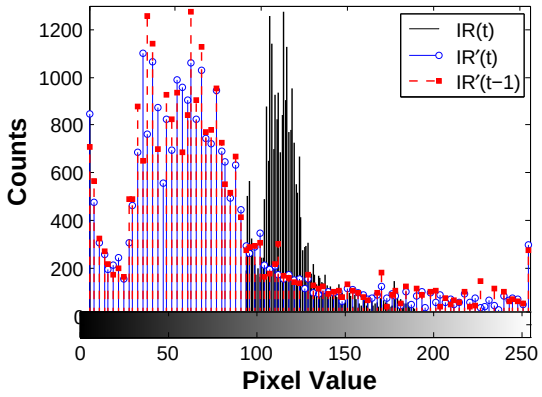

Figure 4.4 – Infrared image histograms adjusted so that the errors are not introduced into PIV routine. By applying histogram equalization, the diurnality of the pixel intensities are removed.

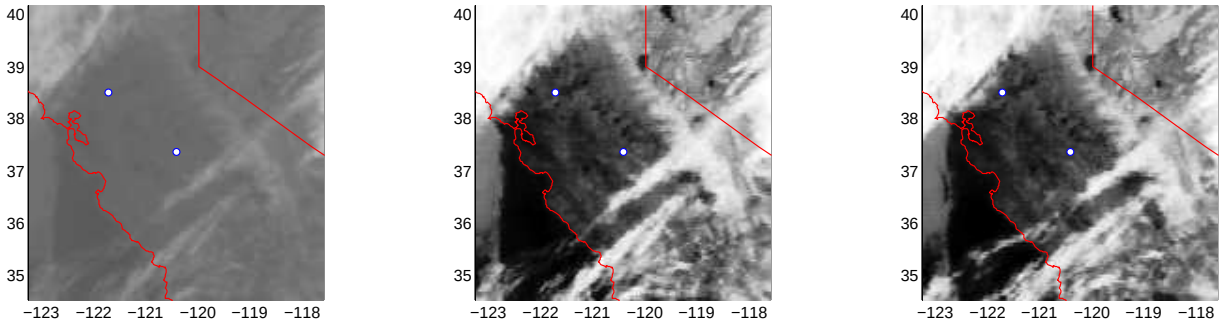

(a) Original IR (b) Old IR (c) New IR

Figure 4.5 – Pre-processing of consecutive IR images so that histogram of pixel intensities are equalized. This step helps to avoid potential errors in PIV algorithm.

A problem with using the images from the visible spectral bands (E) is that these images are only useful during the day. Moreover, they are difficult to process during the early and late parts of the day, as discussed in the previous section. To overcome this problem we proceed by using Infrared (IR) images since the IR images are available at all times and do not have the processing complications that would have affected the PIV calculations if the visible images were used.

Given that the PIV algorithm applies correlations to neighboring pixels of sequences of images if the pixel values change by factors other than the cloud motion the PIV algorithm will fail to

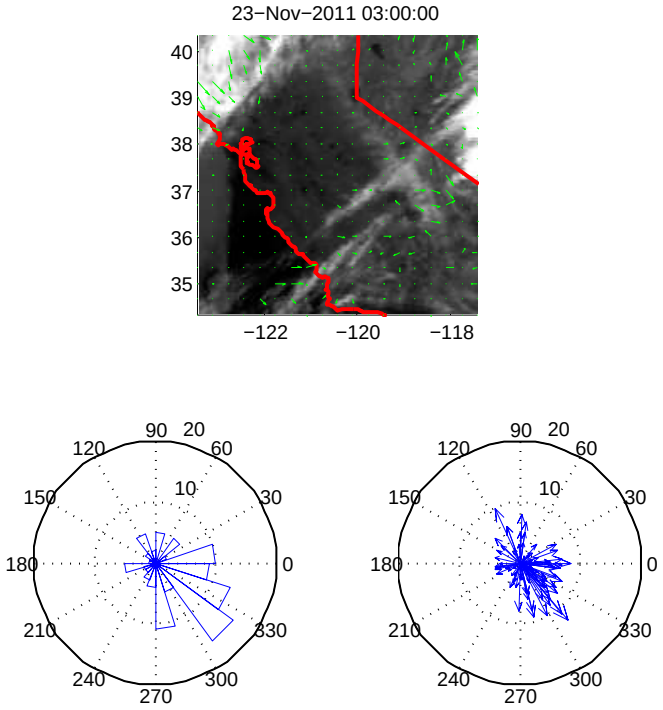

Figure 4.6 – Velocity field obtained from PIV algorithm. The rose plot on bottom left shows the histogram of the velocity vectors and the compass plot on the bottom right shows the distribution of the velocity vectors.

capture the cloud apparent velocity. One possible source of such errors is the diurnal variation of the pixel intensity [58]. Thus, in order to reduce potential errors using the PIV algorithm, each pair of IR images is first pre-processed by adjusting the intensity values of the second image ($IR(x,t)$) with the first one ($IR(x,t-1)$) using a histogram equalization algorithm. A histogram of an unprocessed image is shown in Fig. 4.4 (the black vertical bars). The distribution of pixel intensity for this example falls in the range 100 to 200 and is most dense at 120. Due to the narrow range, the original image appears mostly gray with little contrast between clouds and and the ground in Fig. 4.5(a). The image contrast is enhanced by adjusting the pixel value histograms so that the pixel values spread out between 0 and 255. An example of the pre-processing is shown in Fig. 4.5(b). In the processed IR image, clouds are easily distinguished from the ground. The image that was taken

30-minutes later is also processed so that the histogram of the pixel intensity values matches the processed pixel values of the current image, see Fig. 4.5(c). The processed consecutive IR images are used as inputs in the PIV algorithm to compute the velocity field vectors.

An example of the velocity field calculations is shown in the top plot of Fig. 4.6. The velocity field was obtained for images from the same days as the images in Fig. 4.5, from which we can see that the clouds are moving in the South-East direction. Although, there are a few 'stray' vectors, we can see from the histogram of the velocity directions (rose plot on bottom-left of Fig. 4.6) and distribution of velocity vectors (compass plot on bottom-right of Fig. 4.6) that most vectors point in the South-East direction, as expected. To obtain the final output of the velocimetry stage (see Fig. 4.1), we compute the average velocity vector ($\bar{\mathbf{V}}$) as,

$$\bar{\mathbf{V}} = \frac{1}{N}\sum_{i\in\mathfrak{I}} u_i \mathbf{e}_{lon} + \frac{1}{N}\sum_{i\in\mathfrak{I}} v_i \mathbf{e}_{lat}, \tag{4.5}$$

where u is the speed in the horizontal (longitudinal) direction), v is the speed in the vertical (latitudinal) direction, and the summation is carried out over the set of vectors in $\mathfrak{I} \equiv \{i : \sqrt{u_i^2 + v_i^2} \geq 1\}$ (vectors with magnitude greater than 1 pixel/30min), so that only that non-zero vectors are included in the averaging.

The final output of the velocimetry stage is $\bar{\mathbf{V}}(t)$ which is computed from IR images at time t and $t-1$. Because at sub-hourly to hourly time-scales we do not expect that the bulk cloud movement will change very much, a backwards moving average over the last three time-steps is applied to ensure the smoothness of time-series $\bar{\mathbf{V}}(t)$,

$$\bar{\mathbf{V}}'(t) = \frac{1}{3}\sum_{\tau=t-2}^{t} \bar{\mathbf{V}}(\tau). \tag{4.6}$$

where $\bar{\mathbf{V}}'(t)$ is the velocity that will actually be used for computing the set of Cloud Index variables that will be used as inputs to the ANN forecasting model.

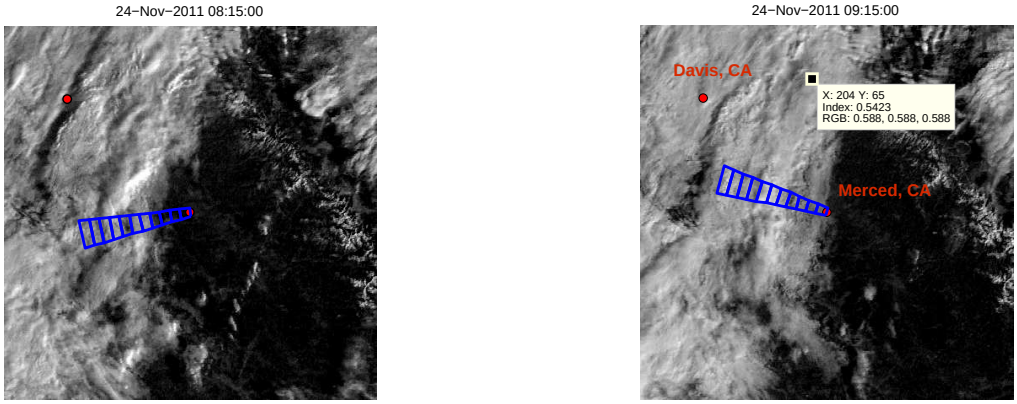

(a) (b)

Figure 4.7 – Sector used for computing cloud fraction variables $X_i(t)$. The sector orientation is collinear with the direction of the cloud movement. For this case, the sector originates from one of the location of interest (Merced, CA). Another sector (not displayed in figure) for Davis, CA is also used.

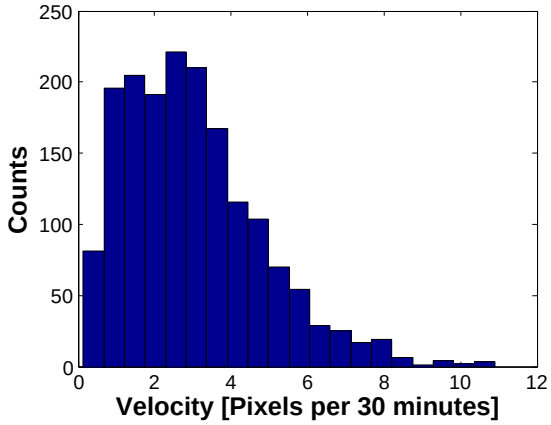

Figure 4.8 – Histogram of cloud speeds over the range of dates: Nov. 23, 2011 – Dec. 31, 2011. The velocity units are in pixels widths (of the IR images) per 30 minutes. The average cloud speed is 3 pixels/30 minutes, which translates to $\approx$ 20–24 km/hour. Converting to units for the Visible images, the average speed is $\approx$ 12 pixels/30 minutes.

4.5 Cloud Indexed Variables

As part of the first step in developing the forecast models, the input variables are established from the work done in the preprocessing stages. There are two pieces of information that are available

1) cloud-indexed images, and 2) cloud velocities. The cloud indexed variables (X) are computed by creating a set of grid elements that represent portions of the sky that are more likely to determine the short term future of the solar irradiation at the forecasting location. The grid elements are created with the first element originating at the location of interest, then extending out more elements in the upstream direction of the flow field $\bar{\mathbf{V}}'(t)$. This approach assumes that advection is the main transport mode for the clouds therefore it will likely perform well when frozen cloud translation is a good approximation.

Figure 4.7 shows an example of a sector of elements for a sequence of images separated 2 time-steps apart (1-hour). For each element the average cloud index is computed using the cloud indexed image ($n(x,t)$) obtained from the first stage (see Fig. 4.1). The calculation of X_i can be written as,

$$X_i(t) = \frac{1}{N} \sum_{x_j \in A_i} n(x_j, t), \tag{4.7}$$

where A_i represents the area bounded by the i^{th} grid element (see Fig. 4.7). The size of the elements is adaptive and determined by analyzing the cloud speeds: higher speeds correspond to longer grid elements. A distribution of the cloud speeds is shown in Fig. 4.8 where the units are given in pixels widths (of the IR images) per 30 minutes. The average cloud speed is 3 pixels/30 minutes, which translates to $\approx$ 20-24 km/hour (resolution of IR images are $\approx$ 4 km/pixel). Converting to units for the visible (E) images, which have a resolution of $\approx$ 1 km/pixel, the average speed is $\approx$ 12 pixels/30 minutes. The element widths are adjusted to become wider for larger distances form the point of interest in order to have some robustness in all the uncertainty involved.

The cloud index variables just described and referred to as $X_1, X_2, \ldots, X_7$ are then used as exogenous inputs into the forecasting model. The subscripts denote the grid element for which the cloud index average was computed with 1 being the closest grid element and 7 being the furthest. The approach described here resembles that in [57], except that there DNI forecasting was obtained with a simple curve fitting between the cloud index averages and the irradiance, whereas here the cloud index averages are incorporated into a non-linear ANN forecasting model.

4.6 Artificial Neural Networks

As mentioned in Section 4.2 and depicted in the Forecasting Algorithm diagram in Fig. 4.1, the forecasts are ultimately produced by an ANN time-series forecasting model. Artificial Neural Networks (ANNs) are useful tools for approximating complicated mapping functions for problems in classification and regression [59], and have also been used extensively in many areas including solar radiation modeling. A review of over 40 applications of ANNs and other artificial intelligence techniques applied to solar radiation modeling can be found in [16]. The advantage of ANNs is that no assumptions are required about the underlying process relating input and output variables. An ANN is a particular representation of an output y in terms of some input variables x. The ANN representation is based on signals being sent through elements called neurons in such a way that the processing of the inputs signals produces an output, y, that is sufficiently close to the desired target value of t. Neurons are arranged in layers, where the first layer contains the set of inputs, the last layer contains the output, and the layers in between, referred to as hidden layers, contain hidden neurons. A feedforward neural network with N inputs and N_h neurons in one hidden layer with a linear output activation function can be expressed as,

$$y = \sum_{k=1}^{N_h} w_k f_k^{hidden} \left(\sum_{j=1}^{N} w_{j,k} x_j + w_{0,k} \right) + w_0, \tag{4.8}$$

where f_k^{hidden} are sigmoidal functions, such as the hyperbolic tangent function. A characteristic of feedforward neural networks is that the neurons are successively interconnected from layer to layer where neurons in one layer affect all neurons in the next but do not affect other neurons in the same layer or any preceding layers. Numerical optimization algorithms such as back-propagation, conjugate gradients, quasi-Newton, and Levenberg-Marquardt have been developed to efficiently adjust the weights, $w_{k,j}$ and w_k in the feedforward neural networks so that the minimization of some performance function is achieved on some training data. Typically the performance function

Table 4.1 – Name referencing of considered models and their mathematical descriptions. Models GHI_{f1} and GHI_{f2} differ by their respective exclusion and inclusion of the GHI(t) time-series as inputs. The Cloud Motion Forecast (CMF) model refers to the study in [1], where $k_f^*(t+T)$ is obtained by forecasting the cloud motion.

Model	Mathematical Description
GHI_{f1}	$= f(\cos(\theta(\tau))\|_{\tau=t+T,\ldots,t-n\ \Delta t}, X_i(\tau)\|_{\tau=t,\ldots,t-n\ \Delta t})$
GHI_{f2}	$= f(\cos(\theta(\tau))\|_{\tau=t+T,\ldots,t-n\ \Delta t}, X_i(\tau)\|_{\tau=t,\ldots,t-n\ \Delta t},$ $\text{GHI}(\tau)\|_{\tau=t,\ldots,t-n\ \Delta t})$
GHI_p	$= k^*(t)\ \text{GHI}_{clear}(t+T)$
CMF	$= k_f^*(t+T)\text{GHI}_{clear}(t+T)$

used for adapting the weights is the MSE.

$$\text{MSE} = \frac{1}{M}\sum_{i=1}^{M}(y_i - t_i)^2. \tag{4.9}$$

4.6.1 ANN forecast development and training

Here we use ANNs to produce the function to model the time-series function expressed in Eqn. 4.1, which includes the input variables: $y(t), y(t-1), \cos(\theta_z(t+T)), \cos(\theta_z(t+T-1)), X_1(t), X_2(t), \ldots, X_7(t)$, and $X_1(t-1), X_2(t-1), \ldots, X_7(t-1)$; to predict $y(t+T)$, where y are 30-minute averaged values of GHI, $\cos(\theta_z)$ is also expressed in 30-minute averages, and the variables X_i's are as defined in Section 4.5. The models which are considered for this study are summarized in Tab. 4.1. The inputs include the use of lagged information which is usually useful in forecasting models. The lagged information includes the previous $n = 2$ time-steps for the variables involved. Using more lagged values leads to unnecessary inputs and over-complicates ANN training. It is also important to included $\cos(\theta_z)$ as an input to the ANN, since this variable is useful for describing the deterministic diurnal variation of GHI. The variables X, if useful, will help to describe the cloud effects on GHI.

For this work we consider two ANN models with the main difference being in the input layer. One of the models which does not include lagged values of GHI as an input variable, will be referred to as GHI_{f1}. The other model will have lagged GHI values as inputs and will be referred to as GHI_{f2}. Otherwise, the ANN architectures for both models are configured to have $N_h = 5$ hidden neurons

and are trained by minimizing the MSE over a random training set consisting of 90% of the data. The remaining data set is used as a testing set in order to avoid ANN over-training by terminating the training once the MSE over the testing set has increased after 6 consecutive iterations. The data set is comprised of data gathered from Nov. 23, 2011 through Jan. 5, 2012 from the UC Merced and UC Davis solar observatory stations located at 37.36 N, 120.43 W and 38.5 N, 121.73 W, respectively. Data for the month of May 2011 for Merced, CA is used as a hold-out validation set, which is not used at all in the training process.

4.6.2 Persistent Model For Baseline Forecast Comparison

In this section we explain the persistent model that will be used as the baseline for comparing the accuracy of the forecasting methodology here proposed. The persistent model is defined by using the current clear-sky index as a prediction for the future clear-sky index. The clear-sky index is defined by normalizing GHI with a clear-sky model, GHI_{clear},

$$k^* = \frac{\mathrm{GHI}}{\mathrm{GHI}_{clear}}. \tag{4.10}$$

Assuming that the current k^* persists into the future, the forecasted GHI is:

$$\mathrm{GHI}_p(t+T) = k^*(t)\ \mathrm{GHI}_{clear}(t+T). \tag{4.11}$$

It is worth noting that the persistence model is highly accurate for many parts of year when there are cloudless days or even for highly overcast days. Because the persistent model incurs into large errors only during highly variable days, the persistence errors directly help to describe the intrinsic random variability in solar irradiance (see [32] for more on solar variability, and [2] for further discussion on bench-marking forecast quality with persistence). Because of this property, the persistence model is the best way to compare models developed and tested over different data sets [2].

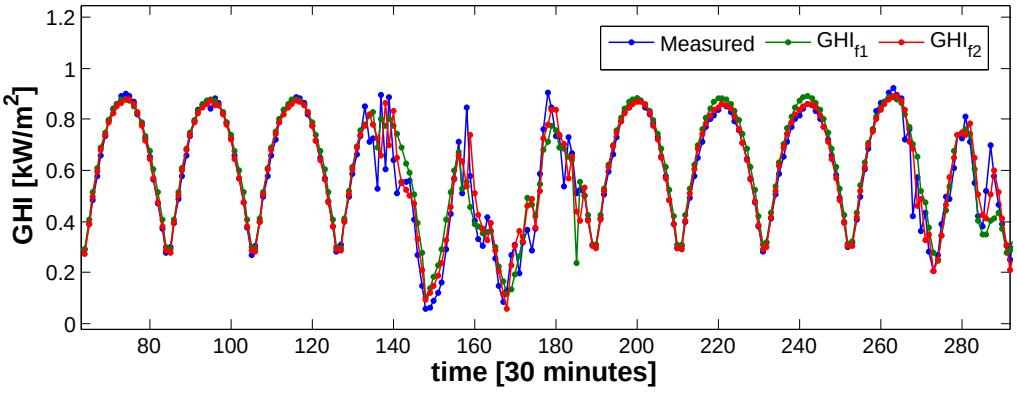

Figure 4.9 – Time series of measured and forecasted GHI for $T = 30$ minutes ahead. Data shown includes the days from May 5–15, 2011 for Merced, CA which was part of the validation set with night values removed.

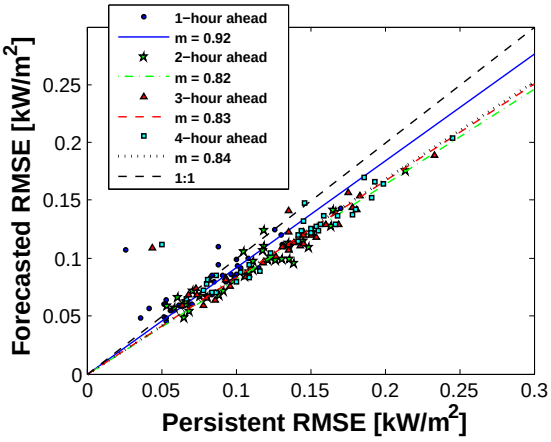

Figure 4.10 – RMSE of forecast and persistence models for forecasting horizons 1–4 hours ahead. Data obtained from [3]. The slopes m are used to estimate the relative improvements of the forecasts over the persistence: 1 - RMSE$_f$/RMSE$_p = 1 - m$.

Table 4.2 – Forecast MBE, RMSE, and RMSE forecast skill: 1 - RMSE/RMSEp, where RMSEp is the RMSE of the persistence model. See Tab. 4.1 for model descriptions. Values denoted in bold represent best performance. RMSE forecast skill performance is estimated from Fig. 9 of [1].

(a) $T = \Delta t = 30$ minutes

	MBE $[W/m^2]$	RMSE $[W/m^2]$	1 - RMSE/RMSE$_p$ [%]
Training			
GHI$_{f1}$	**0.422**	59.3	8.53
GHI$_{f2}$	-1.49	**53.1**	**18.1**
GHI$_p$	-2.84	64.8	0
Validation			
GHI$_{f1}$	74.9	10.7	11.6
GHI$_{f2}$	**71.1**	**2.13**	**16.1**
GHI$_p$	84.7	3.34	0
CMF	–	–	8

(b) $T = 2\ \Delta t = 60$ minutes

	MBE $[W/m^2]$	RMSE $[W/m^2]$	1 - RMSE/RMSE$_p$ [%]
Training			
GHI$_{f1}$	-1.99	68.1	18.4
GHI$_{f2}$	**-1.67**	**65.4**	**21.6**
GHI$_p$	-6.9	83.4	0
Validation			
GHI$_{f1}$	**4.64**	83.4	14.3
GHI$_{f2}$	4.89	**79.7**	18.2
GHI$_p$	5.7	97.4	0
CMF	–	–	18

(c) $T = 3\ \Delta t = 90$ minutes

	MBE $[W/m^2]$	RMSE $[W/m^2]$	1 - RMSE/RMSE$_p$ [%]
Training			
GHI$_{f1}$	-4.9	78.5	20.1
GHI$_{f2}$	**-2.68**	**75.1**	**23.6**
GHI$_p$	-15.4	98.3	0
Validation			
GHI$_{f1}$	**2.74**	84.3	22.5
GHI$_{f2}$	9.25	**84**	**22.8**
GHI$_p$	5.74	109	0
CMF			17

(d) $T = 4\ \Delta t = 120$ minutes

	MBE $[W/m^2]$	RMSE $[W/m^2]$	1 - RMSE/RMSE$_p$ [%]
Training			
GHI$_{f1}$	-8.6	90.2	18.5
GHI$_{f2}$	**-3.52**	**82.6**	**25.4**
GHI$_p$	-24.6	111	0
Validation			
GHI$_{f1}$	-10.4	89.5	24.2
GHI$_{f2}$	-5.48	**83**	**29.7**
GHI$_p$	**4.71**	118	0
CMF	–	–	16

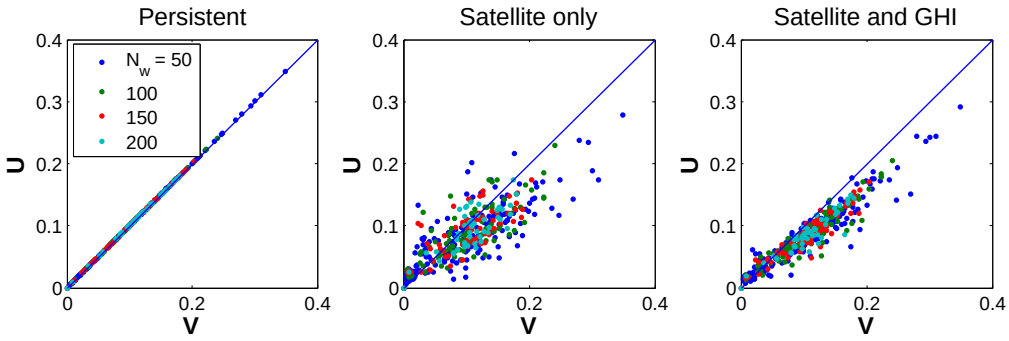

(a) 30 minute ahead forecast on entire data set

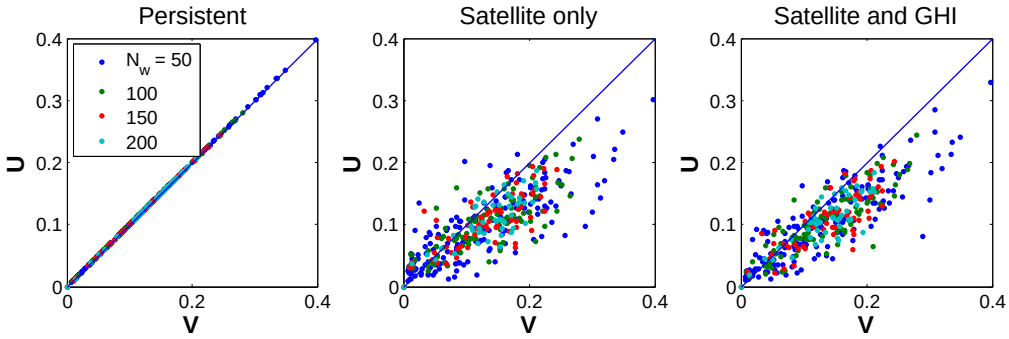

(b) 60 minute ahead forecast on entire data set

Figure 4.11 – Scatter plot of U and V for persistence forecasts, satellite-based ANN forecasts, and a combined forecast for 30 and 60 minutes ahead on validation data subset and entire data set. The combined forecasts is the average of the persistent and the satellite-based ANN forecasts.

4.7 Forecasting Results

The accuracy of the forecasting models is evaluated using four evaluation criterions: the Mean Biased Error (MBE), the Root Mean Square Error (RMSE), the RMSE forecast skill, and the forecasting skill metric s recently proposed by [2]. The accuracy metrics are evaluated independently for the two existent data sets – training and validation. Where possible, we also include comparisons with existing satellite-based solar forecasts such as in [1, 8]. As a visualization of the actual forecasts, Fig. 4.9 is provided, showing the measured GHI and the forecast models GHI_{f1} and GHI_{f2} (see Tab. 4.1 for descriptions).

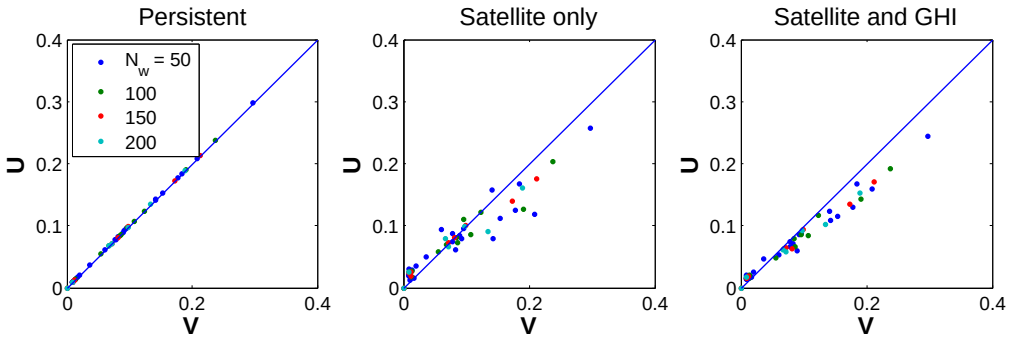

(a) 30 minute ahead forecast on validation data set

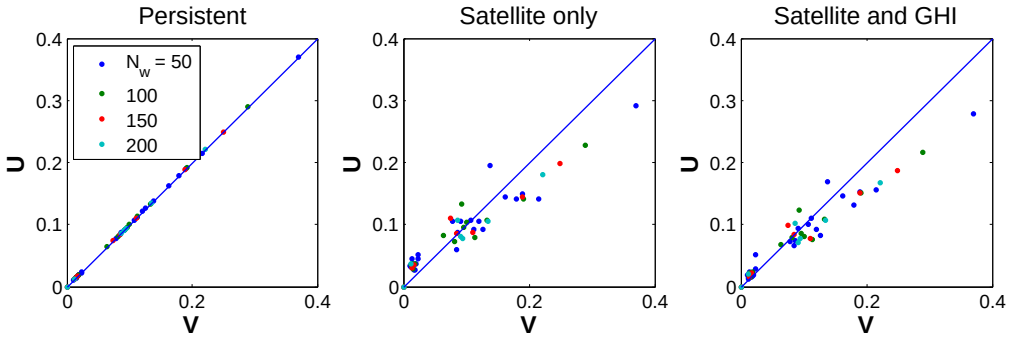

(b) 60 minute ahead forecast on validation data set

Figure 4.12 – Scatter plot of U and V for persistence forecasts, satellite-based ANN forecasts, and a combined forecast for 30 and 60 minutes ahead on validation data subset and entire data set. The combined forecasts is the average of the persistent and the satellite-based ANN forecasts.

4.7.1 MBE and RMSE Evaluations

The models described in the previous section are evaluated and compared here in terms of MBE and RMSE,

$$\text{MBE} = \frac{1}{N} \sum_{t \in DT} (\text{GHI}_f(t) - \text{GHI}(t)), \tag{4.12}$$

and

$$\text{RMSE} = \sqrt{\frac{1}{N} \sum_{t \in DT} (\text{GHI}_f(t) - \text{GHI}(t))^2}, \tag{4.13}$$

where $\text{GHI}(t)$ is the measured value at time t, $\text{GHI}_f(t)$ is the forecasted value at time t, and the summation is carried over $t \in DT$ day-time values only. The day-time sets satisfy the criteria, $\cos(\theta_z) > 0.15$ which also excludes the early and late parts of the day. These parts of the days

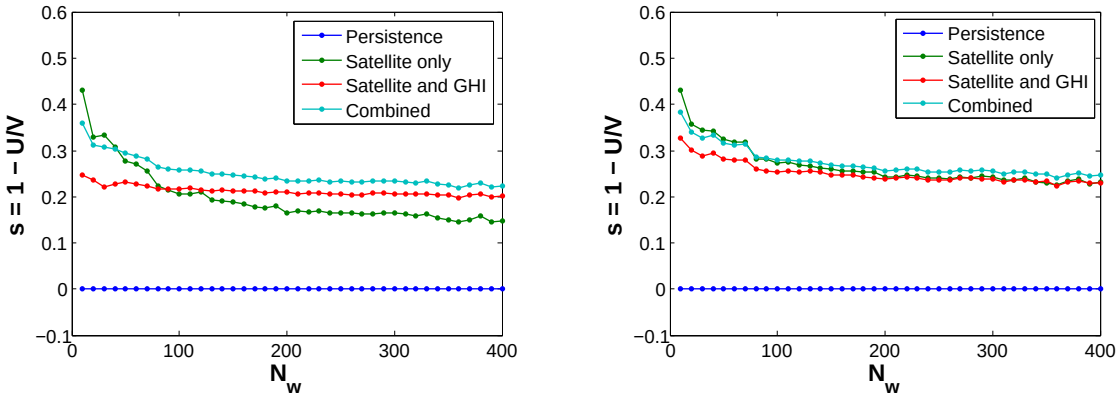

(a) 30 minute ahead forecast

(b) 60 minute ahead forecast

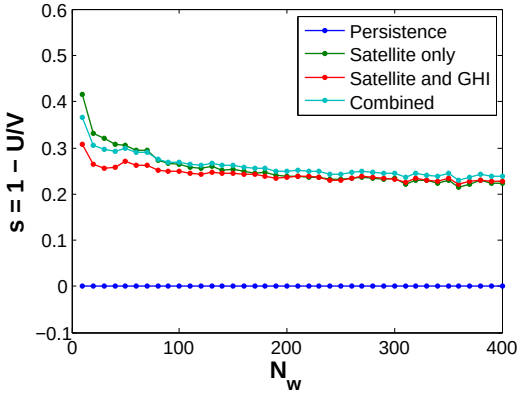

(c) 90 minute ahead forecast

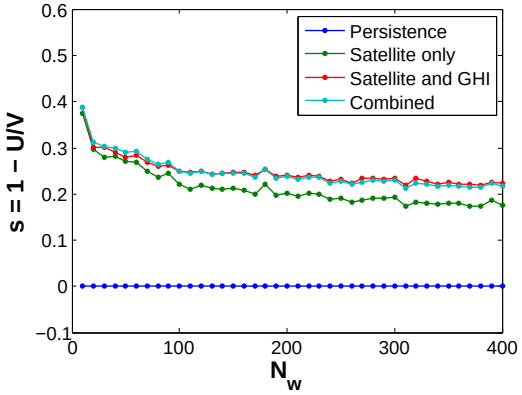

(d) 120 minute ahead forecast

Figure 4.13 – Calculations of $s = 1 - U/V$ for 30 – 120 minute forecast horizons over entire data set. The combined forecast is the average of the persistent and the satellite-based ANN forecasts.

would also cause excessive difficulties in the image processing as discussed in Section 4.3.

Table 4.2 displays the RMSEs and MBEs of the mean GHI calculated for the entire data set. The evaluations are performed for the forecasting horizons of $T = 30, 60, 90$, and 120 minutes for the 30-minute averaged GHI values for the training and validation sets. The best RMSEs are generally obtained with the model GHI_{f2} for all forecasting horizons. The ranking in terms of the MBEs, however, is more diverse. As a measure of the forecasting skill, we consider the relative RMSE improvement over the persistence (also shown in Tab. 4.2). The relative improvements range between 8–29.7% for the proposed forecasting methods. The RMSE forecast skill with respect to

the persistent model is considerably better as T increases.

The RMSEs also lie in the range obtained in the satellite-based solar irradiance forecasts for a single location by other researches [15, 25, 1]. In order to compare the forecast performance of [1], we have estimated the RMSE forecast skill values from Fig. 9 of [1], which are shown in Tab. 4.2 here. From these observations, it appears that the proposed methodology compares favorably with existing satellite-based forecasting models.

The presented forecasted methodology can also be compared with the results obtained in [3] by again comparing the relative improvements of RMSEs over the persistent model. RMSE data obtained from [3] is plotted in Fig. 4.10. The plots show the RMSEs of cloud motion-based hourly GHI forecasts and persistent RMSEs for forecasting horizons of 1-6 hours. There are two similarities to point out between the results in [3] and the results obtained here: the first observation is that the smallest relative improvements are obtained for the first forecasting horizon, as can be seen by estimating the relative improvements as given by the slopes ($1 - \mathrm{RMSE}_f/\mathrm{RMSE}_p = 1 - m$). For the 30-minutes ahead forecasting of the 30-minute average GHI, we obtain an improvement of $\approx 8.5-18.1\%$, whereas [3], reports an improvement of $\approx 10\%$. These forecasting horizons correspond to 1 time-step (Δt) forecasting horizons for the respective studies. The second observation is that, for multiple time-step ($T = n\ \Delta t$) forecasting horizons, the relative improvements are consistently $\approx 20\%$.

4.7.2 Forecast Skill Evaluation

To further evaluate the forecast model performance, the forecast skills of the developed models are evaluated using the procedure described in [2]. The procedure involves calculating the uncertainty U, defined as,

$$U = \sqrt{\frac{1}{N_w} \sum_{t \in T_w} \left(\frac{\mathrm{GHI}_f(t) - \mathrm{GHI}(t)}{\mathrm{GHI}_{clear}} \right)^2}, \tag{4.14}$$

and the variability V, defined as,

$$V = \sqrt{\frac{1}{N_w} \sum_{t \in T_w} \left(k^*(t) - k^*(t - \Delta t)\right)^2}, \tag{4.15}$$

over subsets $T_w = T_1, T_2, \ldots, T_{(N/N_w)}$, of size N_w data points, then calculating the average forecasting skill as $\langle s \rangle = 1 - \langle U/V \rangle$, where the average of the ratio U/V can be determined from regression over each pair (U_i, V_i) calculated in subset T_i. In the definition for V, the clear-sky index $k^* = \text{GHI}/\text{GHI}_{clear}$ is used. As discussed in [2], this forecasting metric is approximately equivalent to simply take the ratios of the RMSE of the forecasts with the RMSE of a persistent model ($U/V \approx$ RMSE/RMSEp, where RMSEp is the RMSE of the persistent model).

Figure 4.11 shows scatter plots of U and V computed after partitioning all of the training data with $N_w = 50, 100, 150$, and 200 points. These plots allow us to visualize the forecasting performance: when points lie below the 1:1 line, the forecast model is considered to have forecasting skill whereas when points are above the 1:1 line it indicate that the forecasts are worse than the persistent model and correspond to negative forecasting skill values ($s < 0$).

The plots for the persistent model serve to verify the evaluation procedure: as expected for forecasting horizons of 30 and 60 minutes, all the (U, V) points for the persistent model lie on the identity line as shown in Fig. 4.11 , therefore, the persistent model does not indicate forecast skill according to definition. The performance of the developed satellite-based forecasts show some improvement over persistence, as many of the points fall below the 1:1 line. For the "satellite only" forecast model, the one which uses no GHI lagged values (GHI_{f1}), the forecasting skill seems to indicate that this model can be a very superior model at times since many (U, V) points far below the identity line it seems to be. However, model GHI_{f1}, is a riskier model as it also frequently encounters (U, V) above the 1:1 line. With respect to the forecasting model that does include GHI as an input variable (GHI_{f2}), we see that it is a more consistent model, as the overall scatter of the (U, V) points are tighter than for GHI_{f1}, particularly for the 30 minute (1-step) forecast horizon.

From the forecast skill analysis of GHI_{f2}, we can also observe that the effect of including GHI as

an input begins to decrease with longer forecasting time horizons, and that both GHI_{f1} and GHI_{f2} models begin to perform with similar accuracy (e. g., compare the upper-right and lower-right plots in Fig. 4.11). Therefore, at longer forecast time horizons ($T \approx 90$–120 minutes), the accuracy levels seem to depend more on the satellite derived information rather than on the solar irradiance.

Figure 4.12 also shows (U, V) but for the validation set of May 2011 for Merced, CA (note the fewer points). Again, the general results are the same as for the training set which confirms that overtraining was avoided and that the forecast evaluation procedure is robust. From this comparison we can say that the forecasting model GHI_{f1} is a riskier model since the scatter plots are rather spread out as compared to the forecasts model GHI_{f2}.

The overall forecasting performances are summarized by computing the average forecasting skill $\langle s \rangle$. This is done by computing the slope of the linear regression with intercept set to 0 for points such as those in Fig. 4.11 and for various N_w. The results are shown in Fig. 4.13 for forecasting horizons of $T = 30, 60, 90$, and 120 minutes, which correspond to $n = 1, 2, 3$, and 4 time-step forecasts, respectively. In addition to the forecast models already mentioned (persistent, GHI_{f1}, and GHI_{f2}), a fourth model can be easily obtained by combining the latter two forecasts using a uniform average. For each forecasting horizon the baseline persistent model has a forecasting skill of $\langle s \rangle = 0$, while the proposed models each have significant forecast skill of $15\% \leq \langle s \rangle \leq 25\%$. Furthermore, for all forecasting horizons, the combined forecast shows some improvement over the two individual models.

4.8 Conclusions

This paper presents a global horizontal solar irradiance forecasting approach based on satellite observations and Artificial Neural Networks (ANNs). The satellite images were processed using cloud indexing and velocimetry algorithms so that Cloud Indexed average variables can be used as inputs to the ANN model. The forecasting horizons include 30, 60, 90, and 120 minutes to forecast the 30-minute averaged GHI. The resulting forecast root-means-squared errors (RMSE) and relative

improvements over the persistent model indicates that the produced forecasts are very similar to those obtained in other studies [15, 25, 3]. The improvements over persistence, in particular, seems to be a very reliable way of comparing forecast models. The improvements are $\approx 8.5 - 18.1\%$ for 1 time-step forecasts, and $\approx 18 - 30\%$ for multiple time-step forecasts. Until larger penetration levels of solar power come to the grid, and feedback is given to solar power forecasters, it remains to be determined whether these forecast qualities are adequate for increased renewables integration.

A novelty of this study is that it describes a hybrid model that combines detailed satellite-image processing with Artificial Neural Networks. Although these models are at least at par with conventional frozen cloud translation approaches, we anticipate that more sophisticated approaches that use machine learning techniques will follow and eventually lead to greater accuracy and reliable solar irradiance forecasting. For example, classification techniques can be used to identify fog, cloud-type, cloud texture, etc. and include these classes as part of the ANN forecasting algorithms. The first approach developed here has demonstrated that there is promise in this general direction.

Chapter 5

Forecasting of Global Horizontal Irradiance Using Sky Cover Indices

This work discusses the relevance of three Sky Cover (SC) indices for solar radiation modeling and forecasting. The three indices are global in the sense that they integrate relevant information from the whole sky and thus encode cloud cover information. However, the three indices also emphasize different specific meteorological processes and sky radiosity components. The three indices are derived from the observed cloud cover via Total Sky Imager (TSI), via measurements of the Infrared Radiation (IR), and via pyranometer measurements of Global Horizontal Irradiance (GHI). We enhance the correlations between these three indices by choosing optimal expressions that are benchmarked against the GHI SC index. The similarity of the three indices allows for a good qualitative approximation of the GHI irradiance when using any of the other two indices. An Artificial Neural Network (ANN) algorithm is employed to improve the quantitative modeling of the GHI sky cover index, thus improving significantly the forecasting details of GHI when all three indices are used.

5.1 Introduction

Our goal is to correlate Total Sky Imager (TSI) cloud cover measurements, Infrared Radiation (IR), and Solar Radiation (SR) at the Earth's surface and to use this information as input for modeling and forecasting of the Solar Radiation (SR). In order to develop the various correlations, we gather TSI and IR measurements and correlate both measurements with SR data. We note that each of these measurements are affected by the amount of the cloud cover present. There are inherited limitations to developing such correlations since they depict different information about the underlining atmospheric processes. For example, sky cover values obtained from the TSI are typically based on the proportion of pixel values above some threshold in the visible range. The IR measurements are sensitive to many factors, including surrounding temperature, sky temperature, relative humidity, atmospheric composition, and the presence of nearby clouds. Out of all these factors, cloud presence contribute the most to the variations in IR and our objective is to isolate these effects. The variability of SR is also strongly dependent on clouds.

Our approach correlates cloud effects on TSI and IR with the cloud effects on GHI. We then produce estimates of GHI based on TSI and IR. Section 5.2 presents the data sets used and explains the methodology of our analysis. In Section 5.3 we study three Sky Cover (SC) indices based on IR, TSI, and GHI measurements. Section 5.4 shows the results of the GHI estimates based on the IR and TSI indices. Section 5.5 demonstrates the importance of the IR and TSI information for the improvement of GHI forecasts based on Artificial Neural Network (ANN) algorithms. Concluding remarks are given in Section .

5.2 Data Collection And Methodology

The data used in this work corresponds to the period between October 3, 2010 and December 3, 2010 at the University of California Merced Solar Observatory. This period is characterized by a mixture of clear and overcast days. All instruments are located within 4m radius of each other

and are strategically placed so that shading and interference effects are minimized. Additional meteorological data sets, such as dewpoint temperature and soil temperature, are taken from the California Irrigation Management and Information Systems (CIMIS) at the Merced weather station (#148), which is located within 7 km of the UC Merced solar irradiance observatory station.

5.2.1 Global Horizontal Irradiance

We consider the effects of cloud cover on Global Horizontal Irradiance (GHI). An Eppley PSP (Precision Spectral Pyranometer) measures irradiance at wavelenghts between 0.285μm and 2.80μm, which comprises approximately 98.5% the solar spectrum. The amount of GHI has a diurnal dependence on the solar zenith angle. In order to remove this dependence, to isolate the cloud effects on GHI, and to compare to sky cover indices based on the TSI and IR measured values, we consider the clearness index K_g:

$$K_g = GHI/GHI_{clear}. \tag{5.1}$$

We estimate GHI_{clear} as a function of the cosine of the zenith angle ($\cos(\theta_z)$) only. We use the following clear days from the data set to benchmark our estimate of GHI_{clear}: October 10–15, and 20, and November 1, 15, and 24. October 10 is selected as the calibration set to produce a polynomial (cubic) fit as the estimate of GHI_{clear}, and the rest of the clear days are used to validate the fit. The order of the polynomial is determined by the rate at which the residual norm is changing - beyond the 3rd order the change is very small as compared to the change from quadratic to cubic order. The coefficients in order of the highest order term to the lowest order term (the constant) of the polynomial are calculated as -0.66, 1.2, 0.44, -0.0065. On the calibration set, the fit produces and mean bias error (MBE) of -1.3 W/m^2 and root mean squared error (RMSE) of 4.9 W/m^2. On the validation set, the fit produces MBE and RMSE values of -9.1 W/m^2 and 9.9 W/m^2. These errors are very small when compared to the variations on GHI resulting from cloud effects, so we do not expect our GHI_{clear} estimates to contribute to systematic errors on the subsequent correlations.

From the above equation, $K_g = 1$ for clear days and a very small value for cloudy days depending on total cloud cover. Sky cover variability based on GHI can be defined as:

$$SC_{GHI} = 1 - GHI/GHI_{clear} = 1 - K_g. \tag{5.2}$$

These sky cover estimates are compared in the next sections. In terms of solar modeling and forecasting, the most important sky cover quantity is the one based on the clearness index (K_g). Therefore, the TSI- and IR - based cloud cover quantities are benchmarked according to the clearness index values.

5.2.2 Infrared Measurements

The instruments used for measuring radiation are oriented on horizontal surfaces. The solar irradiance was measured with a pyranometer (PSP), and the infrared radiation was measured with a pyrgeometer (PIR), both of which were manufactured by Eppley Labs [60, 61]. In the PIR the case and dome temperatures are recorded along with net infrared radiation (IR_{net}). The infrared radiation IR is calculated according to [62]:

$$IR = IR_{net} + \sigma T_c^4 - k\sigma(T_d^4 - T_c^4), \tag{5.3}$$

where T_d is the instrument dome temperature, T_c is the instrument case temperature, k is constant with value $k = 3.5$ as recommended by the manufacturer, and σ is the Stephan-Boltzmann constant. The detector which measures IR_{net} is sensitive to radiation at wavelengths between 3.5μm to 50μm. In this range of wavelengths, radiation is mostly emitted from objects with temperature close to 300K and virtually no radiation from the Sun is received at these wavelengths. The intensity of the infrared radiation from the Sun is about two orders of magnitude smaller than the intensity in the visible spectrum. It is also about an order of magnitude smaller than the intensity of the IR radiation emitted by the Earth. In this respect, the clear-sky values of IR are approximated by

the Stephan-Boltzmann relationship with emittance ϵ that depends on the dewpoint temperature ($T_{dewpoint}$) and time of day [63]:

$$IR_{clear} = \epsilon \sigma T_{ambient}^4, \tag{5.4}$$

$$\epsilon = 0.6921 + 0.00244 T_{dewpoint} + 0.05101 \sin(15t), \tag{5.5}$$

where t is the number of hours from midnight and the ambient temperature is used in place of the sky temperature. The time variable (t) helps to remove the ambient temperature diurnal patterns introduced by estimating IR_{clear} from $T_{ambient}$. A more reasonable way to remove the diurnal patterns is to model ϵ as a function of relative humidity. Because the above equations give satisfactory estimates of IR_{clear}, we defer the aforementioned corrections.

5.2.3 Total Sky Imager Data

Images of the sky are taken by the Yankee Environmental Systems, Inc. TSI instrument [48]. The images are processed with the manufacturer's software that classifies pixel values for images taken with a camera located above a rotating hemispherical mirror. The mirror contains a band that continuously blocks the mirror from the sun (see Fig. 5.1). The processed sky cover information from the TSI includes fractional sky cover due to thin and opaque clouds, which are distinguished by the light blue and white shaded areas in Fig. 5.1. The proportion of these areas to the total circular area is classified as fractional sky cover. Images are taken and processed at one minute intervals from which hourly values are subsequently calculated.

The TSI does not produce other cloud properties such as cloud type, speed, or height. The information in the above list is given as a time-series which only includes day-time values since the sky-imager does not process images in the dark. As shown in Fig. 5.1, the built-in classification algorithms do not always classify all the clouds preset. Developing more accurate classifications is essential for a more precise use of the TSI. However, we do not address this issue here. Values calculated with the YES built-in algorithms are used in this paper.

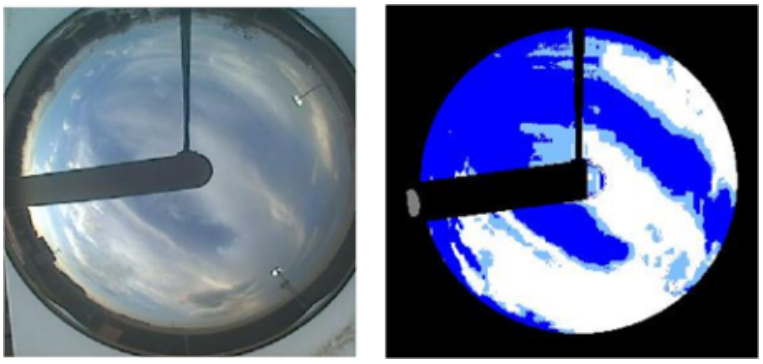

Figure 5.1 – Left: Example of image taken by the TSI for a cloudy day. Right: Processed image using manufacturer's image classification algorithms. Light blue color indicates thin clouds and white color indicates opaque clouds.

Table 5.1 – Expressions defining sky cover (SC) indices derived from GHI, TSI and IR data. The subscript 'clear' indicates data values associated with clear sky days.

Data Type	Sky Cover Index
Visible Radiation	$SC_{GHI} = 1 - GHI/GHI_{clear}$
Total Sky Imager	$SC_{TSI} = aSC_{thin} + bSC_{opaque} + c$
Infrared Radiation	$SC_{IR} = c_2\delta_{IR}^2 + c_1\delta_{IR} + c_0$,
	$\delta_{IR} = IR - IR_{clear}$

5.3 Correlating Sky Cover Indices

Cloud cover information is based on TSI, IR, and GHI measured values. The relations given in Table 5.1 show how sky cover (SC) is computed using data from each of the instruments. Note that the SC quantities based on the TSI and IR contain parameters that are used for fitting the data on SC that is based on GHI. This is because in this study we are specifically interested in extracting predictive information to forecast GHI. For the case of the TSI, we assume that a linear combination of the thin and opaque sky cover correlates well with the SC_{GHI}. This approach is more general than simply adding thin and opaque values because the coefficients may help to correct some of the errors introduced during image processing of the sky images. For IR, we base SC_{IR} on the difference between between measured IR and estimated clear-sky values of IR, (IR_{clear}). The differences are denoted as δ_{IR}, which we estimate (based on Fig. 5.2) can be fitted quadratically with SC_{GHI}.

In order to apply the correlations properly, it is necessary to remove early morning and late

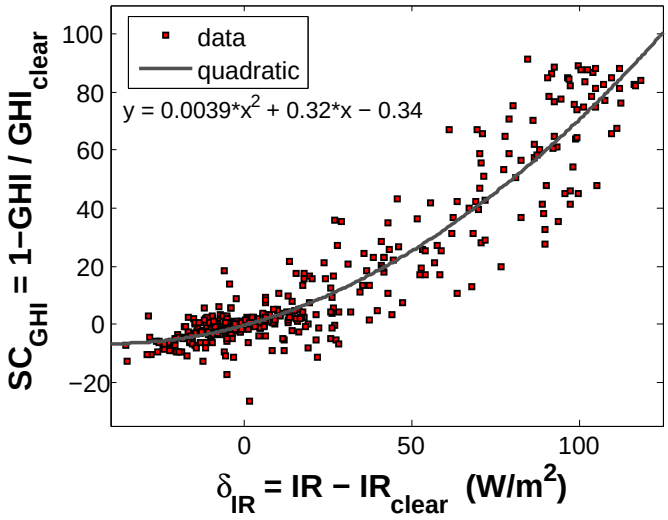

Figure 5.2 – Scatter plots of SC_{GHI} versus δ_{IR}. The blue line is a quadratic fit used to define SC_{IR}. the parameters of the polynomial are also shown under the legend box.

evening hours when estimating the parameters. The reason for this is because errors are easily encountered when calculating SC_{GHI} when GHI_{clear} is small. Also, for a few days in the data set, condensation on the domes of the PSP instruments occurred due to morning fog. Thus, to estimate the parameters for SC_{TSI} and SC_{IR} we use only the day-time data set from 10:00am to 4:00pm to avoid data contamination.

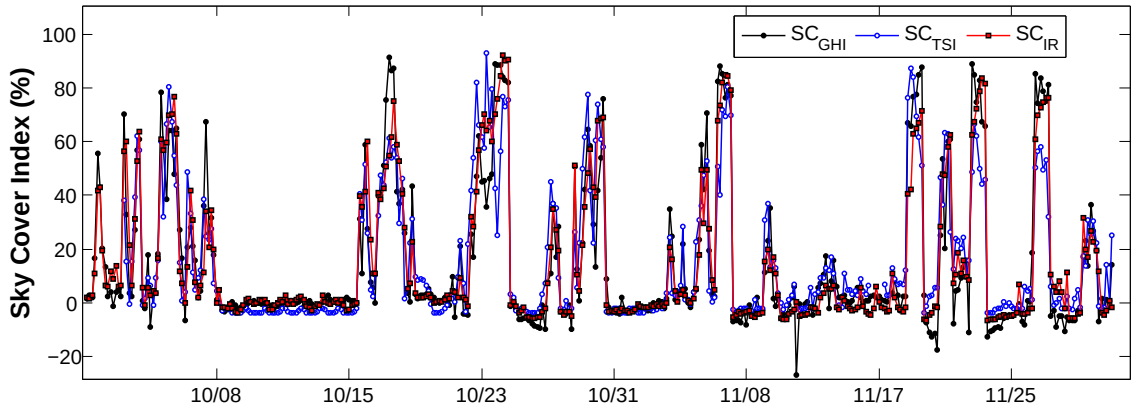

Figure 5.3 – Time series of the sky cover index inferred from the TSI, IR and GHI for October and November, 2010. The night, dawn and dusk values are excluded from the graph. The instrument maintenance day (Nov. 17) was also removed from the set shown.

Figure 5.2, clearly shows strong correlation effects among the GHI and IR sky cover indices. In particular, it seems appropriate to estimate the cloud effects as a function of the difference δ_{IR}= (IR - $\mathrm{IR}_{\mathrm{clear}}$) using a quadratic polynomial fit (see Table 5.1). The polynomial coefficients are calculated based on a least squares regression fit as shown in the figure. As for the $\mathrm{GHI}_{\mathrm{clear}}$, we used the set of 10 clear days. The fit produces an $R^2 = 0.884$ and RMSE = 9.46 W/m^2.

We obtain the values of the parameters in Table 5.1 for the expression of $\mathrm{SC}_{\mathrm{TSI}}$ to be: a = -0.116, b = 1.31, and c = 0.091 by benchmarking the $\mathrm{SC}_{\mathrm{TSI}}$ with $\mathrm{SC}_{\mathrm{GHI}}$. This fit produces an $R^2 = 0.823$ and RMSE = 11.8 W/m^2 which is comparable to the values obtained from correlating $\mathrm{SC}_{\mathrm{IR}}$ with $\mathrm{SC}_{\mathrm{GHI}}$.

The level of quantitative and qualitative agreement of the three sky cover indices discussed above is shown in Fig. 5.3.

5.4 Calculating GHI From Sky Cover Indices

In the previous section we derived relationships between sky cover quantities inferred from TSI, IR, and GHI measurements. Polynomial fits were used to correlate TSI and IR sky cover with GHI sky cover. From these fits we can approximate GHI from TSI and IR by manipulating the equations and using the curve fits for each SC:

$$\mathrm{GHI}_{\mathrm{estimated,IR}} = (1 - \mathrm{SC}_{\mathrm{IR}})\mathrm{GHI}_{\mathrm{clear}}, \tag{5.6}$$

$$\mathrm{GHI}_{\mathrm{estimated,TSI}} = (1 - \mathrm{SC}_{\mathrm{TSI}})\mathrm{GHI}_{\mathrm{clear}}. \tag{5.7}$$

Applying the above GHI estimates from IR and TSI measured values the time-series in Fig. 5.4 is obtained for October 15, 16, and 17. Note that night values are automatically set to zero due to the multiplication of $\mathrm{GHI}_{\mathrm{clear}}$. Both of the estimates agree very well for the days shown, particularly the clearest day. Note the locations of the cusps especially for Nov. 16th. The close agreements obtained here are an indication that the formulation prescribed so far for relating the

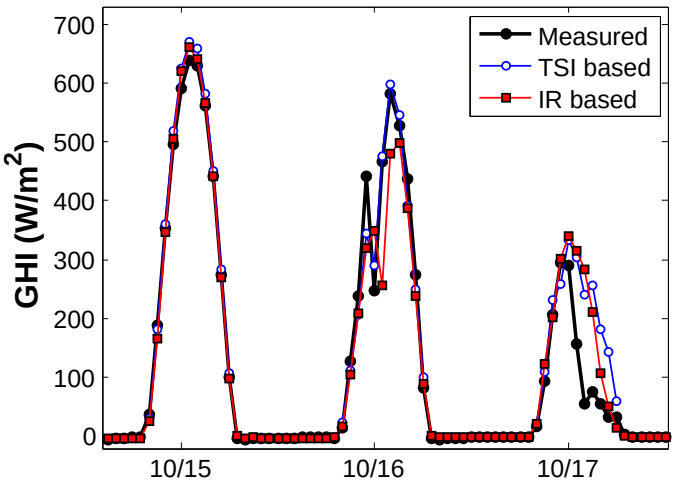

Figure 5.4 – GHI time series measured and estimated based on SC_{IR} and SC_{TSI}. Night values were removed from plot.

values obtained from the GHI, IR, and TSI instrumentation is correct, and thus motivates the use of the SC indices as valid inputs for forecasting models.

A scatter plot (see Fig. 5.5) of the estimated GHI values versus the measured values shows that the GHI estimates are very reliable as the squared correlation coefficients indicate, e.g. $R^2 = 0.935$ for the IR-based model and $R^2 = 0.923$ for the TSI-based model. In terms of modeling GHI, TSI and IR produce similar results with the spread of the IR estimates showing slightly better results.

In summary, the following simple algorithm can be used for modeling GHI based on TSI and IR measured values:

1. Calculate IR_{clear} from temperature and dewpoint temperature measurements;

2. Taking the difference between IR and IR_{clear} compute SC_{IR} using the quadratic polynomial.

3. From SC_{IR} estimate GHI (see Eqn. (5.6)).

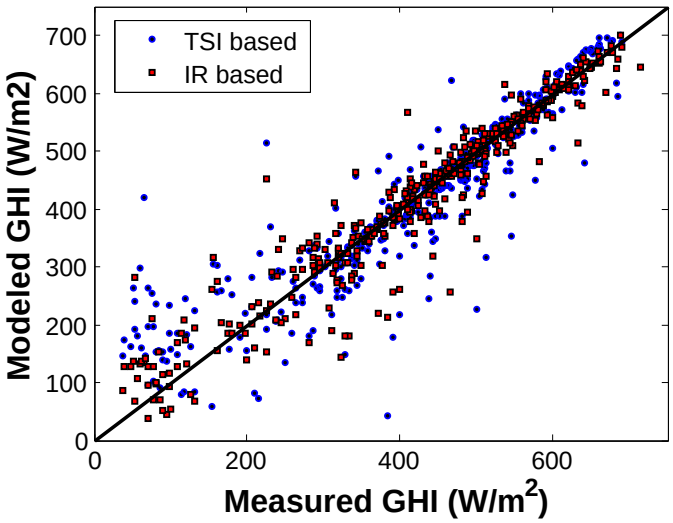

Figure 5.5 – Scatter plot for comparing GHI based on IR and TSI. The correlation coefficients (R^2) for IR and TSI estimates are 0.935 and 0.923 respectively.

Alternatively, one can use a linear combination of opaque and thin TSI data to compute $\mathrm{SC_{TSI}}$ and then from $\mathrm{SC_{TSI}}$ estimate GHI (see Eqn. (5.7)).

5.5 ANN Forecasting of Solar Radiation Using Sky Cover Indices

In this section, we apply the results obtained in the previous sections to the development of a forecast model for GHI. To the knowledge of the authors, no forecast methodology based on TSI based sky cover (cloud effects) for hourly and intra-hourly prediction have demonstrated major gains in accuracy, and none have used IR. The approach we adopt is to forecast the GHI-based SC index at one hour ahead intervals, then use Eqn. (5.2) to revert back to the GHI value.

The forecasting model is mathematically represented as:

$$\begin{aligned} \mathrm{SC_{GHI}(t+1)} = \mathrm{f(SC_{GHI}(t), SC_{GHI}(t-1), \ldots SC_{GHI}(t-n),} \\ \mathrm{SC_{IR}(t), SC_{IR}(t-1), \ldots SC_{IR}(t-n),} \\ \mathrm{SC_{TSI}(t), SC_{TSI}(t-1), \ldots SC_{TSI}(t-n),} \end{aligned} \tag{5.8}$$

where the forecasting input variables include previous values of the SC indices at times t, $t-1$ hr, and up to $t-n$ hrs. The model $f()$ can be a function based on a number of statistical forecast modeling approaches including ones used in solar irradiance modeling (ARIMA, ANNs, k-NN) [64, 10]. We use ANNs as these models have a proven record for solar irradiance forecasting [10].

The ANN model that we select is a feed-forward type composed of one input layer, one hidden layer, and one output layer. The input layer is comprised of the inputs according to the arguments of Eqn. (5.8) and the output layer is the value that we would like to predict $\mathrm{SC_{GHI}}(t+1)$. The number of neurons in the hidden layer is fixed at 10. The activation functions of the hidden layers are sigmoidal and the output neuron has a linear activation function. We use Bayesian regularization to adjust the weights of the ANN synapses, and the models are trained until convergence of the weight values [45].

In order to identify which time-series variables contribute to the best forecasting performance, we apply the ANN model using four input combinations. The first input combination uses only the GHI-based SC index time-series, the second input set consists of SC indices based on GHI and IR, the third input set consists of SC indices based on GHI and TSI, and the fourth input set consists of all the SC indices.

Figure 5.6 shows the results of the ANN forecasting using various SC inputs. The days shown are the same as the ones in Fig. 5.4. One can immediately see the improvement over the results depicted in Fig. 5.4. In particular, the position of the cusp on Oct. 16 is properly reproduced by all ANN that use an additional SC input besides the GHI data. By looking at Oct. 17 one

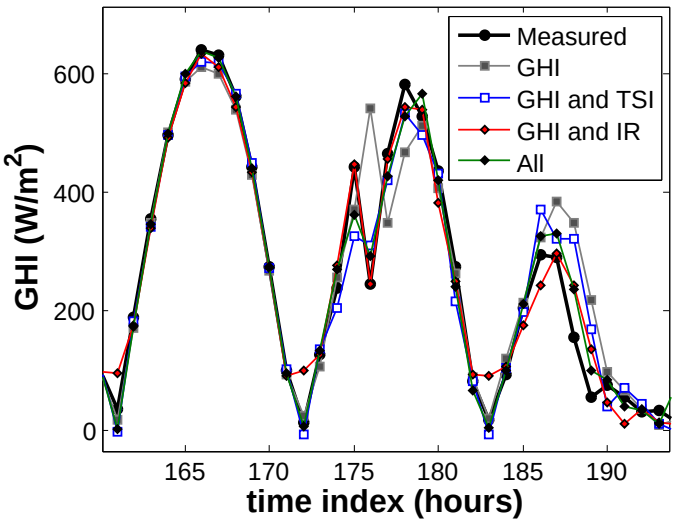

Figure 5.6 – GHI time series for measured and forecasted values based on SC_{GHI}, SC_{IR}, and SC_{TSI}. The legend shows which inputs were included in the forecasting model. Night values are not included.

Table 5.2 – Statistical metrics (R^2, average error, and root-mean-square deviation) for the ANN forecast results based on SC_{GHI}, SC_{IR} , SC_{TSI} , and permutations.

SC_{GHI}	SC_{IR}	SC_{TSI}	R^2	RMSE (W/m^2)	MBE (W/m^2)
✓	–	–	0.952	46.9	**4.1**
✓	✓	–	0.966	39.0	4.5
✓	–	✓	0.977	32.2	6.2
✓	✓	✓	**0.982**	**27.9**	4.6

concludes that the ANN forecasting that uses all three SC indices seems is more accurate. These observation are yet to be confirmed by examining more cloudy days. However, as seen from Table 5.2, the advantage of using TSI and IR data together is clear.

5.6 Conclusions

We examined different strategies for inferring cloud cover from visible image processing and IR measurements as they pertain to the characterization of solar radiation at the ground level. We show that, by defining pertinent sky cover indices, it is possible to accurately model GHI based on measured values from the TSI and IR data. This work suggests that predictive information

is embedded in the measurements obtained from the TSI and IR instrumentation, and that this information should be considered as relevant inputs for solar forecast models. A simple algorithm was developed and tested over several clear and cloudy days in October and November 2010 at the University of California Merced site in order to estimate GHI from both TSI and IR hourly values. Further improvement on GHI modeling is achieved by considering Artificial Neural Network forecast models using various combinations of Sky Cover indices.

We identify two distinctive sources of error that can be improved regarding predictive quality for solar modeling and forecasting include: (1) improved understanding of IR_{clear}; and (2) improved TSI image processing and classification algorithms. Because currently there has been only modest success in including the effects of cloud cover as obtained from meteorological station predictions [8, 7, 9], we propose that the methodology suggested in the present work shows promise in generating improved intra-hour solar forecasting models.

Chapter 6

Forecasting of Global and Direct Solar Irradiance Using Stochastic Learning Methods, Ground Experiments and the NWS Database

We develop and validate a medium-term solar irradiance forecasting model by adopting predicted meteorological variables from the U.S. National Weather Service's (NWS) forecasting database as inputs to an Artificial Neural Network (ANN) model. Since the inputs involved are the same as the ones available from a recently validated forecasting model, we include mean bias error (MBE), root mean square error (RMSE), and correlation coefficient (R^2) comparisons between the more established forecasting model and the proposed ones. An important component of our study is the development of a set of criteria for selecting relevant inputs. The input variables are selected using a version of the Gamma test combined with a Genetic Algorithm. The solar geo-temporal variables are found to be critically important, while the most relevant meteorological variables include sky cover, probability of precipitation, and maximum and minimum temperatures. Using the relevant input sets identified by the Gamma test, the developed forecasting models improve RMSEs for GHI by 10 to 15% over the reference model. Prediction intervals based on regression of the squared residuals on the input variables are also derived.

6.1 Introduction

The Gamma test (GT) is an appropriate tool for identifying relevant inputs, as this test has been demonstrated to be able to provide information regarding the relationship between input and output data sets, even prior to model development [65, 66, 67, 68, 69]. The GT is an algorithm designed to provide an estimation of the lowest possible mean squared error (MSE) attainable by a continuous and differentiable model for some output, y, based on the inputs, $\mathbf{x}$. The criteria for choosing the content in $\mathbf{x}$ can be based on keeping the dimension of $\mathbf{x}$ small (to remove insignificant inputs), meanwhile retaining a low estimate for the MSE. The GT is a relatively simple algorithm to apply and is used here as a basis for the selection of relevant inputs. The selection procedure also involves a genetic algorithm (GA) search in order to efficiently explore possibly significant input combinations. In Section 6.3 the GT and GA procedures are described, and in Section 6.4 the input selection algorithms are evaluated.

After applying the GT and GA to identify which subsets of inputs are potentially useful, artificial neural networks (ANNs) are used to construct the forecasting models. ANNs are described and applied in Sections 6.5 and 6.6. In Section 6.7, prediction intervals are derived which take into account the forecasting uncertainty based on the predicted NDFD-based meteorological conditions.

6.2 Data

The National Weather Service (NWS) manages the National Digital Forecast Database (NDFD) which provides gridded digital forecasts of weather parameters for the entire country at high resolutions of up to 2.5-km spatial and 1-hour temporal [70, 71]. Local forecasts from NWS Weather Forecast Offices (WFOs) are generated by national model outputs, meso-scale model runs and human input. These local forecasts are then merged and assembled on a national grid [70, 71]. Weather forecasted values are publicly available and can be accessed electronically in Extensible Markup Language (XML) format through the NWS website: http://www.weather.gov/ndfd [72].

The forecasted meteorological elements provided by the NWS include ambient temperature, dew point temperature, relative humidity, sky cover, wind speed and direction, probability of precipitation, significant wave height, weather type, and snow amount. Daily maximum and minimum ambient temperatures are also provided by the NDFD.

NDFD meteorological data was collected daily at approximately 12:00 p.m. (Pacific local time) for the period of this study which spans the dates November 1, 2008 – November 30, 2009. The NDFD data sets collected on each day contain same-day forecasted values and forecasted values for the next six days. Since the forecasting methodology is essentially a regression on the NDFD data sets, the solar irradiance forecasts generated here will also be available as the NDFD forecasts are produced (same-day forecasts as well as a few days ahead).

6.3 Model Inputs and Input Selection

To develop the irradiance forecasting models, eleven input variables are considered. Nine of the variables are predicted meteorological variables (described in Section 6.2) and listed in Table 6.1. The other two variables are geometric/temporal variables: the cosine of the solar zenith angle ($\cos Z$) and the normalized hour angle ($\bar{\omega}$, defined later). The geometric variables are important because they describe the deterministic diurnal variations of clear-sky solar irradiation. One of the objectives of this work is to make a determination of which auxiliary meteorological variables are useful for predicting solar irradiation and which ones can be discarded to prevent over complication of the model. In order to do so, the GT is used as a criteria for determining the relevant inputs. With a total of eleven inputs there are $2^{11} - 1 = 2047$ possible subsets of inputs to perform the GT with. Rather than evaluating all possible combinations, a GA search is employed to reduce the input space. The description of the GT and GA procedures are provided after a describing the data preprocessing and introducing the definition of $\bar{\omega}$.

Table 6.1 – List of inputs for modeling. Note: The range of hourly ambient temperature is equal to the maximum of the daily Max Temperature and minimum of the daily Min Temperatures. Wind direction data is given in increments of 10°.

number	name	minimum	maximum
1	Max Temperature (°C)	7.22	40.55
2	Temperature (°C)	-2.78	40.55
3	Dew Point Temperature (°C)	0	37.78
4	Relative Humidity (%)	0	100
5	Sky Cover (%)	0	100
6	Wind Speed (m/s)	0	22.5
7	Wind Direction (deg)	0	350
8	Probability of Precipitation (%)	0	100
9	Min Temperature (°C)	-2.78	22.22
10	cos(Z)	0	1
11	Normalized Hour Angle, $\bar{\omega}$	0	1

6.3.1 Variable Representation and Preprocessing

Table 6.1 lists the input variables that are used for model input selection. In order to keep the notation concise, the input variables are represented as x_j where j is the associated variable number indicated in the first column of Table 6.1. The set of input variables consists of the meteorological variables from the NDFD database the solar geometry variables: $\cos Z$ and $\bar{\omega}$. To avoid scaling issues that can complicate the Gamma test or neural network training, all meteorological input variables are normalized by subtracting the variables by their corresponding minimum values, then dividing by their range (maximum - minimum) so that the values vary from 0 to 1.

6.3.2 Dimensionless Time Scale as an Input

We introduce an additional input for modeling DNI which we refer to as the normalized hour angle defined as

$$\bar{\omega} = \omega/(\omega_{max}), \tag{6.1}$$

where ω is known as the hour angle and ω_{max} is equal to absolute value of the maximum hour angle for a given day while the sun is up; $\omega_{max} = \omega_{sunset} = -\omega_{sunrise}$. These variables are commonly used for conversions between standard time and solar time and are readily calculated using algebraic

relations given in [50]. By definition, $\omega = 0$ at solar noon when the sun is due south and is at its highest elevation for a given day. Observations of DNI daily profiles for clear-sky conditions vs $\bar{\omega}$ are shown in Fig. 6.1. This figure shows that $\bar{\omega}$ is a potentially useful input variable because clear-sky DNI profiles for any part of the year have the same basic shape with respect to $\bar{\omega}$.

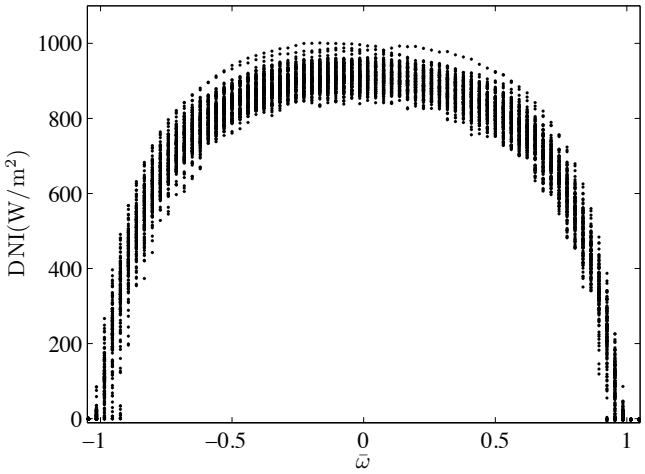

Figure 6.1 – DNI for clear-sky conditions plotted versus normalized time index $\bar{\omega}$. DNI profiles have same basic shape when viewed on this time scale for all parts of the year.

6.3.3 Residual Variance Estimation: Gamma Test

The GT was developed by [73, 74], and further advanced by [75, 66]. The idea behind the GT is to suppose there exists a continuous and differentiable function, f, relating the output, y, to some m-dimensional input vector, $\mathbf{x}$, and has the general form

$$y = f(\mathbf{x}) + r, \tag{6.2}$$

where the residual term, r, represents the uncertainty or noise in the model, and has a mean of 0 and variance σ_r^2.

The procedure of the GT is to first construct the k^{th} $(1 \leq k \leq k_{max})$ nearest neighbor list $\mathbf{x}_{N[i,k]}(1 \leq i \leq M)$ of input vectors $\mathbf{x}_i(1 \leq i \leq M)$, where k_{max} is the maximum number of nearest

neighbors (typically $k_{max} = 10$) and M is the number of data points. The following steps are then applied:

- for $(1 \leq k \leq k_{max})$ compute:

$$\delta_M(k) = 1/M \sum_{i=1}^{M} |\mathbf{x}_{N[i,k]} - \mathbf{x}_i|^2, \tag{6.3}$$

and

$$\gamma_M(k) = 1/(2M) \sum_{i=1}^{M} |y_{N[i,k]} - y_i|^2. \tag{6.4}$$

- construct the linear regression for relationship for the data $(\delta_M(k), \gamma_M(k))$:

$$\gamma_M(k) = \Gamma + A\delta_M(k). \tag{6.5}$$

Provided that the regression line is a good fit, the intercept of Eqn. (6.5), Γ, provides a close estimate of the residual variance σ_r^2 and therefore the lowest attainable MSE. This condition is satisfied when $M \to \infty$ as proven in [75]. The slope A gives a crude estimate of the complexity of the unknown surface of the regression function, $f(\mathbf{x})$. The GT is non-parametric technique and the results apply regardless of the particular methods used to subsequently build a model. This test is particularly suited for the analysis of non-linear regression problems.

An extension of the Gamma statistic Γ is the V_{ratio} parameter defined as the ratio between the variance of the residuals and the variance of the output, $V_{ratio} = \Gamma/\mathrm{Var}(y)$. This parameter can be considered a normalization of the expected MSE and is analogous to the commonly used model quality measure, R^2:

$$\mathrm{R}^2 \approx 1 - V_{ratio}. \tag{6.6}$$

In this paper, we use the V_{ratio} rather than Γ to evaluate the GT outputs.

A sequence of GTs performed for an increasing number of data points is referred to as an M-test

[66]. The M-test is useful because allows one to evaluate the reliability of Γ as an estimate of σ_r^2, and to determine whether enough data is available for model construction. For instance, during initial GT evaluations when the number of data points is small, the M-test plots fluctuate, indicating that the MSE estimates do not agree and are therefore not reliable. As more data is included, the M-test plots begin to stabilize to consistent MSE predictions. If the M-Test plots stabilize, then a degree of confidence that the Γ estimate is reasonably accurate is achieved [66]. In these cases the input/output data will be relatively simple to model. In Section 6.4, the M-test will be applied to verify that enough training data is available and to compare different model inputs.

For a fuller discussion on the GT and the implications for modeling we refer the reader to the reference [66].

6.3.4 Genetic Algorithm Search for Model Input Selection

The selection of the optimal subset of inputs can be accomplished with genetic algorithms (GAs). GAs are optimization search techniques inspired by the process of biological evolution. The algorithms involve optimization searching patterns where alleles (features) of individuals in a population of potential solutions are altered by crossover and mutation operators over generations/cycles so that the fittest individuals continue to evolve [67]. The proportion of individuals that either mutate or crossover are fixed by the mutation and crossover parameters. In the current problem of input selection, the individual fitness is based on minimizing the objective function adopted from [65, 67], which consist of three penalty terms:

$$G(\mathbf{x}_i) = w_\Gamma g_\Gamma(\mathbf{x}_i) + w_A g_A(\mathbf{x}_i) + w_L g_L(\mathbf{x}_i). \tag{6.7}$$

The three penalty terms g_Γ, g_A, and g_L, are monotonically increasing functions of Γ, A, and the ratio of number of inputs in $\mathbf{x}_i$ to total number of inputs, respectively. When selecting the most relevant subset of inputs, $\mathbf{x}_i \subset \mathbf{x}$, the objective function ($G(\mathbf{x}_i)$) encourages competition among three optimality measures. That is, the optimal subset of inputs should 1) produce low

Table 6.2 – Genetic algorithm search parameters for model input selection.

Parameter	Value
Population size	100
Crossover rate	0.5
Mutation rate	0.05
Intercept fitness, w_Γ	1
Gradient fitness, w_A	0.1
Length fitness, w_L	variable (0.1, 0.2, ..., 1)
Run time(s)	600

prediction errors (the Γ value the subset should be low); 2) keep the complexity of the input and output relationship low (value of A should be small); and 3) include only the relevant features. Correspondingly, the fitness scaling parameters in this objective function which must be modified include: 1) intercept fitness weight, w_Γ; 2) gradient fitness weight, w_A; and 3) length fitness weight, w_L.

The scale, w_Γ, corresponds to emphasis on the gamma statistic, Γ. In choosing a combination of inputs, it is preferable to keep inputs which contribute to producing low values of Γ (equivalently, low values of $g_\Gamma(\mathbf{x}_i)$). Therefore, the scale w_Γ is set at a high value of $w_\Gamma = 1$.

As mentioned in Section 6.3.3, the gradient returned by the GT is a crude estimation of the complexity of the model, $f(\mathbf{x})$. Given that A is only a crude estimate, we put little emphasis on this measure, so the scale for this term ($g_A(\mathbf{x}_i)$) in the objective function is assigned a low value of $w_A = 0.1$.

The length fitness parameter, w_L corresponds to the number of inputs to be considered in the model. The value to assign for w_L is not as straight forward because too little emphasis on the length fitness leads to the retention of insignificant or counterproductive inputs. On the other hand, too much emphasis on $g_L(\mathbf{x_i})$ may lead to an overall increase of Γ for the population of inputs in the GA search. Therefore, w_L is left variable and subsets of inputs are considered optimal based on which inputs remain relevant as w_L is varied from 0.1 to 1 in increments of 0.1.

Values of all the GA optimization parameters are listed in Table 6.2.

6.4 Evaluation of Input Selection Algorithms

The GA search is applied using the winGamma computer software. The length fitness scale, w_L, is varied from 0.1 to 1 in increments of 0.1 and the results obtained by the GA search are used to produce the bar plots in Figs. 6.2(a) and 6.2(b). The height of the bars represent the collective frequency (in percent) that each input is included in the best 10% of input subsets which minimized the objective function ($G(\mathbf{x}_i)$). These results indicate that the variable x_{10} ($\cos Z$) is the most important input for modeling GHI. This is expected because $\cos Z$ dictates the deterministic part of the global horizontal solar irradiation. The next most relevant inputs for GHI are x_5 (sky cover), x_8(probability of precipitation), and x_9 (minimum temperature). The variables which seem to be the least important are x_7 (wind direction), and x_4 (relative humidity) which have low frequency in the best 10% of input combinations.

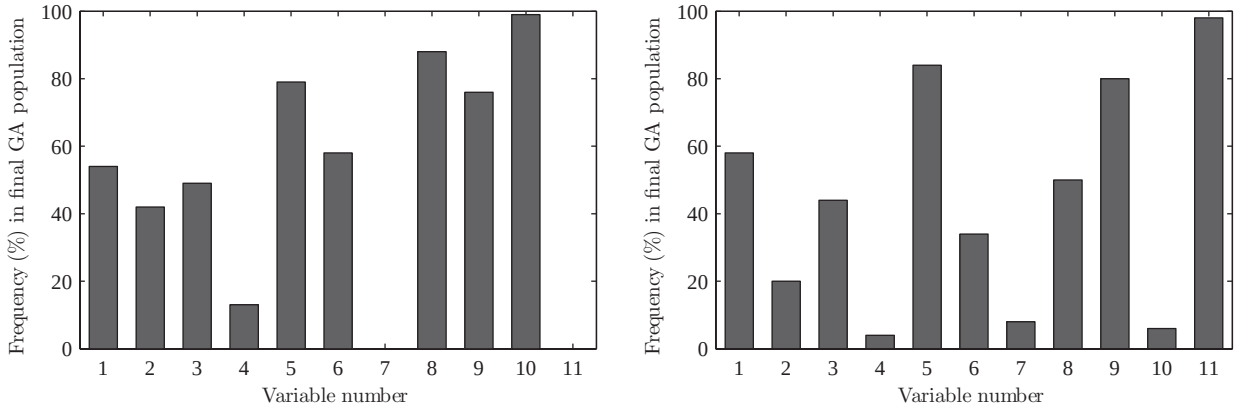

(a) GHI (b) DNI

Figure 6.2 – Genetic algorithm results for model input selection. High frequency of inclusion indicates that the variable is useful for minimizing the objective function, Eqn. (6.7).

Fig. 6.2(a) can be used for choosing which input subsets to consider. Based on Fig. 6.2(a), the combination of inputs to be selected for GHI are subset 1: [x_8, x_{10}]; subset 2: [x_5, x_9,x_8, x_{10}]; subset 3: [x_1, x_2, x_3, x_5, x_6, x_8, x_9, x_{10}] and subset 4: [all variables]. The inputs in subset 1 corresponds to the simplest case where the two variables that were predicted by the GA to have the most significance are used. The size of the input set is incremented in subset 2 by including the

next significant variables: x_5 (minimum temperature) and x_9 (probability of precipitation). Input subset 3 increments subset 2 by including the next most significant variables, and subset 4 contains all the available variables. These input subsets are listed in the second column of Table 6.3(a).

The relevant inputs for DNI are slightly different than for GHI. The most relevant inputs appear to be x_5 (sky cover), x_9 (minimum temperature), and x_{11}(normalized hour angle). The four subsets selected for modeling DNI are subset 5: [x_5, x_9, x_{11}]; subset 6: [x_1, x_3, x_5, x_8, x_9, x_{11}]; subset 7: [x_1, x_2, x_3, x_5, x_6, x_8, x_9, x_{11}]; and again subset 4: [all variables]. These input subsets are listed in the second column of Table 6.3(b).

An M-Test is performed on the selected inputs and the results are plotted in Figs. 6.3(a) and 6.3(b). As described in Section 6.3.3 the reliability of the GT can be inferred from the stability of the M-Test plots. All GHI M-test plots appear to have stabilized indicating that enough data is obtained and that the GT results are reliable. It is clear from Fig. 6.3(a) that the variables x_8(probability of precipitation) and x_{10} ($\cos Z$) alone will not be enough to produce the most accurate models. The M-test results for DNI (Fig. 6.3(b)) are similar in that the variables x_5 (sky cover), x_9 (probability of precipitation), and $x_{11}(\bar{\omega})$ will not give the best possible model accuracy.

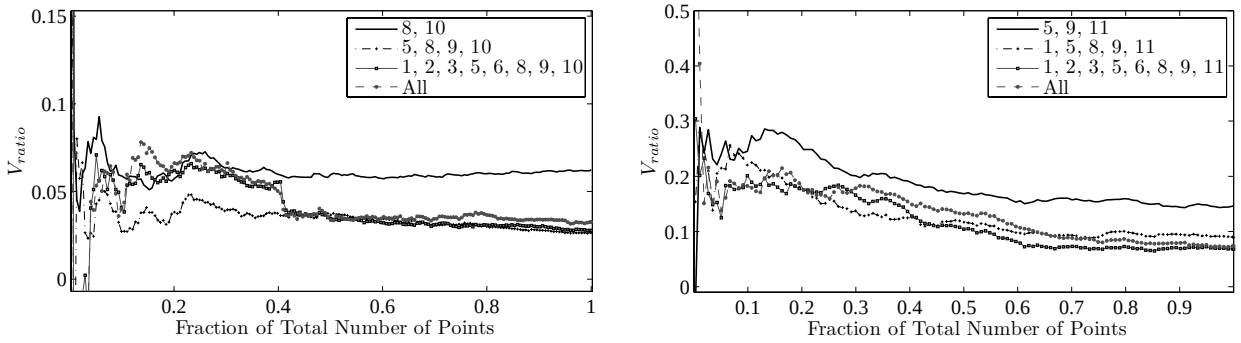

(a) GHI (b) DNI

Figure 6.3 – M-Tests for various input subsets (as indicated in the legend) which were selected based on results obtained from GA results. The V_{ratio} on the vertical axis is an estimate of the normalized MSE, i.e. $\approx 1 - R^2$. The total number of data points for GHI is 4472 and for DNI is 3738.

6.5 Artificial Neural Networks

Artificial Neural Networks (ANNs) are useful tools for approximating complicated mapping functions for problems in classification and regression [59], and have also been used extensively in many areas including solar radiation modeling. [10] gives a review of over 40 applications of ANNs and other artificial intelligence techniques applied to solar radiation modeling. The advantage of ANNs is that no assumptions are required about the underlying process relating input and output variables. However, because ANNs are universal approximating functions, their mapping capabilities can potentially lead to problems such as over-fitting training data [59], and thus leading to poor generalization on new data sets. To prevent overtraining [76], for example, used an approach to construct network architectures based on Bayesian and sensitivity analysis where coincidentally the methodology identifies relevant inputs as well as an appropriate neural network architecture in the case of modeling the direct normal irradiance. Another approach which addresses the issue of overtraining and model input selection simultaneously is based on the GT (see e.g., [68, 69] for application on modeling daily values of GHI). The principal advantage of the GT approach over the Bayesian approach is the simplicity of the theoretical underpinnings behind the methodologies. The GT results obtained in Section 6.4 are used here to prevent overtraining with ANNs.

An ANN is a specific representation of y in terms of some input variables $\mathbf{x}$. The ANN representation is based on signals being sent through elements called neurons in such a way that the processing of the inputs signals produces an output, y, that is sufficiently close to the desired target value of t. Neurons are arranged in layers, where the first layer contains the set of inputs, the last layer contains the output, and the layers in between, referred to as hidden layers, contain hidden neurons. A feedforward neural network with N inputs and N_h neurons in one hidden layer with a linear output activation function can be expressed as

$$y = f(\mathbf{x}, \mathbf{w}) = \sum_{k=0}^{N_h} w_k f_k^{hidden} \left(\sum_{j=0}^{N} w_{j,k} x_j \right). \tag{6.8}$$

where f_k^{hidden} are sigmoidal functions, such as the hyperbolic tangent function. A characteristic of feedforward neural networks is that the neurons are successively interconnected from layer to layer where neurons in one layer affect all neurons in the next but do not affect other neurons in the same layer or any preceding layers. Numerical optimization algorithms such as back-propagation, conjugate gradients, quasi-Newton, and Levenberg-Marquardt have been developed to efficiently adjust the weights, $w_{k,j}$ and w_k in the feedforward neural networks so that the minimization of some performance function is achieved on some training data. Typically the performance function used for adapting the weights is the MSE.

$$\text{MSE} = \frac{1}{M}\sum_{i=1}^{M}(y_i - t_i)^2. \tag{6.9}$$

6.6 Model Development and Evaluation

The MATLAB NEURAL NETWORK TOOLBOX was used to construct regression models for GHI and DNI where the inputs consists of same-day forecasted meteorological variables. The same-day forecasted NDFD data was randomized and split into two categories consisting of a training set and a test set. The proportions of each set are based on the results of the M-test (Figs. 6.3(a) and 6.3(b)). Accordingly, the training set consists for 60% of the randomly selected points of the entire data set to train the GHI neural networks and 80% to train the DNI neural networks. The neural network architectures are based on the feed-forward structure described in Section 6.5 where the input layer consist of the inputs from the four subsets suggested in Section 6.4.

6.6.1 Forecasting Model Training

Eight ANN models were trained and tested to forecast solar irradiation. Models 1 to 4 forecast GHI and Model 5 to 8 forecast DNI. In each training cycle (epoch), all the training data is presented to the ANN in random batches and the MSEs are computed. The weights are adapted using

Table 6.3 – Statistical summary of trained neural network models and comparison with persistent and Perez Model. Best values are denoted in bold fonts.

(a) GHI

		Training			Test		
Model	Inputs	MBE[W/m^2] (%)	RMSE[W/m^2] (%)	R^2	MBE[W/m^2] (%)	RMSE[W/m^2] (%)	R^2
1	$[x_8, x_{10}]$	**+0.38 (+.1)**	77 (19.3)	0.939	**+0.60 (+.1)**	89 (22.8)	0.915
2	$[x_5, x_8, x_9, x_{10}]$	-1.35 (-0.3)	67 (17.2)	0.952	-3.23 (-.6)	**72 (17.7)**	**0.947**
3	$[x_1, x_2, x_3, x_5, x_6, x_8, x_9, x_{10}]$	-2.25 (-0.5)	63 (15.7)	0.959	-3.10 (-.6)	73 (18.5)	0.945
4	[All]	-1.94(-0.5)	**58 (14.8)**	**0.965**	-2.10 (-.5)	74 (18.6)	0.942
Persistent GHI		–	–	–	-1.5 (-0.4)	123.1 (31.1)	0.854
Perez Model		–	–	–	-10.73 (-2.50)	84 (21.7)	0.921

(b) DNI

		Training			Test		
Model	Inputs	MBE[W/m^2] (%)	RMSE[W/m^2] (%)	R^2	MBE[W/m^2] (%)	RMSE[W/m^2] (%)	R^2
5	$[x_5, x_9, x_{11}]$	**-1.5 (-0.3)**	171 (35.0)	0.763	**-2.4 (-0.5)**	162 (32.3)	0.781
6	$[x_1, x_3, x_5, x_8, x_9, x_{11}]$	-2.7 (-0.5)	142 (29.1)	0.835	-3.4 (-1.3)	**156 (31.2)**	**0.801**
7	$[x_1, x_2, x_3, x_5, x_6, x_8, x_9, x_{11}]$	-6.3 (-9.5)	148 (30.1)	0.821	-7.1 (-10.3)	161 (33.2)	0.788
8	[All]	-1.3 (-1.9)	**138 (28.1)**	**0.845**	-4.2 (-8.3)	158 (32.0)	0.797
Persistent DNI		–	–	–	-8.40 (-1.7)	270 (54.5)	0.404

Levenberg-Marquardt learning algorithm and the stopping criteria for neural network training is based on continued training until the R^2 reaches the Gamma test output, V_{ratio}, or for a maximum of 100 epochs. The number of neurons in the hidden layer was kept at 10 to 20 neurons. When more neurons were used, larger discrepancies of the model quality statistics between the training and testing sets were observed and as a result the ANN models generalized more poorly.

6.6.2 Benchmark Reference Models: 24-H Persistent Model and Perez Model

For the purpose of comparisons, we include a persistent model defined as the model that estimates the solar irradiance as having the same hourly values as the previous day, i.e., the persistent model used here is a 24-hour persistent model.

The Perez GHI forecasting model [8] which has been validated at a number of locations is also

applied here. The Perez model relates GHI to sky cover (SC) as:

$$\mathrm{GHI} = \mathrm{GHI}_{\mathrm{clear}}(1 - 0.87SC^{1.9}), \tag{6.10}$$

where SC is the sky cover values obtained from the NDFD forecasts. Estimates for $\mathrm{GHI}_{\mathrm{clear}}$ are obtained using a Linke Turbidity factor of 3 as per [77].

6.6.3 Statistical Evaluation Metrics

The eight models differ by their inputs as is indicated in Table 6.3(a) and 6.3(b). The model quality metrics used for comparisons of the different models include the R^2, RMSE, and relative RMSE (rRMSE), which are calculated using the following equations:

$$\mathrm{R}^2 = 1 - \frac{\sum_{i=1}^{M}(y_i - t_i)^2}{\sum_{i=1}^{M}(t_i - \bar{t})^2}, \tag{6.11}$$

$$\mathrm{RMSE} = \sqrt{\sum_{i=1}^{M}\frac{1}{N}(y_i - t_i)^2}, \tag{6.12}$$

$$\mathrm{rRMSE} = \mathrm{RMSE}/\bar{t}, \tag{6.13}$$

$$\mathrm{MBE} = \sum_{i=1}^{M}\frac{1}{N}(y_i - t_i), \tag{6.14}$$

and

$$\mathrm{rMBE} = \mathrm{MBE}/\bar{t}. \tag{6.15}$$

In the above definitions, y_i are the predictions from the ANNs, t_i, are measured values of GHI or DNI, and $\bar{t}$ are the averages of GHI or DNI for the training or test set. Night values (values which occur when $\cos Z < 0$) are removed when computing each of the statistical quantities.

6.6.4 Forecasting Model Evaluations

All models proposed here show major improvements over the 24-hour persistent model. The improvement is most apparent for the DNI forecasting models (see Table 6.3(b)). By comparing the statistical measures for training and test sets of each model, we notice there are significant improvements over the simpler models with the least inputs. As can be the case in modeling with ANNs, better training performance is achieved when more inputs are used. However, the use of more inputs does not necessarily translate to better generalization or ability to forecast. The results in Tables 6.3(a) and 6.3(b) show that models with intermediate complexity perform best on both training and test sets.

As indicated by the RMSE and R^2 values, Perez's 2010 model [8] compares well with Model 1, which includes the same inputs (note that clear sky GHI is approximated well by $\cos Z$). In this case, Perez's model should be favored over Model 1 because the later employs fewer parameters than Model 1, and no additional errors due to excessive computations are incurred. The Perez model has only two parameters whereas the ANN method requires over 20 parameters and is therefore overly complex in this case. However, a comparison between the MBE values for the ANN and Perez's models show that there is room to improve over Perez's simple model. If we take Perez's model as the baseline for RMSE comparisons, Model 1 underperforms by 6%, whereas Models 2-3 improve over Perez's model by over twice the same amount, indicating that the stochastic approach with more inputs represents a true gain that compensates for the additional complexity in computation. Again, some of these results were expected from the M-tests (see Fig. 6.3(a)).

It is also interesting to compare results from Tabs. 6.3(a) and 6.3(b) with the M-test results in Figs. 6.3(a) and 6.3(b). In comparing the actual training R^2s of each model with those predicted from the M-tests, we see that they are quite close, in particular, for the GHI models. For example, according to the M-test for Model 1, we could have expected an $R^2 \approx 0.945$, which is close to the actual $R^2 = 0.939$. The training R^2s for GHI are generally much closer to what was predicted in the M-test than for DNI. This is likely because the M-test plots have stabilized with a relatively

smaller proportion of data (at $\approx 45\%$) as compared to DNI (M-test plots do not stabilize until after $\approx 80\%$ of total number of data points used). This also indicates GHI is much easier to predict than DNI and that additional data will be required to obtain better models for DNI.

One concern for using a larger input set is that the prediction errors of each input directly propagates to errors in forecasting the output. In order to observe the propagation of the NDFD uncertainty, the forecasting errors for all models for same-day and several days ahead are shown in Figs. 6.4(a) and 6.4(b). These figures illustrate that forecasting errors increase with forecasting lead-times as a result of uncertainty in the next few days of the inputs from the NDFD. This point is explained more explicitly in the next section. A general observation from these figures is that models with fewer inputs have lesser nominal increases in forecasting errors with respect to forecasting horizon. In addition, as the forecasting horizon increases to four or more days ahead there is less of a difference between each of the models, and so the preferred models would be Model 1 and Model 5 because fewer inputs are involved.

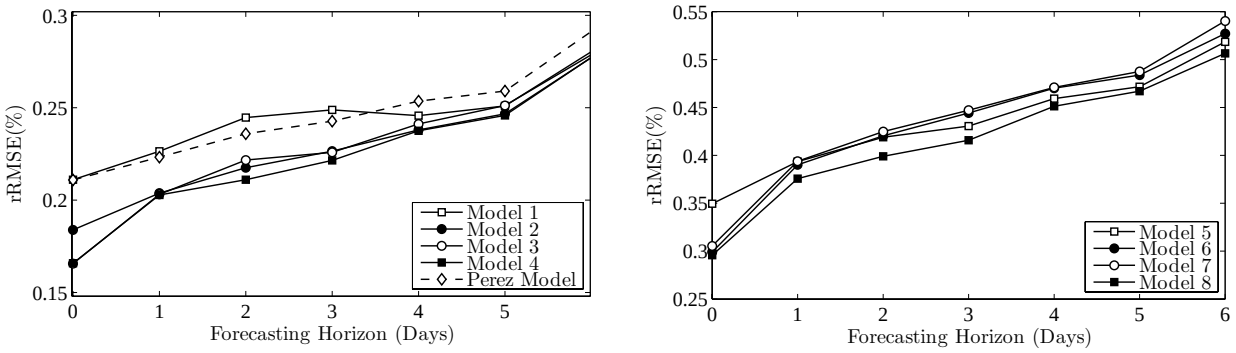

(a) GHI (b) DNI

Figure 6.4 – The relative RMSE (%) for forecasts using models with different inputs as indicated in the legend on graph. The horizontal axis represents the number of days ahead where 0 denotes same-day.

The rRMSEs given so far are a measure of model quality over the entire data set. In some cases it may be important to know if there are certain periods when the solar radiation is more predictable. The rRMSEs for GHI Model 3 and DNI Model 7 are calculated on a monthly basis to produces Figs. 6.5(a) and 6.5(b). For both models the rRMSEs are lower than the aggregated

rRMSE during the months between and including March through September. It is also apparent from these figures that during the summer months solar irradiation (GHI and DNI) is much more forecastable.

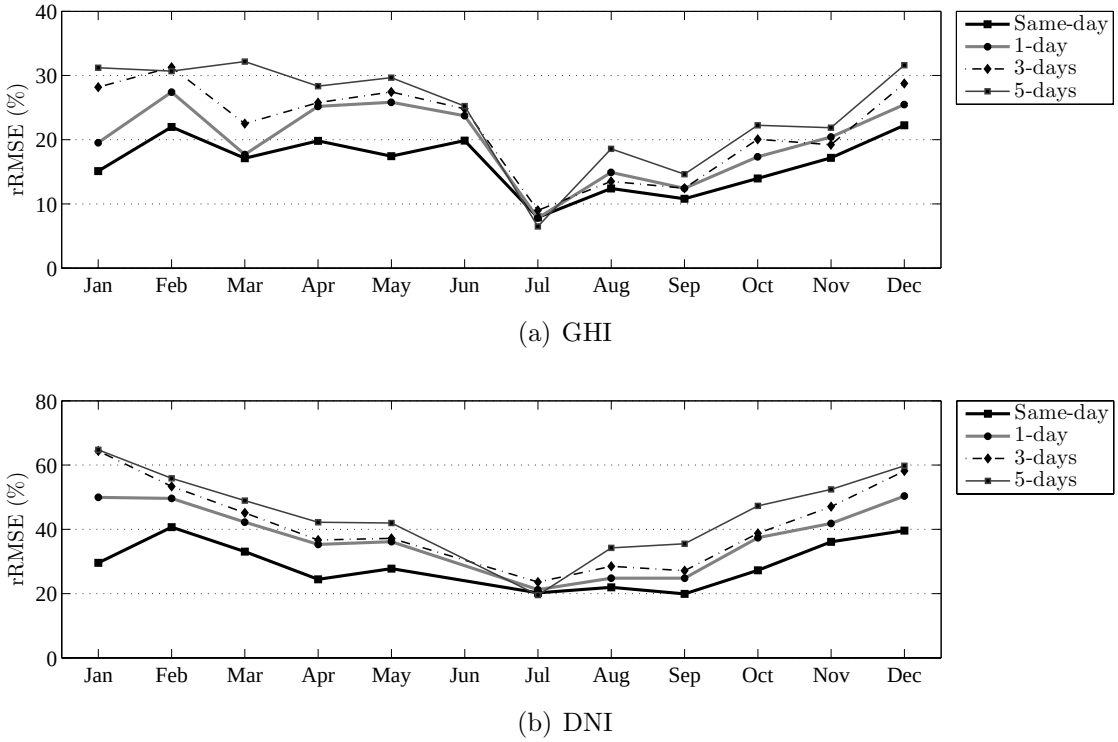

(a) GHI

(b) DNI

Figure 6.5 – The relative RMSE by month from beginning of November 2008 to end of November 2009. The rRMSEs are normalized with respect to $\text{GHI}_{mean} = 474\text{W/m}^2$ and $\text{DNI}_{mean} = 541\text{W/m}^2$. The rRMSEs are for modeling DNI for same-day and forecasts one to six-days ahead as indicated by legend on graph. The DNI data sets for June 2009 were deemed unreliable due to mechanical problems with the measurement tracking system, and therefore these values are not reported here.

6.7 Prediction intervals

As a post-analysis step, prediction intervals are provided in order to examine how model and forecasting uncertainty depends the type of sky situation. For instance, as shown in Figs. 6.5(a) and 6.5(b), model and forecasting accuracy is generally much better during summer months when there are few cloudy days. Similar as in [24, 12], prediction intervals are derived here by analyzing

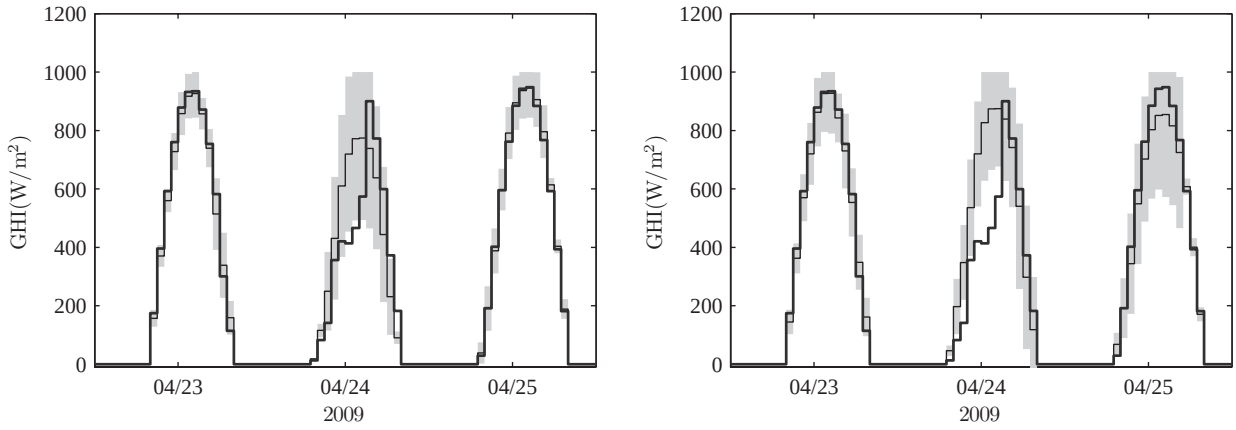

(a) Same-day forecasted hourly values and measured values.

(b) One-day ahead forecasted hourly values and measured values.

Figure 6.6 – Forecasts from Model 3 with prediction intervals for hourly GHI. The dark-bold lines are the measured values, the thin lines are the predictions, and the shaded regions are the 95% confidence intervals.

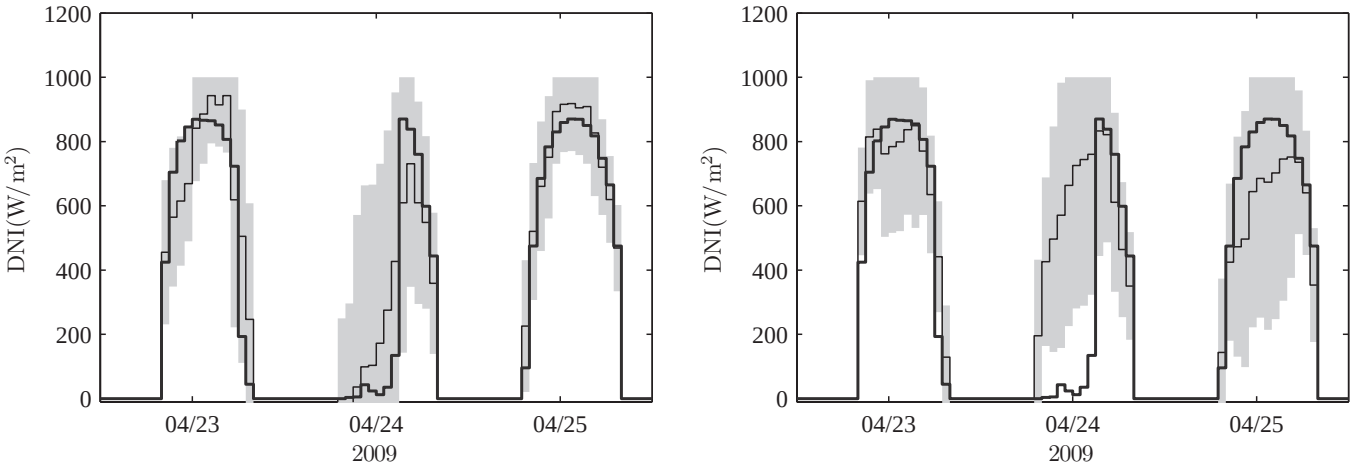

(a) Same-day

(b) One-day ahead

Figure 6.7 – Forecasts with prediction intervals for hourly DNI. The dark-bold lines are the measured values, the thin lines are the predictions, and the shaded regions are the 95% confidence intervals.

the residuals.

To construct the prediction intervals we make a few assumptions regarding the distribution of the residuals. One of the assumptions is that the expected value, or mean value, of the residuals (r) given some value of the inputs $\mathbf{x}$, denoted as $\mathsf{E}(r|\mathbf{x})$, is equal to zero, $\mathsf{E}(r|\mathbf{x}) = 0$. The next assumption

is that the residuals with the expectation value $\mathsf{E}(r|\mathbf{x}) = 0$ and variance $\mathrm{Var}(r|\mathbf{x}) = \mathsf{E}(r^2|\mathbf{x})$ are normally distributed. Then letting $s(\mathbf{x}) = \sqrt{\mathsf{E}(r^2|\mathbf{x})}$, the prediction limits of the models can be computed as

$$y_{prediction\ limits} = f(\mathbf{x}) \pm z_{\alpha/2} s(\mathbf{x}), \tag{6.16}$$

where $z_{\alpha/2}$ is the z-score for the confidence level $1 - \alpha$. For 95% confidence levels, $z_{\alpha/2} = 1.96$. In [12], $s(\mathbf{x})$ was modeled using a fourth degree polynomial using the predicted clearness index and cloud cover. Similarly, we applied regression using ANNs to produce model estimates of $s(\mathbf{x})$.

Figs. 6.6(a) show time-series plots of measured and modeled GHI with prediction bands for same-day forecasts. The upper limits of the bands were limited to a maximum value of 1000W/m^2. Although approximately 95% of all the observed points fell within the confidence intervals, most of the departures were clustered on a few days, while most days had no departures. These systematic departures are probably due to errors in the inputs for which the estimates of prediction bands are based on.

For clear days, the prediction bands are relatively narrow indicating that GHI is very predictable for clear-sky situations. For days with more sky cover, however, irradiance is much less predictable as indicated by the wider prediction bands. Fig. 6.6(b) shows one-day ahead predictions of GHI for the same days as in Fig. 6.6(a). These results coincide with previous results from [24, 12], where they characterized larger forecasting uncertainty during partly cloudy to overcast conditions for solar power and irradiance model predictions, respectively.

Fig. 6.8 shows sky cover values for the same days used in the prediction interval plots. For the day 4/24/2009, the 1-day ahead forecasted hourly values are underestimated, and thus the prediction bands are smaller for the 1-day ahead irradiance predictions than the same-day predictions. The opposite is true for the sky cover and predictions bands for 4/25/2009. These figures show that forecasting uncertainty is proportional to sky cover and also that the irradiance predictions and prediction intervals are directly related to sky cover forecasting uncertainty.

One can also compare the prediction intervals for same-day forecasts with 1-day ahead forecasts

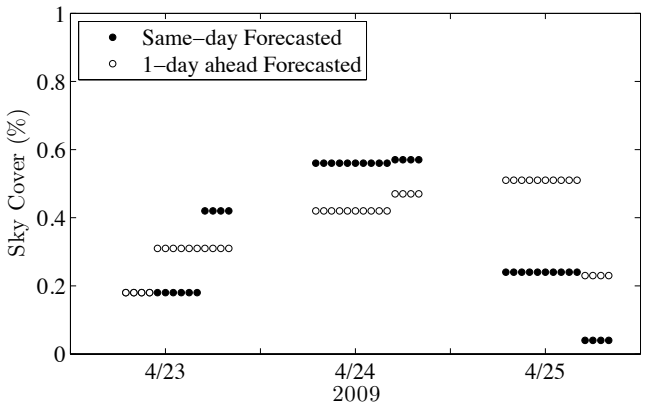

Figure 6.8 – Hourly values of sky cover for same days used in the prediction interval plots. Night values were removed.

for DNI, Figs. 6.7(a) and 6.7(b). The prediction intervals for DNI are much wider than for GHI, further illustrating that DNI is relatively more difficult to reliably predict.

6.8 Conclusions

We developed forecasting models for hourly solar irradiation using artificial neural networks for lead times of up to six days. Model inputs included current and forecasted meteorological data obtained from the U.S. National Weather Services forecasting database, and solar geotemporal variables. The normalized hour angle was introduced as an effective input for modeling and forecasting solar irradiation. An input selection scheme was applied using the Gamma test combined with a master genetic algorithm-based method to reveal the most relevant set of inputs which included the solar geometry variables, sky cover, probability of precipitation, and minimum and maximum temperatures.

For same-day forecasts of GHI, rRMSEs range from 15 to 22% for different models constructed on 13 month data set. The same-day forecasts show that the models constructed here compare favorably to those of satellite-based models [77, 78, 79], and other medium-range (lead times of one to six-days) forecasting models [12, 24, 80, 71, 8]. Implementation of Perez's latest GHI forecasting model to the data set used here yields an RMSE of 84.5W/m^2 (rRMSE = 21.7%) for same-day

forecasts which compares well with one of our simple models that uses the same inputs. Models with slightly larger sets of inputs generally perform better for same-day and 1-day ahead forecasts. The DNI forecasting models were not compared to any established models because their is none available to compare. However, this study finds DNI to be generally much more difficult to predict reliably: rRMSEs obtained on same-day forecasts are in the range of 28 to 35%. This trend is in agreement with previous satellite-based studies (see e.g., [79]).

In general, and as expected, the models lose accuracy with increasing forecasting horizon but less sharply during the summer than during the winter months. This is due to long periods of consecutive clear days in the summer and a large number of cloudy to overcast days during the winter for California's Central Valley. These weather characteristics are important for the siting and operation of solar farms, since the high irradiation summer months coincide with peak power demand in the region. Solar power is not only abundant in the region studied, but it is also very predictable during the peak demand season.

Chapter 7

Characterization and Cost Analysis of UC Merced's Campus Load and 1-MW PV Plant Variability

Variability and uncertainty in renewable energy generation has a direct impact on the cost of electricity prices because of the potential impacts on the operation of existing power generating units. The purpose of this paper is to present a case study detailing the variability added to the UC Merced campus load after including a 1-MW photovolataic (PV) plant to supply a significant amount (25-30% of maximum demand) of the energy load. Cost estimates of the required mechanisms to compensate for the variability are calculated based on utility prices and the PV fluctuations. Then these results are correlated with solar power variability. Additionally, a simulation is performed for a battery storage system to mitigate the PV fluctuations. These simulated costs are also correlated with three variability metrics including the standard deviation of the fluctuations and the mean absolute values of the fluctuations. In order to extrapolate results from the case study to a more general scenario, we show that the obtained correlations can be useful for providing estimates on the financial impacts of variable generation resources based on more widely available solar irradiance data.

7.1 Introduction

A major challenge of integrating solar power systems is the addition of variability onto the electrical grid, in particular for large centralized PV systems. While variability reduction can be achieved through geographic diversity and smoothing [32, 81, 33, 35, 36], i.e., distributed PV systems, there are still concerns that at large penetration levels of renewable energies, the variability may significantly impact electricity markets [35, 37] as well as cause other technical issues [6]. Currently, the grid operates with most of the uncertainty coming from the demand side. To handle the uncertainty due to the unpredictable variability, transmisssion operators (ISOs) must make sure to allocate additional reserve capacity [37, 38]. With the exception of hydro, reserves with fast-ramping capabilities are typically comprised of the more expensive generating units and thus uncertainty has the effect of creating higher electricity prices [38].

In [32, 81, 36], the authors demonstrate the possibility to significantly reduce fluctuations from distributed PV systems as opposed to a single reference location. While this is one way to manage the fluctuations produced from PV plants, it is questionable whether the advantages of geographic diversity of PV systems outweigh the benefits of economies of scales of large centralized plants. Furthermore, [39] argues that managing variability in renewable energy resources is technically feasible; but social, political – and hence, economical – obstacles hinder the integration of renewable energy sources. Therefore, it is important to quantify the cost of the fluctuations produced by renewable electricity generation, in addition to developing methods to manage the variability of the electricity produced by solar power systems.

The objectives of this study are to 1) compare the PV power output (P_{PV}) and Global Horizontal Irradiance (GHI) variability for 15-min time-scales, 2) provide estimated relative costs associated with the utilities carrying the burden of compensating for P_{PV} fluctuations, 3) model the cost for a scenario where it is the system owner's responsibility to mitigate P_{PV} fluctuations using a battery as a dispatchable storage system. The first objective is interconnected with the second and third because the costs depends on the amount of variability. For this reason, we use variability as a metric

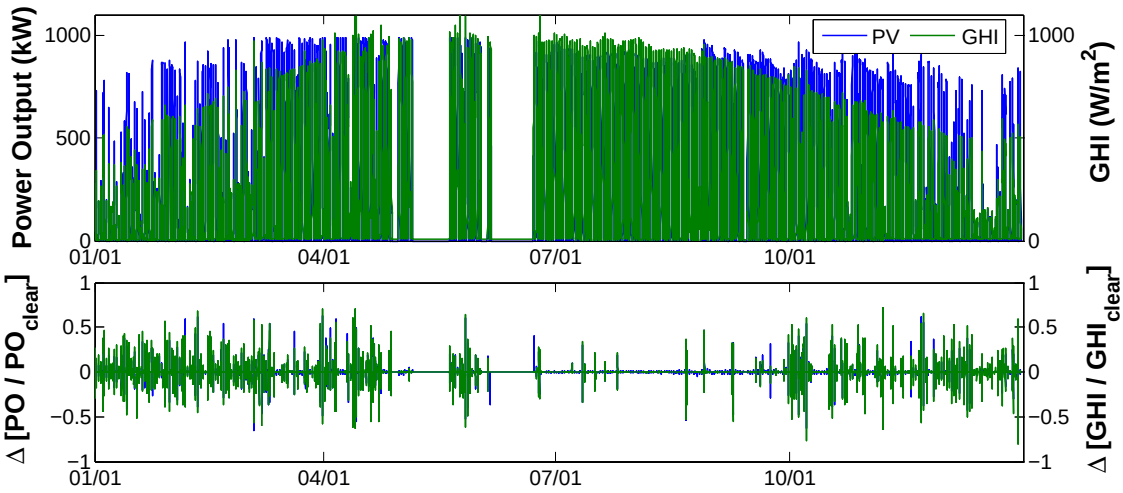

Figure 7.1 – Comparing PV power output variability with global horizontal irradiance variability.

for estimating cost of fluctuations. It will also be shown that quantifying solar variability allows for making cost estimates by using solar irradiance data. Using solar irradiance data is beneficial since actual PV data is presently limited while solar irradiance data is much easily accessible.

7.2 Solar Irradiance And Power Output Variability

In November 2009, UC Merced deployed a SunPower PV system provided with single axis tracking comprising of 4880 photovoltaic panels installed across an area of 6072 m^2 with a power capacity of 1.12 MW. A Global Horizontal Irradiance (GHI) sensor has also been located on site at the center of the plant on an elevated surface. At the time of the writing of this document only 15-min and 1-hr averaged data has been available. For this study, the 15-min data is used to characterize the 15 minute ramps observed in the PV power output (P_{PV}), the solar irradiance (GHI), and the load data (P_L).

7.2.1 Normalization and Fluctuations of Solar irradiance and PV power output

The variability of GHI and P_{PV} can be characterized by the ramps calculated from their time-series. Here, as well as in other studies of solar irradiance variability [33, 35], the weather related fluctuations are calculated in terms of the clearness index (K^*_{GHI}) defined as

$$K^*_{GHI} = \frac{\text{GHI}}{\text{GHI}_{\text{clear}}}. \tag{7.1}$$

By normalizing GHI with a $\text{GHI}_{\text{clear}}$ model the variations due to solar position and seasons are removed. Therefore, the fluctuations of the time-series, K^*_{GHI} are entirely attributed to short-term weather variations such as passing clouds.

The fluctuations of the P_{PV} are characterized by normalizing the P_{PV} with respect to the nominal capacity rating of the PV power plant, $P_{PV,\text{max}}$;

$$P'_{PV} = \frac{P_{PV}}{P_{PV,\text{max}}}. \tag{7.2}$$

where $P_{PV,\text{max}} = 1$ MW. The data for the time series of P_{PV} and GHI used in this study were collected from the date range of Jan.–Dec. 2010. The top graph in Fig. 7.1 shows the time series for each variable over the range of dates. Some days in May and June 2010 were removed because of an inverter failure. It can be seen from the top graph, the GHI has cyclic seasonal variations while P_{PV} is relatively less seasonal because of the single-axis tracking and the latitude inclination of the PV panels. On the bottom graph of Fig. 7.1, the time series of the step changes (ramps) of P_{PV} and GHI are plotted. Both the fluctuation time series seem to exhibit a semi-stationary pattern (averages are approximately constant for any segment in the time-series).

The fluctuations can be summarized by computing the standard deviations,

$$\sigma(\Delta x) = \sqrt{\frac{1}{N}\sum \Delta x^2} \tag{7.3}$$

where x is either the P_{PV} or GHI. In computing the standard deviations, the night values are ignored since the GHI and P_{PV} have values of zero and do not contribute to the characterization of weather-based variability. The standard deviation is computed for a set of points which can include a day, month, season, etc. In the next section we will consider monthly standard deviations.

7.2.2 Monthly and Annual Variability

Figure 7.2 shows monthly calculated standard deviations of the 15-min relative P_{PV} and GHI step changes. The monthly variation of the standard deviations is similar for P_{PV} and GHI . The months from June to September are characterized as low variable months. This characteristic of small variability in particular makes solar power utilization economical for the study site since there is lower variability in the summer and higher solar irradiance.

The standard deviations range from approximately 3–12%, the single fluctuations however can reach up to 60%. The ramp probability distributions shown in Fig. 7.3 again shows the equivalence of the ramps between the PV and solar variability. A normal (Gaussian) distribution with the same standard deviation of the P_{PV} fluctuations is also shown for reference. Note that the probability distribution have higher tales than a normal distribution. For example, in a normal distribution ($N(0, \sigma_{\Delta P'})$), 3 standard deviations corresponds to 9–36%, making a 50–60% ramps very unlikely which is contrary to what is found in the data. Probability and cumulative distributions for multiple GHI sensors and PV systems have also been examined in [44, 47, 35].

7.3 Campus Load Variability

This section describes the impact of variability in P_{PV} on the UC Merced campus' power demand (P_D) from Pacific Gas and Electric Company (PG&E) in order to balance the net campus load (P_L). Annual 15-min time series from January–December 2010 for UC Merced campus load, power supply from PG&E and power output from solar panel is used for this analysis.

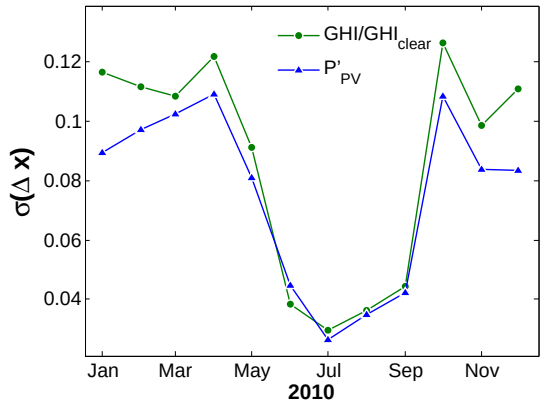

Figure 7.2 – Variability of Power Output on a Monthly basis.

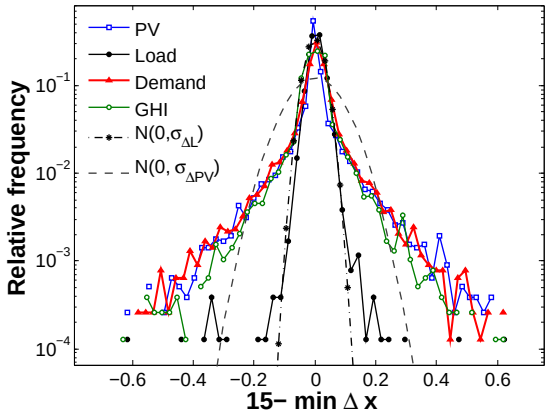

Figure 7.3 – Probability distribution of power output, load, demand and GHI fluctuations. Normal distribution are included for reference.

7.3.1 Description of UC Merced campus load

On clear days, as shown in Fig. 7.4, the UC Merced's 1-MW PV plant serves approximately one-third of the campus load during the day-time. The net campus power demand (P_D), defined as

$$P_D = P_L - P_{PV}, \tag{7.4}$$

is met by purchasing electricity from PG&E. The centralized HVAC system for UC Merced, also referred to as the Central Plant, consumes a significant part of campus load (included in Fig. 7.4) because it provides all the heating, cooling, steam and hot water to the campus. It contains

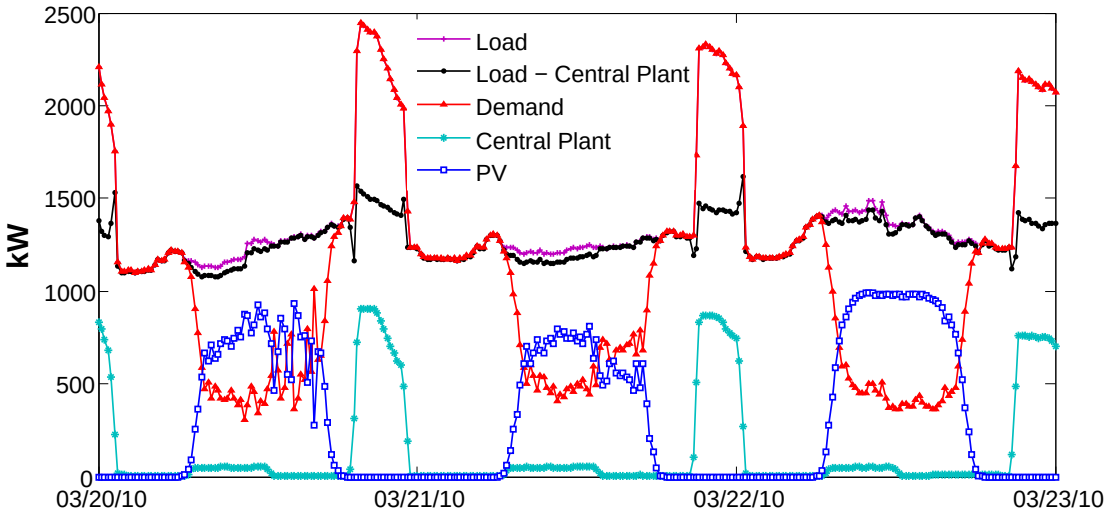

Figure 7.4 – Load profile of UC Merced for 20–23 March 2010.

large compressors for its centralized cooling system which chills and stores water. Currently, these compressors are operated at night during 10:00pm–3:00am Pacific Daylight Saving Time (PDT) due to lower PG&E tariffs and higher operating efficiencies.

7.3.2 PV, Load and Campus Demand Variability

To study the effect of PV on campus load and demand from PG&E, only day-time values are considered so that the ramps of the campus load which are due to cooling and heating operations at the Central Plant (P_{CP}) are excluded. Even though these ramps are relatively larger, they are well understood and mostly predictable, thus they do not contribute to the random variability in the overall campus load. In Fig. 7.3, it is observed that any fluctuation in P_{PV} is directly passed to P_D for which the supplier (utility service), in this case PG&E, has to compensate.

Figure 7.5 compares the day-time 15-min fluctuations for the P_{PV}, P_L, and P_D time-series. Again, some data in May and June was removed due to problems with an inverter. The fluctuation patterns in the overall demand are similar to the P_{PV}, whereas the fluctuation patterns in the net campus load are relatively constant throughout the year. The probability distributions for

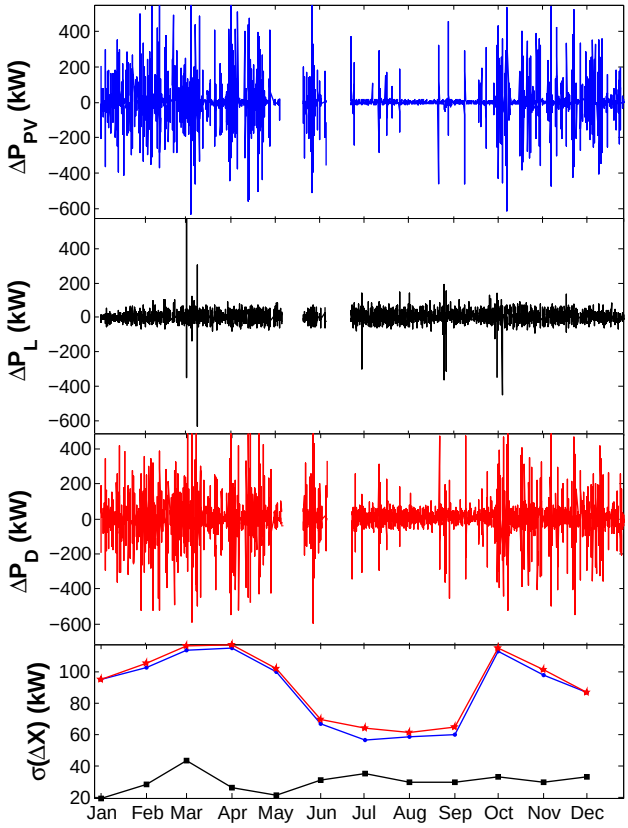

Figure 7.5 – Time series of 15-minute step changes for PV(kW), Load(kW) and Demand(kW). Bottom graph is the computed standard deviations.

the ramps over the entire year are compared in Fig. 7.3 showing that the ramp distribution of the load can be well approximated by a normal distribution with the same standard deviations as the load ($N(0, \sigma_{\Delta L})$). The bottom plot in Fig. 7.5 shows the monthly standard deviations of the fluctuations. This plot shows that the overall demand fluctuations are dominated by the PV power output fluctuations. In Section 2, it was shown that the variability of P_{PV} has a very high correlation with GHI, therefore, GHI variability data can be used to describe the added variability to the campus' demand when one-third energy is supplied by a 1-MW PV plant. These observations place significance in characterizing solar irradiance variability for estimating the variability impacts on medium size industrial energy customers.

7.4 Battery Storage System Applied To Mitigate Large Pv Ramps

In this section, we consider the use of a battery system as a storage device in order to simulate the costs associated with the mitigation of the power fluctuations. The cost estimates are achieved by modeling the system as a problem of revenue optimization which includes the revenues due to the wholesale of power produced and the costs from the utilization of a battery. In a broader point of view, the operation of a battery can be thought of as a generic storage system or reserve capacity required to back up the renewable energy system since the operation of the battery is such that it is immediately dispatchable and is used to compensate for high fluctuations of an electrical balancing system. The methodology that is used here was recently formulated and employed by Omran et. al, 2011 for the case of reducing fluctuations of 10-MW PV plant using either LA or NA batteries as well the option of dumping energy. The objective carried out by Omran et. al 2011 was to make an evaluation of the most cost effective ways for reducing fluctuations by considering the use of two different types of batteries and also the options of dumping loads. Their approach for estimating costs is adopted here, but rather than determining most cost effective alternative, our focus is to determine the correlations between PV variability with the resulting revenues after including the incurred costs of a storage system.

7.4.1 Optimization Problem Formulation

The optimization problem is to maximize revenues after including the capital and operational costs associated with the storage system. These associated costs are accounted in the second and third terms of the objective function (Eqn (7.5)). Storage system and operating characteristics are accounted for in the constraints. The problem formulation is to maximize the revenues as follows:

$$\max R = \sum_{i=1}^{M} \alpha \frac{\Delta t}{60} P_G(i) - \left(\beta \frac{1}{\eta_{PB}} P_{B,\max} + \gamma \frac{1}{\eta_{ch}} E_{B,\max} \right), \tag{7.5}$$

where the decision variables of the optimization problem include the power of the battery P_B, the total generated power P_G the energy of the battery E_B and the required power and energy densities ($P_{B,\max}$ and $E_{B,\max}$) of the battery which are determined endogenously through the maxization of the revenue function (Eqn (7.5)). The parameter α is the electricity price given in Table 2. The parameters β and γ correspond to the prices associated with the battery system power (C_P) and energy (C_E) capital costs, respectively. The parameters η_{PB} and η_{ch} correspond to the efficiencies of the battery system to deliver power and energy capacity, respectively.

The optimization is subject to the following constraints:

$$P_G(i) = P_{PV}(i) + P_B(i), \tag{7.6}$$

$$P_G(i-1) - x \leq P_{PV}(i) \leq P_G(i-1) + y, \tag{7.7}$$

$$E_b(i) = E_B(i-1) + \frac{\Delta t}{60} P_B(i-1), \tag{7.8}$$

$$SOC_{\min} E_{B,\max} \leq E_B(i) \leq E_{B,\max}, \tag{7.9}$$

$$-P_{B,\max} \leq P_B(i) \leq P_{B,\max}. \tag{7.10}$$

The first constraint (Eqn. (7.6)) is simply that the sum of the produced and used power are equal to the total generated and sent to the grid. It is assumed by the first constraint that the battery only receives power from charging by the PV system. The second constraint (Eqn. (7.7)) is of primary interest in this study, as it is the constraint which forces the total generated power to be within certain ramping limits. The parameters x and y respectively set a lower bound and upper bound on the 15-min fluctuations. The optimization problem is solved for various ramp limit parameter values. The next three constraints (Eqns. (7.8–7.10)) correspond to the battery's physical characteristics. The first battery constraint (Eqn. (7.8)) relates the energy and power of the battery at a given instant in time. The second constraint (Eqn. (7.9)) sets a lower and upper limit for the energy of the battery. The energy of the battery is constrained to have positive values above the minimum state of charge ($SOC_{\min}$). The third battery constraint (Eqn. (7.10)) sets lower

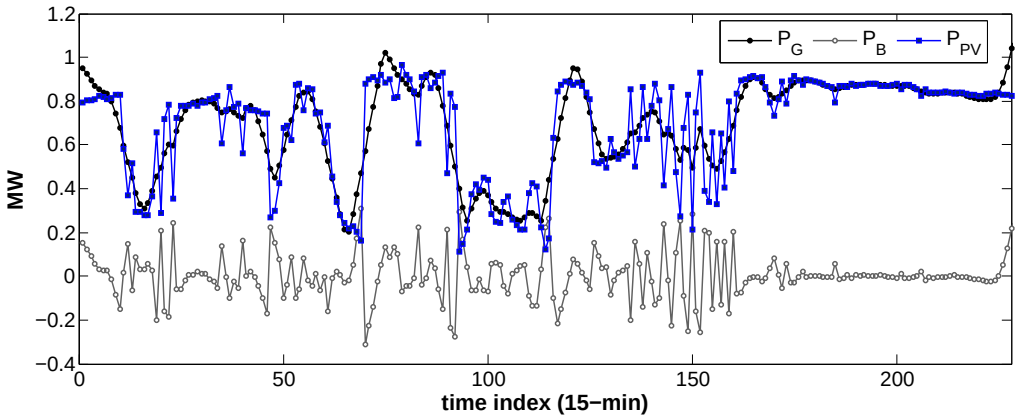

Figure 7.6 – Simulated generated and battery power and actual PV power output for a batch of 10 days with night values removed.

Table 7.1 – List of parameter values used in revenue optimization problem

Parameters	Values
η_{PB}	0.85
η_{ch}	0.75
$C_P(\$/kW)$	300
$C_E(\$/kWh)$	150
SOC_{min}	0.2
$\alpha(\$/kWh)$	0.42

and upper bound on the power output (discharging) and input (charging) of the battery. These limits on the power of the battery are determined by the battery's power density.

7.4.2 Model Parameter Values

The parameter values are the same as the ones used in [82], including the price and operating costs characteristics of the LA battery. Since the problem is only solved here for a limited amount of data of approximately a year, we ignore possible replacements of the battery which were included in [82] and the discount rates, and only focus on the parameter values which describe the battery's capital and operating cost, efficiency, $SOC_{\min}$ parameter, and the price of electricity (α). Table 7.1 lists the value of each of these parameters as obtained from [82].

7.4.3 Optimization Results

The primary interest of the this analysis is to relate the loss of revenues due to P_{PV} to the variability metric. In subsequent sections we will consider three metrics, for now the metric quantifying variability which is used is based on the standard deviation of the fluctuations using Eqn. (7.3). In order to obtain results for various levels of P_{PV} variability, we solve the optimization for batches of 14 consecutive days for the entire data set, then we compare the simulated changes in revenues to the calculated standard deviations of the fluctuations for each batch of the time-series. The changes in revenues are based on the difference between the revenues obtained by including a battery to reduce fluctuations, (R_{B+PV}), and the revenues from not including a battery while also not reducing fluctuations, (R_{PV}). The relative change in revenues is calculated as

$$\Delta R = \frac{R_{B+PV} - R_{PV}}{\bar{R}_{PV}} \tag{7.11}$$

where $\bar{R}_{PV}$ is the average revenues and R_{PV} is revenue for each batch of days simulated.

Figure 7.6 shows the resulting simulated battery power, P_{PV}, and total generated power for the first 10 days of October 2010. The battery power oscillates between positive and negative values and the net profile mean is approximately zero, which means that the battery's net contribution to the first term of the objective function is negligible compared to the second and third term.

Figure 7.7 shows some of the inequality constraints which were all satisfied by the solution of the linear program for the case with ramp limits set to 100kW/15min. The equality constraints (not shown) are always binding while the inequality constraints are only binding at a few points. However, since the optimization was solved for the entire 10 day set in this example, the points where the inequality constraints are binding actually effect the entire optimization results and not just the individual binding points.

The optimization was carried out for ramp-limits 6, 10, 14 and 18% of the power rating of the PV plant (1-MW) for batches of 14-days for the entire data set. Figure 7.8 shows the changes in revenues as a function of the variability as quantified by the standard deviation of the fluctuations.

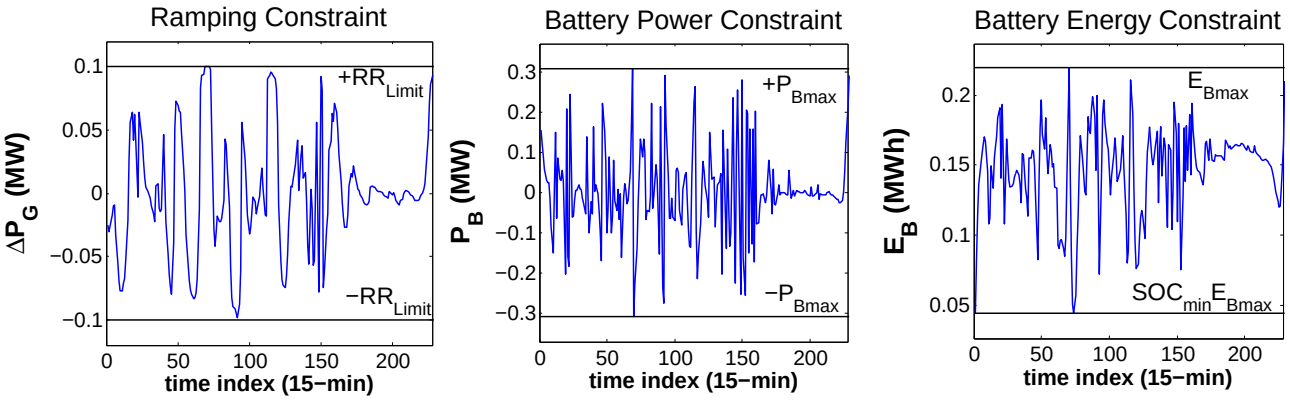

Figure 7.7 – Validation of constraint equations.

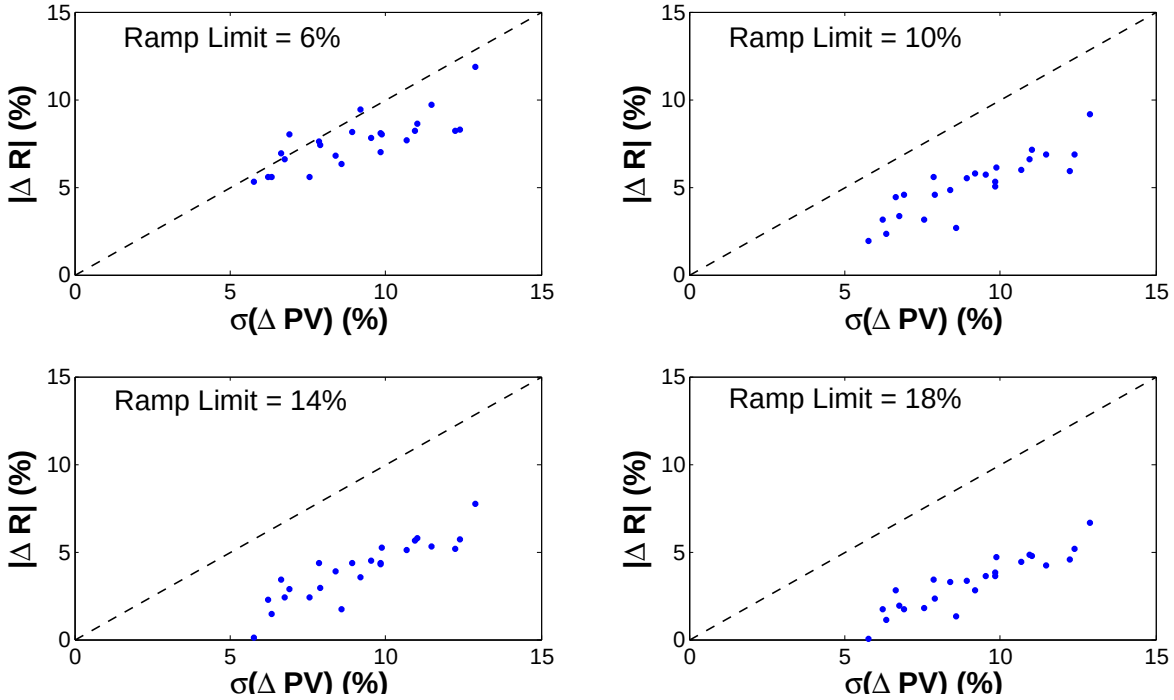

Figure 7.8 – Change in revenues vs Variability of PV power output for different ramp limits.

As expected, when the PV variability is very small, there are no changes in revenues.

From Fig. 7.8, we observe that as the ramp limits are relaxed (smaller ramp limits), then the changes in revenues also decreases, regardless of the variability. From these graphs, it is shown that the simulated changes of revenues are not only dependent on the ramp limits but are also strongly dependent on the PV variability.

The second and third terms of the objective function, Eqn. (7.5), depend on the power and

Table 7.2 – Correlation coefficients of simulation produced parameters and variability metrics.

Variability Metric	ΔR	$E_{B\max}$	$P_{B\max}$
V	0.902	0.907	0.843
V'	0.827	0.827	0.782
V'	0.911	0.917	0.899

energy density values of the battery system which are determined by solving the optimization problem. As already noted, the first term of the objective function has a negligible effect on calculating the changes in revenues. Based on the observations that the changes in cost of revenues are highly correlated with the variability, we may also conclude that the required power and energy density of the battery must also have high correlations with variability.

7.4.4 Correlations between simulated results and variability

For each of the 14-day runs, $P_{B,\max}$ and $E_{B,\max}$ are also determined in addition to the changes in revenues and the variability. Correlation coefficients are computed for the variability metric with ΔR , $P_{B,\max}$ and $E_{B,\max}$. Alternative variability metrics are also considered such as the mean of the absolute delta values,

$$V' = \frac{1}{N} \sum |\Delta P_{PV}| \tag{7.12}$$

and the mean of the 10% highest absolute delta values,

$$V'' = \frac{1}{N} \sum_{\max 10\% |\Delta \mathrm{P_{PV}}|} |\Delta P_{PV}| \tag{7.13}$$

Table 7.2 lists the correlation coefficients for each of the resulting simulated quantities vs the variability metrics. Although the highest correlations belong to the metric V'', a framework [32, 33] was recently established for the metric V for quantifying variability from distributed PV systems. Therefore, it is better to compute the relative savings of distributed PV systems based on V which can be readily calculated from solar irradiance data as discussed in Section 2.

7.5 Potential Economic Benefits

The potential economic benefits of using distributed PV systems can be estimated by comparing with the results obtained for the costs of using a battery system. As a criteria for going with the large single system versus a distributed system, we write

$$B_{EoS} > B_{RV} \tag{7.14}$$

where B_{EoS} is the benefit of economies of scales and B_{RV} is the benefits associated with reduced variability. Just like any commodity, solar energy systems have reduced capital costs when purchased in bulk, which is why many solar companies and utilities are currently favoring large multi-MW installations. Suppose that we relate the capital costs of an ensemble of systems $C^{\sum N}$ with the capital costs of a large single system C^1 as

$$C^1 = fC^{\sum N}, \tag{7.15}$$

where $0 < f < 1$ is the fraction of the ensemble (many individual systems) costs corresponding to the costs of a single system. The value f would depend on costs associated with additional land use, transmision lines, etc. and in general is a decreasing function of N. According to Hoff et. al., the variability of an ensemble of PV (V^1) is related to the variability of a single system ($V^{\sum N}$) for a spacious orientation of distributed identical PV systems as,

$$V^{\sum N} = gV^1 \tag{7.16}$$

where $g = 1/\sqrt{N} < 1$ as given by Hoff et. al.. From the results obtained in the previous section of this paper it is found that the battery costs associated with limiting PV fluctuation ($C_{\Delta PV}$ is proportional to the variability,

$$C_{\Delta PV} = \beta V \times C^* \tag{7.17}$$

where C^* is the normalization factor: $C^* = R_{PV} = \sum \alpha P_{PV}$, i.e., the revenues from PV production. The battery cost savings from the option of a distributed system case relative to a large single-station can be estimated as

$$\begin{aligned} B_{RV} &= \{(\beta V^1 + \alpha) - (\beta V^{\sum N} + \alpha)\} \times T_L && (7.18) \\ &= \beta T_L (V^1 - V^{\sum N}) && (7.19) \\ &= \beta T_L V^1 (1 - g) && (7.20) \end{aligned}$$

where T_L is the lifetime of the PV systems, β is the constant of proportionality and α is a parameter related to any imposed ramp limits.

The benefits of economies of scales can be written as

$$\begin{aligned} B_{EoS} &= C^1 - C^{\sum N} && (7.21) \\ &= C^1 (1 - 1/f) && (7.22) \\ & && (7.23) \end{aligned}$$

From Eqn. (7.14), the criteria where centralized planning is more advantageous becomes

$$C^1 (1 - 1/f) > \beta V^1 T_L C^* (1 - g) \tag{7.24}$$

In solving for f the criteria gives,

$$f < \frac{1}{1 - \frac{\beta V^1 \tau_{LT} C^*}{C^1} (1 - g)} \tag{7.25}$$

or after substituting $g = 1/\sqrt{N}$,

$$f < \frac{1}{1 + \frac{\beta V^1 T_L C^*}{C^1} \left(\frac{\sqrt{N} - 1}{\sqrt{N}} \right)}. \tag{7.26}$$

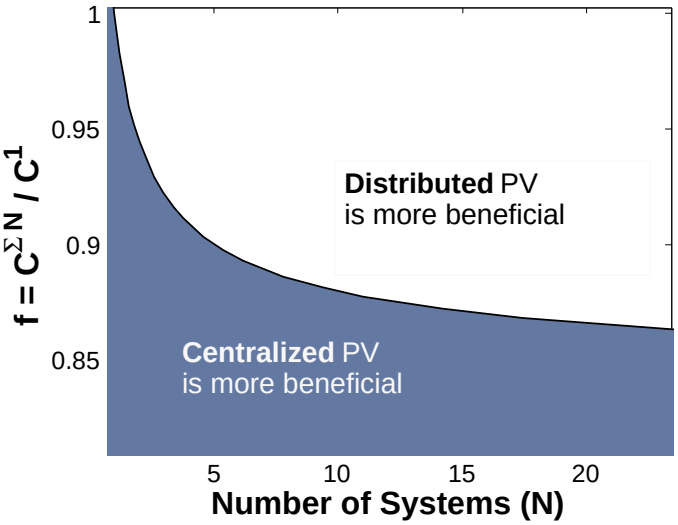

Figure 7.9 – Right hand side of criteria for values $T_L = 20$, $T_{PB} = 10$, and $V^1 = 0.15$. If $f = C^{\Sigma N}/C^1$ is below this line then it is estimated that a large single centralized PV station is more beneficial than a distributed ensemble of systems.

The first observation of this result is that if $g = 1$ (no geographic dispersion) then the criteria says that it is always advantageous to go with the single centralized plant since ($f < 1$) for the hypothesis of economies of scales. A second observation is that the ratio $\frac{\beta V^1 T_L C^*}{C^1}$ is the required battery investment relative to the capital costs of single station. This ratio can come from cost of reserve capacity resulting of the PV system. The above results also gives an estimate on how much PV distribution would be required ($\sqrt{N}$). The criteria above can further be simplified by letting $\beta = 1$ as the previous results suggest, and letting the $1/T_{PB} = C^*/C^1$ which can be interpreted as the economic payback period of the large centralized system.

$$f < \frac{1}{1 + \frac{V^1 T_L}{T_{PB}} \left(\frac{\sqrt{N}-1}{\sqrt{N}} \right)} \tag{7.27}$$

This last result is amenable for plugging in some reasonable values. As an example, we let $T_L = 20$, $T_{PB} = 10$, and $V^1 = 0.15$ then plot the right hand side of the above expression to produced Fig. 7.9.

7.6 Conclusions

This study has shown that 15-min step changes of Global Horizontal Irradiation (GHI) and PV power output (P_{PV}) are highly correlated in terms of the applied variability metrics. The GHI and P_{PV} comparisons agree with other previous studies [34, 47]. We also compared the variability of the UC Merced campus load (with peak load of approximately 3-MW) and the 1-MW PV plant and found that the total 15-minute variability is dominated by the PV system. Since the 1-MW PV variability contributes mostly to the total campus load variability, a cost analysis was applied using the utility service's (PG&E) tariffs on the PV fluctuations. This analysis provides an estimate of the costs passed to the utility service providers to compensate for the added PV variability. The calculated costs were found to be proportional to the calculated PV variability's and on the order 5–25% of total PV savings.

Lastly, a simulation based on revenue optimization for including a battery storage system to reduce fluctuations was performed. The results indicate that loss of revenues incurred from reducing or "smoothing" the power output variability to within required ramp limits is well correlated with PV variability. The constraints set by the ramp limits is also a key parameter in evaluating the revenue losses.

Integrating solar to the grid not only adds to the variability but it also introduces additional cost to compensate for the fluctuations. As emphasized in this work, it is important to quantify solar irradiance variability for a given location in order to perform comprehensive economic analysis of solar power systems .

Chapter 8

Conclusions

In the current work, forecasting models were developed at multiple-time horizons including 3–15 minutes ahead using a sky imager, 30–120 minutes ahead forecasts using a combined satellite and ANN-based approach, 1-hr ahead forecasts using ground-based measurements, and same-day and 1-day ahead time horizons using the NDFD forecasting database. The results of the NDFD-based forecasts were on par with a similar model which was previously validated over several climatically distinct locations [8]. Likewise, the developed 1-hr ahead forecasting models performed well, but were only evaluated over a limited data set because the equipment used was only recently made available. Correspondingly, further development is required of the short-term forecasting models which were studied. Direct cloud information obtained from a sky imager and satellite observations were also applied for intra-hour and intra-day solar irradiance forecasts resulting in some improvement in forecast accuracy with other models existing in the literature [15, 25, 1, 8].

Because there is a high demand for very accurate solar forecasting, it is imperative to take into serious considerations how forecasting models are evaluated so that different forecast models can be properly compared [27]. In this regard, the current work addresses this issue by proposing an approach for evaluating forecasting skill. It was demonstrated that this approach directly accounts for variability of the solar irradiance as opposed to other metrics that do not [2]. An important outcome of the proposed forecast skill is to apply a clear-sky persistence model and to observed the

improved accuracy for newly developed forecast model over the persistence forecasts. This sort of evaluation procedure is currently lacking in many forecast models presented in the literature.

To enhance the perceived benefits of solar forecasting, it is necessary to demonstrate through applications the advantages of having solar forecasts. As a step in this direction, this work included a simulation of using a battery as a back-up to a solar energy system (the UC Merced 1-MW photovoltaic plant). The simulation was such that the net revenues were maximized after including the costs associated with the battery, as well as including other operational constraints. An implied assumption of the presented work was that the PV output was perfectly forecastable since the optimization is done on the entire batches of data sets. This assumption is probably reasonable if it is also assumed that the battery can instantaneously ramp up and down. Realistically and for other back-up systems, the ramping capabilities should be accounted for and also the forecasting errors. Again, a detailed characterization of the PV (or solar) variability is key to understanding the economic impacts, a point not emphasized enough or sometimes neglected in variable generation studies [82, 38]. Variability characterization is in particular important for analyzing the benefits of reduced variability through geographic dispersion or reduced variability for certain parts of the year. Other system configurations, such as using a different storage system, etc. can be similarly studied.

Bibliography

[1] A. Hammer, D. Heinemann, C. Hoyer, R. Kuhlemann, E. Lorenz, R. Müller, and Beyer H. G. Solar energy assessment using remote sensing technologies. *Remote Sensing of Environment*, 86:423–432, 2003.

[2] R. Marquez and C. F. M. Coimbra. A novel metric for evaluation of solar forecasting models. *ASME Journal of Solar Energy Engineering,*, accepted, 2012.

[3] R. Perez, S. Kivalov, Schlemmer J., K. Jr. Hemker, D. Renne, and T. E. Hoff. Validation of short and medium term operational solar radiation forecasts. *Solar Energy*, 84:2161–2172, 2010.

[4] D. Lew and R. Piwko. Western Wind and solar integration study. Technical report, National Renewable Energy Laboratories, 2010.

[5] V. Sundar. Integration of renewable resources: operational requirements and generation fleet capability at 20 percent RPS. Technical report, California Independent System Operator (CAISO), 2010.

[6] G. D. Rodriguez. A utility perspective of the role of energy storage in the smart grid. In *Power and Energy Society General Meeting, 2010 IEEE*, pages 1–2, Jul 2010.

[7] R. Marquez and C. F. M. Coimbra. Forecasting of global and direct solar irradiance using stochastic learning methods, ground experiments and the NWS database. *Solar Energy*, 85(5):746–756, May 2011.

[8] R. Perez, S. Kivalov, J. Schlemmer, K. Hemker, D. Renne, and T. E. Hoff. Validation of short and medium term operational solar radiation forecasts in the US. *Solar Energy*, 84(5):2161–2172, 2010.

[9] J. Cao and X. Lin. Study of hourly and daily solar irradiation forecast using diagonal recurrent wavelet neural networks. *Energy Conversion and Management*, 49(6):1396–1406, Jun 2008.

[10] A. Mellit. Artificial intelligence technique for modelling and forecasting of solar radiation data: a review. *Int. J. Artif. Intell. Soft Comput.*, 1:52–76, Nov 2008.

[11] L. Martin, L. F. Zarzalejo, J. Polo, A. Navarro, R. Marchante, and M. Cony. Prediction of global solar irradiance based on time series analysis: application to solar thermal power plants energy production planning. *Solar Energy*, 84(10):1772–1781, Oct 2010.

[12] E. Lorenz, J. Hurka, D. Heinemann, and H. G. Beyer. Irradiance forecasting for the power prediction of grid-connected photovoltaic systems. *IEEE Journal of Selected Topics in Applied Earth Observations and Remote Sensing*, 2(1):2–10, 2009.

[13] P. Mathiesen and J. Kleissl. Evaluation of numerical weather prediction for intra-day solar forecasting in the continental united states. *Solar Energy*, 85(5):967–977, May 2011.

[14] C. Changsong, D. Shanxu, C. Tao, and L. Bangyin. Online 24-h solar power forecasting based on weather type classification using artificial neural network. *Solar Energy*, 85(11):28562870, Aug 2011.

[15] A. Hammer, C. Heinemann, E. Lorenz, and B. Lückeke. Short-term forecasting of solar radiation based on image analysis of meteosat data. In *TEUMETSAT meteorological satellite data user's conference*, pages 331–337, 1999.

[16] A. Mellit. Artificial intelligence technique for modelling and forecasting of solar radiation data: a review. *International Journal of Artificial Intelligence and Soft Computing*, 1:52–76, 2008.

[17] A. Mellit and A. M. Pavan. A 24-h forecast of solar irradiance using artificial neural network: application for performance prediction of a grid-connected pv plant at Trieste, Italy. *Solar Energy*, 84(5):807–821, May 2010.

[18] A. Mellit, H. Eleuch, M. Benghanem, C. Elaoun, and A. M. Pavan. An adaptive model for predicting of global, direct and diffuse hourly solar irradiance. *Energy Conversion and Management*, 51(4):771–782, Apr 2010.

[19] A. Sfetsos and A. H. Coonick. Univariate and multivariate forecasting of hourly solar radiation with artificial intelligence techniques. *Solar Energy*, 68(2):169–178, Feb 2000.

[20] R. Marquez, V. G. Gueorguiev, and C. F. M. Coimbra. Forecasting solar irradiance using sky cover indices. *ASME Journal of Solar Energy Engineering,*, in press, 2012.

[21] G. Reikard. Predicting solar radiation at high resolutions: A comparison of time series forecasts. *Solar Energy*, 83(3):342–349, Mar 2009.

[22] E. M. Crispim, P. M. Ferreira, and A. E. Ruano. Prediction of the solar radiation evolution using computational intelligence techniques and cloudiness indices. *International Journal of Innovative Computing, Information and Control*, 4(5):1121–1133, 2008.

[23] W. C. Chi, B. Urguhart, M. Lave, A. Dominquez, J. Kleissl, J. Shields, and B. Washom. Intra-hour forecasting with a total sky imager at the uc san diego solar energy testbed. *Solar Energy*, 85(2011):2881–2893, Sept 2011.

[24] Peder Bacher, Henrik Madsen, and Henrik Aalborg Nielsen. Online short-term solar power forecasting. *Solar Energy*, 83:1772–1783, 2009.

[25] A. Hammer, C. Heinemann, C. Hoyer, and E. Lorenz. Satellite based short-term forecasting of solar irradiance–comparison of methods and error analysis. In *The 2001 EUMETSAT meteorological satellite data user's conference*, pages 677–684, 2001.

[26] H. T. C. Pedro and C. F. M. Coimbra. Assessment of forecasting techniques for solar power output with no exogenous inputs. *Solar Energy*, in press, 2012.

[27] V. Kostylev and A. Pavlovski. Solar power forecasting performance towards industry standards. In http://ams.confex.com /ams/ 92Annual/ webprogram/Paper203131.html, editor, *92nd American Meteorological Society Annual Meeting*, 2011.

[28] C. N. Long, J. C. Barnard, J. Calbo, and T. P. Ackerman. Using integrated surface radiation measurements to infer cloud properties. In *Ninth Symposium on Integrated Observing and Assimilation Systems for the Atmosphere, Oceans, and Land Surface*, 2005.

[29] C. N. Long, J. M. Sabburg, J. Calbo, and D. Pages. Retrieving cloud characteristics from ground-based daytime color all-sky images. *Journal of Atmospheric and Oceanic Technology*, 23(5):633–652, May 2006.

[30] B. Thurairajah and J. A. Shaw. Cloud statistics measured with the infrared cloud imager (ICI). *IEEE Trasactions on Geoscience and Remote Sensing*, 43(9), Sep 2005.

[31] In: Proceedings of the International Workshop of Solar Resource from the Local Level to Global Scale in Support of the Resource Management of Renewable Electricity Generation, Institute for Environment and Sustainability, Joint Research Center. *Forecasting of solar irradiation*, Ispra, Italy, 2004.

[32] T. E. Hoff and R. Perez. Quantifying pv power output variability. *Solar Energy*, 84(10):1782–1793, Oct 2010.

[33] R. Perez, S. Kivalov, J. Schlemmer, K. Jr. Hemker, and T. Hoff. Parameterization of site-specific short-term irradiance variability. *Solar Energy*, 85(7):1343 – 1353, 2011.

[34] A. Mills, M. Ahlstrom, M. Brower, A. Elllis, R. George, T. Hoff, B. Kroposki, C. Lenox, N. Miller, J. Stein, and Y. Wan. Understanding variability and uncertainty of photovoltaics for integeration with the electric power systems. Technical Report LBNL-2855E, Ernest Orlando Lawerence Berekeley NAtional Laboratory, Dec 2009.

[35] A. Mills and R. Wiser. Implications of wide-area geographic diversity for short-term variability of solar power. Technical report, Lawrence Berkeley National Laboratory Technical Report, 2010.

[36] A. E. Curtright and J. Apt. The character of power output from utility-scale photovoltaic systems. *Progress In Photovoltaics*, 16(3):241–247, May 2008.

[37] Flexible Ramping Constraint, California ISO, Feb. 2011.

[38] P. Meibom, C. Weber, R. Barth, and H. Brand. Operational costs induced by fluctuating wind power production in Germany and Scandinavia. *IET Renewable Power Generation*, 3(1):75–83, Mar 2009.

[39] Benjamin K. Sovacool. The intermittency of wind, solar, and renewable electricity generators: Technical barrier or rhetorical excuse? *Utilities Policy*, 17(3-4):288 – 296, 2009.

[40] P. Ineichen. Comparison of eight clear sky broadband models against 16 independent data banks. *Solar Energy*, 80:468–478, 2006.

[41] L. F. Zarzalejo, J. Polo, and L. Ramirez. Gc_model5_irradiance, 2004. (Matlab Computer Program) CD-ROM accompanying [26].

[42] V. Badescu. *Modeling Solar Radiation at the Earth Surface*. Springer-Verlag, Berlin Heidelberg, 2008.

[43] T. E. Hoff and R. Perez. Modeling PV fleet output variability. *Solar Energy*, doi:10.1016/j.solener.2011.11.005, 2011.

[44] M. Lave and J. Kleissl. Solar variability of four sites across the state of colorado. *Renewable Energy*, 35(12):2867–2873, Dec 2010.

[45] C. M. Bishop. *Neural networks for pattern recognition*. Oxford University Press, Greate Clarendon Street, Oxford, 1995.

[46] M. Lave, J. Kleissl, and E. Arias-Castro. High-frequency irradiance fluctuations and geographic smoothing". *Solar Energy*, 10.1016/j.solener.2011.06.031, 2011.

[47] J. Marcos, L. Marroyo, E. Lorenzo, D. Alvira, and E. Izco. Power output fluctuations in large scale PV plants: one year observations with one second resolution and a derived analytic model. *Progress In Photovoltaics*, 19(2):218–227, Mar 2011.

[48] YES. *TSI-880 Automatic Total Sky Imager Manual*. Yankee Environmental Systems, Inc., Airport Industrial Park 101 Industrial Blvd. Turners Falls, MA 01376 USA, 2011.

[49] Tao Peng. Circularhough_grd. http://www.mathworks.com/ matlabcentral/ fileexchange/9168, 2011.

[50] J. A. Duffie and W. A. Beckman. *Solar Engineering of Thermal Processes, Third Edition* . John Wiley & Sons, Inc., Hoboken, New Jersey, 2006.

[51] Nobuhito Mori and Kuang-An Chang. Introduction to MPIV, 2003. http://www.oceanwave.jp/softwares/mpiv.

[52] C. N. Long, T. P. Ackerman, K. L. Gaustad, and J. N. S. Cole. Estimation of Fractional Sky Cover from Broadband Shortwave Radiometer Measurements. *Journal of Geophysical Research*, 111(D11204), 2006.

[53] Juan Huo and Daren Lu. Cloud determination of all-sky images under low-visibility conditions. *Journal Of Atmospheric And Oceanic Technology*, 26(10):2172–2181, Oct 2009.

[54] Mantelli Neto, Sylvio Luiz, Aldo von Wangenheim, Enio Bueno Pereira, and Eros Comunello. The use of euclidean geometric distance on rgb color space for the classification of sky and cloud patterns. *Journal of Atmospheric And Oceanic Technology*, 27(9):1504–1517, Sep 2010.

[55] Q. Li, W. Lu, and J. Yang. A hybrid thresholding algorithm for cloud detection on ground-based color images. *Journal of Atmospheric and Oceanic Technology*, 28:1286–1296, Oct 2011.

[56] D. Cano, J.M. Monget, M. Albuisson, H. Guillard, N. Regas, and L. Wald. A method for the determination of the global solar-radiation from meteorological satellite data. *Solar Energy*, 37(1):31–39, 1986.

[57] R. Marquez and C. F. M. Coimbra. Intra-hour DNI forecasting methodology based on cloud tracking image analysis, 2012. *submitted*.

[58] C. Schillings, H. Mannstein, and R. Meyer. Operational method for deriving high resolution direct normal irradiance from satellite data. *Solar Energy*, 76:475–484, 2004.

[59] CM Bishop. Neural networks and their application. *Review of Scientific Instruments*, 65:1803–1832, 1994.

[60] The Eppley Laboratory, Inc., 12 Sheffield Avenue, PO Box 419 Newport, Rhode Island 02840 USA. *Precision Spectral Pyranometer*.

[61] The Eppley Laboratory, Inc., 12 Sheffield Avenue, PO Box 419 Newport, Rhode Island 02840 USA. *Precision Infrared Radiometer*.

[62] B. Albrecht and S. K. Cox. Procedures for improving pyrgeometer performance. *Journal of Applied Meteorology*, 16:188–197, February 1977.

[63] P. Berdahl and R. Fromberg. The thermal radiance of clear skies. *Solar Energy*, 29:299–314, 1982.

[64] C. Paoli, C. Voyant, M. Muselli, and M. Nivet. Forecasting of preprocessed daily solar radiation time series using neural networks. *Solar Energy*, 84(12):2146–2160, Dec 2010.

[65] P. J. Durrant. *winGamma^{TM}: a non-linear data analysis and modelling tool for the investigation of non-linear and chaotic systems with applied techniques for a flood prediction system.* PhD thesis, Department of Computing Science, Cardiff University, 2001.

[66] A. J. Jones. New tools in non-linear modelling and prediction. *Computational Management Science*, 1:109–149, 2004.

[67] I. D. Wilson, A. J. Jones, D. H. Jenkins, and J. A. Ware. Predicting housing value: Genetic algorithm attribute selection and dependence modelling utilising the Gamma test. In Binner, JM and Kendall, G and Chen, SH, editor, *Applications of Artificial Intelligence in Finance and Economics*, volume 19 of *Advances in Econometrics : A Research Annual*, pages 243–275. JAI-Elsevier Sci BV, Sara Burgerhartstraat PO Box 211, 1000 AE Amsterdam, Netherlands, 2004.

[68] A. Moghaddamnia, R. Remesan, M. H. Kashani, M. Mohammadi, D. Han, and J. Piri. Comparison of LLR, MLP, Elman, NNARX and ANFIS Models-with a case study in solar radiation estimation. *Journal of Atmospheric and Solar-Terrestrial Physics*, 71:975–982, 2009.

[69] R. Remesan, M. A. Shamim, and D. Han. Model data selection using gamma test for daily solar radiation estimation. *Hydrological Processes*, 22:4301–4309, 2008.

[70] H. R. Glahn and D. P. Ruth. The new digital forecast database of the national weather service. *Bulletin of the American Meteorological Society*, 84:195–201, 2003.

[71] R. Perez, K. Moore, S. Wilcox, D. Renne, and A. Zelenka. Forecasting solar radiation - Preliminary evaluation of an approach based upon the national forecast database. *Solar Energy*, 81:809–812, 2007.

[72] J. L. Jr. Schattel and R. Bunge. The national weather service shares digital forecasts using web services. *Bulletin of the American Meteorological Society*, 89:449–450, 2008.

[73] Koncar, N. *Optimisation methodologies for direct inverse neurocontrol*. PhD thesis, Department of Computing Imperial College of Science, Technolgoy and Medicine, University of London, 1997.

[74] A. Stefansson, N. Koncar, and A. J. Jones. A note on the gamma test. *Neural Computing & Applications*, 5:131–133, 1997.

[75] D. Evans and A. J. Jones. A proof of the gamma test. *Proceedings of the Royal Society of London Series A-Mathematical Physical and Engineering Sciences*, 458:2759–2799, 2002.

[76] Philippe Lauret, Mathieu David, Eric Fock, Alain Bastide, and Carine Riviere. Bayesian and sensitivity analysis approaches to modeling the direct solar irradiance. *ASME Journal of Solar Energy Engineering*, 128:394–405, 2006.

[77] R. Perez, P. Ineichen, K. Moore, M. Kmiecik, C. Chain, R. George, and F. Vignola. A new operational model for satellite-derived irradiances: Description and validation. *Solar Energy*, 73:307–317, 2002.

[78] C. Schillings, R. Meyer, and H. Mannstein. Validation of a method for deriving high resolution direct normal irradiance from satellite data and application for the Arabian Peninsula. *Solar Energy*, 76:485–497, 2004.

[79] Frank Vignola, Peter Harlan, Richard Perez, and Marek Kiniecik. Analysis of satellite derived beam and global solar radiation data. *Solar Energy* , 81:768–772, 2007.

[80] Hanne Breitkreuz, Marion Schroedter-Homscheidt, Thomas Holzer-Popp, and Stefan Dech. Short-range direct and diffuse irradiance forecasts for solar energy applications based on aerosol chemical transport and numerical weather modeling. *Journal of Applied Meteorology and Climatology*, 48:1766–1779, 2009.

[81] A. Golnas and S. Voss. Power output variability of PV system fleets in three utility service territories in New Jersey and California. *Photovoltaic Specialists Conference (PVSC), 2010 35th IEEE*, pages 535–539, Nov 2010.

[82] W. A. Omran, M. Kazerani, and M. M. A. Salama. Investigation of methods for reduction of power fluctuations generated from large grid-connected photovoltaic systems. *IEEE Transactions On Energy Conversion*, 26:318–327, Mar 2011.